EXTRACTION STUDIES FOR THE MSU K500 CONVERSION TO A PROTON CANCER THERAPY SYNCHROCYCLOTRON

BY

Lung-Sheng Lee

A DISSERTATION

Submitted to
Michigan State University
in partial fulfillment of the requirements
for the Degree of

DOCTOR OF PHILOSOPHY

Department of Physics and Astronomy

1994

ABSTRACT

EXTRACTION STUDIES FOR THE MSU K500 CONVERSION TO A PROTON CANCER THERAPY SYNCHROCYCLOTRON

By

Lung-Sheng Lee

The design features of the extraction systems for the proposed proton cancer therapy machine converted from the MSU K500 isochronous cyclotron are presented. It is helpful to consider the economic factor that the K500 cyclotron could be transformed to the K250 proton synchrocyclotron needed for cancer therapy, with modification as limited as possible. The results indicate that it is difficult, but possible, to meet the medical requirement for beam properties, mainly owing to the resonance crossing in the extraction region, worsened by the intrinsically small average energy gain per turn (implication of low dee voltage) for synchrocyclotrons.

The regenerative method, $\nu_r = 1$ resonant excitation method and precession method are investigated extensively by detailed studies of beam dynamics carried out by the Z^4 code and DEFLZ800 program. Our studies show that the regenerative method is the most promising candidate for the extraction system for this machine. It gives better results and is able to be easily handled.

We also found that the performance of the extraction system depends strongly and sensitively on dee voltage, on internal beam quality and on field imperfections.

To my grandparents and mother

ACKNOWLEDGEMENTS

I thank Dr. H.G. Blosser, my supervisor, for his continued advice and patient guidance. Without his understanding and gracious help, I would end up nowhere. I am indebted to the lab's staff and graduate students, whose help I received during my stay in NSCL. I also thank Drs. M. Gordon, F. Marti and D. Johnson for their valuable assistance.

Special thanks to the National Science Foundation for making these studies financially possible.

I am grateful to Drs. J.S. Kovacs, J. Nolen, M. Berz and W. Pratt for their service on my Ph.D. guidance committee.

Contents

List of Tables

List of Figures

Chapter 1

Introduction

Interest in proton cancer therapy is at a high level at present because of a) clinical experience, which indicates that proton therapy is one of the most effective method of cancer therapy, and b) the cost effectiveness of present accelerator technology. In 1992, Dr. A.T. Porter (Chairman of the department of Radiation Oncology at Wayne State University and Specialist-In Chief of Radiation Oncology at the Detroit Medical Center) visited here and asked Prof. H. Blosser (University Distinguished Professor of MSU, former Director of NSCL and author's major advisor) whether the MSU K500 cyclotron could produce the proton beams needed for cancer therapy. Blosser responded "A first thought is that it is probably technically possible; the isochronous K500 cyclotron would provide more than adequate bending power but would lack focusing – however, a synchrocyclotron adapted from the K500 would probably be a viable solution". Thereafter this thesis was started in September 1992 to study the orbit dynamics of one of the most intricate details involved in converting the K500 to a synchrocyclotron for proton therapy, namely how to extract the beam.

1.1 Historical Background

The initial concept and feasibility of the cyclotron was established by E.O. Lawrence in the early 1930s [1] [2]. A few years later, at the end of 1930s, several cyclotrons were in operation, dedicated to research in nuclear physics; they accelerated protons, deuterons and helium ions, to the territory of 5 MeV [3]. A decreasing magnetic field with radius was employed to maintain axial focusing of the ions in these non-relativistic cyclotrons.

The conflict between the axial focusing requirement and the relativistic mass increase, an increasing field with radius required to match the cyclotron resonance frequency $\omega = qB/mc$, was not effectively solved until the discovery of the principle of phase stability by Veksler [4] and Mcmillan [5] in 1944-45. This principle shows that if the accelerating frequency is modulated in accordance with the mass change in the relation $\omega = qB/mc$, then there will be an equilibrium phase ϕ_s (ϕ is the phase angle of the ion relative to the sinusoidal RF wave) about which the phase of other particles oscillates. The energy gain per turn similarly oscillates about a mean value, determined by dee voltage, phase angle ϕ_s, etc; and the total energy will eventually reach the desired maximum value. Construction of this type of cyclotron, denoted FM cyclotron or synchrocyclotron, was started at the middle of the 1940s and came to its height in the 1950s. In their fully developed form, they were able to provide energy of light nuclei up to several hundreds of MeV and about 1 μA current [3].

In the 1960s and 70s, synchrocyclotrons (SC) were gradually phased out because [6] (1) The SCs were soon at their energy maximum, after their blooming years in the 1950s, for economic reasons; interest in particles of the highest energy shifted to the much less costly synchrotron in response to the research demands of the newly evolving field of "particle physics". (2) The nuclear physics need for precise experi-

ments was poorly filled by SCs due to their less defined and poorer duty cycle beams, and meanwhile the introduction of the "sector focusing" Lawrence-type cyclotron in early 1950s evolved gradually into devices of excellent precision with maximum energy pushing steadily higher thru the range of the SC's.

The original idea of sector focusing was invented by L.H. Thomas [7] in 1938. Thomas pointed out that it is possible to have both constant orbital frequency and axial focusing by using an "azimuthally varying" magnetic field where the radial increase of field matches that required by relativity. The Thomas suggestion for various reasons was not tested experimentally until the 1950s. Two small experimental electron cyclotrons, following the recipe of Thomas, were built and studied at Berkeley in a classified project in the early 1950s [8]; proof of the validity of the concept was established.

The next important contribution in the evolution of the sector focused or "isochronous" cyclotron to relativistic energies was made by the MURA group (K.R. Symon, D.W. Kerst et al., 1955-56) in their development of the FFAG (fixed field, alternating gradient) accelerator [9]. They pointed out that shaping the Thomas hills and valleys in a spiral (azimuth changing with radius) would increase the axial focusing force of the magnetic field; the contribution of the spiral effect to the axial focusing can be many times greater than the simple Thomas effect.

Since the 1950s, efforts of cyclotron designers have been directed continuously toward overcoming the limitations of energy imposed by the relativity effect, on providing greater flexibility both in the choice of energy and the choice of particle to be accelerated, and on improving the beam quality. Much progress has thereby resulted, and both maximum energy and versatility have greatly increased. Variable energy, multi-particle, high intensity, exceptional energy resolution and nearly 100% extraction efficiency have all been strikingly achieved, as particularly exemplified in

the MSU sector-focused isochronous K50 cyclotron (H.G. Blosser and M.M. Gordon, 1959-1965) [10]. On the other hand, the objective of higher energies was carried by the "meson factory" cyclotrons in Vancouver [11] and Zürich [12] and by the Indiana isochronous separated sector cyclotron (M. Rickey and R. Pollock, 1966-1975) [13]. The isochronous cyclotron has then gradually become the mainstream accelerator choice for nuclear physics research since 1980.

With the advent of effective superconducting coil technology, "superconducting cyclotron" projects at MSU [14] [15] and at Chalk River [16] were launched in the early 1970s in response to needs of research on heavy ions and these came into operation in the 1980s. The attractive features of such cyclotrons are small size and low cost [17] and superconducting cyclotrons are at present flourishing.

Concurrent with the evolution of improved cyclotrons, medical concepts for improving radiation therapy were also evolving. Cancer therapy using protons was first proposed by Robert Wilson in 1946 [18]. The first work on the biological and medical application of proton beams was conducted by J.H. Lawrence and C.A. Tobias at Berkeley in 1948 [19]. Initial clinical treatment started at Berkeley in 1954 [20]. Since then, thousands of cancer patients have been treated in many facilities (Harvard and Berkeley, USA; Uppsala, Sweden; PSI, Switzerland; Dubna and Moscow, USSR; Chiba and Tsukuba, Japan) throughout the world using accelerators originally built for nuclear physics research [20]; in these facilities the concepts of proton therapy were proved to be effective, but the adaptation of accelerators designed for physics inevitably led to non-optimal medical capability [21]. Not until the end of 1980s was a well optimized proton cancer therapy facility built at Loma Linda University Medical Center, the first facility specifically constructed to be well matched to the medical requirements of proton therapy [22].

Recently, a number of groups throughout the world worked on the design of ac-

celerators for proton cancer therapy in response to the strong demand for a low cost accelerator capable of producing beams with characteristics well matched to requirements for cancer treatment. For example, proposals by MSU [23] [21], GSI [24], IBA-SHI [25], etc.

1.2 Advantages of Proton Cancer Therapy

Proton therapy is recognized to be one of the most effective methods of cancer therapy at present [26]. Both conventional photon radiation and neutron therapy have the disadvantage of the undesirable fall-off of energy deposition with progressing penetration. For a single beam the dose applied to a deep seated tumor is much smaller than the dose to the healthy tissue. On the other hand, because of the sharp Bragg peak and the very small angular scattering for the protons, proton therapy is more favorable and the side effect will be less severe compared to conventional radiation. A typical sketch of the dose deposition versus depth in tissue (equivalent to water) for both protons [27] and photons (for comparison) [28], and the Bragg peak depth as a function of proton energy [27] are given in Figure 1.1.

1.3 Accelerator Requirements

The requirements on accelerators for proton therapy have been summarized by Pedroni [29] as follows.

- Maximum beam energy in the range of 220 - 280 MeV is needed for the irradiation of deep seated tumors.
- Variable energies ($\geq$ 70 MeV) in steps or continuously are required in order to control the deposition depth of the beam.

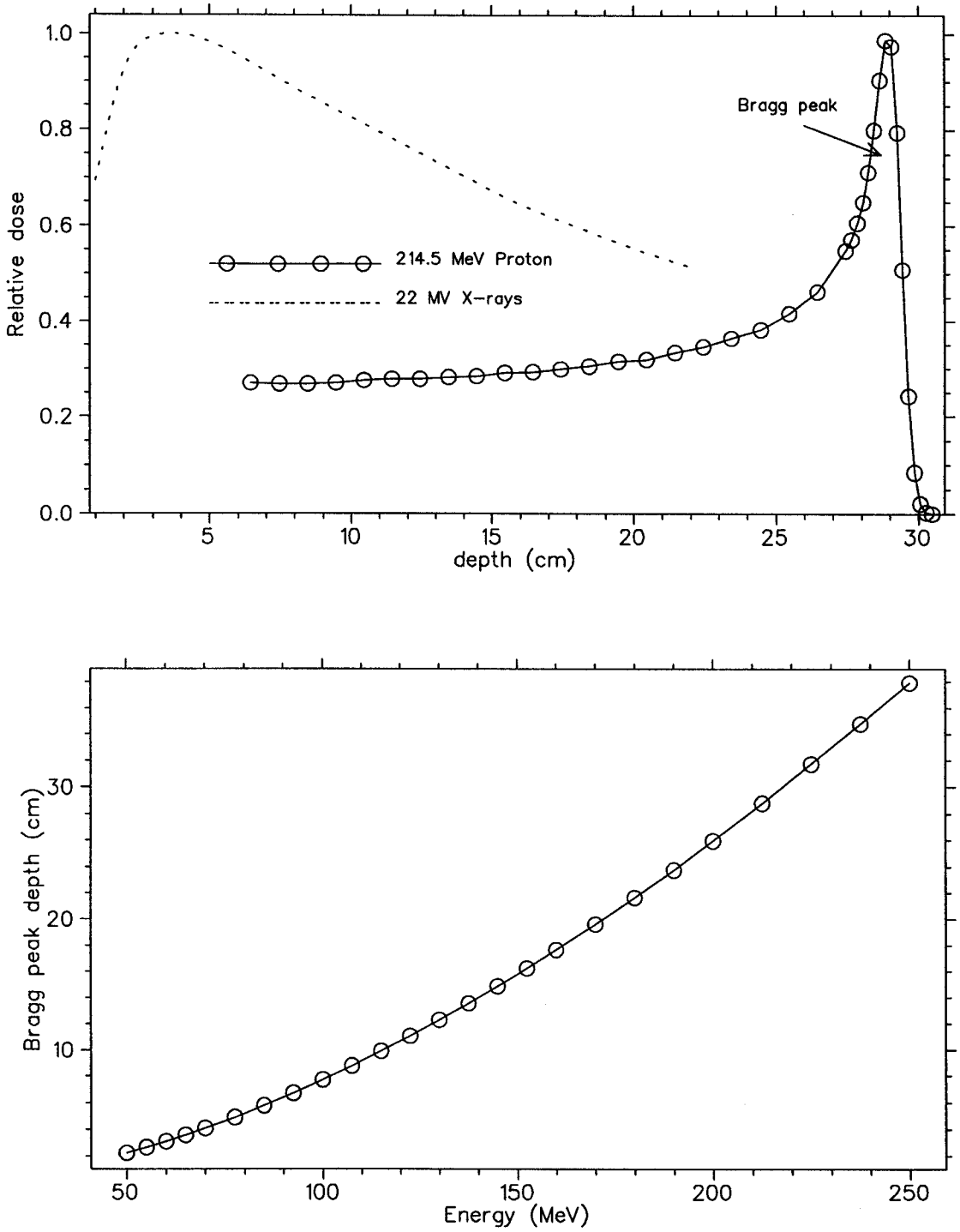

Figure 1.1: Top: experimental depth-dose curve for 214.5 MeV protons from the Paul Scherrer Institute (soild curve) [27]. The dose deposition is normalized such that the dose deposition is equal to one unit at the Bragg peak. Dash line gives dose curve for 22 MV X-rays, normalized to peak, from Ref. [28]. Bottom: Bragg peak depth as function of proton energy [27].

- Beam intensity : The required beam intensity depends on the application technique used. In general, 10 nA is enough.

- The duty cycle of the beam : The cyclotron provide the best possible time structure of the beam for the application of the dynamic scanning methods. However, a 100 - 10000 Hz pulsed machine (e.g., synchrocyclotron) is still an acceptable alternative.

1.4 General Features of Superconducting Cyclotrons and Their Role in Cancer Therapy

Superconducting cyclotrons are noteworthy for their compactness in size and cost effectiveness [17]. The successful operation of the Harper cyclotron in Detroit, the first superconducting cyclotron for cancer therapy, has demonstrated that the superconducting cyclotrons are superior to other type of accelerators for medical use and more easily installed in a hospital due to their compact size, competitive cost, and high reliability. The Harper cyclotron started patient treatments in 1992 and is in heavy use now [30].

Studies of larger superconducting medical cyclotrons have been in process for some years at MSU [23] [21] and by the EULIMA group [31]. At NSCL/MSU, a superconducting synchrocyclotron (FM cyclotron) with an azimuthally symmetric magnetic field [23] and an isochronous superconducting cyclotron with an azimuthally varying magnetic field [21] have been designed for proton therapy in 1990 and in 1993, respectively. The European EULIMA group proposed a separated sector superconducting cyclotron for light-ion therapy (carbon, oxygen and neon).

The distinct differences between conventional solidpole (such as Harvard 160 MeV synchrocyclotron, Berkeley 184-inch synchrocyclotron, etc.) and sectored FM cy-

clotrons (such as Uppsala cyclotron) mainly are [32]: (1) The use of sectors improves vertical focusing. (2) The reduced rf frequency modulation band, provided by a radially increasing magnetic field, implies a likely increase in capture efficiency in the central region, in dee voltage, and in modulation rate.

It is important to recall the well-known characteristic of synchrocyclotrons, namely, that the RF frequency is made to decrease as the particles gain energy in order to match the decreasing frequency of revolution of the ideal, synchronous projectile. Particles, which start too early or too late from the source slit relative to the synchronous projectile, fail to clear the central region and are thus not captured into stable acceleration orbits. The synchrocyclotron thus sacrifices performance in the form of a low duty cycle and smaller current relative to that of isochronous cyclotrons, in order to provide for the relativistic increase in mass of the accelerated particles. But since a 10 nA proton beam current with 100 Hz duty cycle is enough for cancer therapy, and the variable energy requirement for fixed energy machines like cyclotrons could be realized using the degrader (variable thickness absorbers), superconducting synchrocyclotrons should be easily able to meet the medical requirements.

1.5 Using the K500 Cyclotron to Produce 250 MeV Protons

The isochronous operating range of the K500 cyclotron is bounded by the bending limit $K_{bend} = 500MeV(\frac{T}{A} \leq K_{bend}(\frac{Q}{A})^2)$, by the focusing limit $K_{foc} = 160MeV(\frac{T}{A} \leq K_{foc}(\frac{Q}{A}))$ [33], and by the low field limit corresponding to the $\nu_r + 2\nu_z = 3$ resonance [34]. The bending limit is determined by the field rigidity $B\rho$ maximum. The focusing limit comes from the fact that when the flutter is produced by the aligned magnetic moments of iron sector, as in the K500, the iron becomes fully saturated as the magnetic field is increased, so that the difference between the hill field and the valley

field in turn approaches a constant value; the ratio of the hill field to the valley field (the "flutter") then decreases as the field is increased so that the vertical focusing becomes weaker; ultimately at some field value, the vertical focusing becomes too weak and therefore places a limit on the regime of useful fields [33]. The low field limit $B_o \geq 30$ kG derives from the $\nu_r + 2\nu_z = 3$ resonance which, at low field in a three sector cyclotron (such as the K500), prevents the beam from reaching the extraction radius without large vertical blow-ups. The K500 in isochronous mode would then work only marginally as a proton therapy accelerator due to the low field limit and to the focusing limit which sets the maximum energy for protons in isochronous mode at 160 MeV [35]. In order to boost the final proton energy to 250 MeV and push the resonance radius further outward, the isochronism must be abandoned; a synchrocyclotron conversion of the MSU K500 cyclotron turns out to be a palatable and economical plan. It is without doubt much less expensive to utilize an existing facility than to build a new one. The technical feasibility of the required K500 modifications are reviewed in following sections of this thesis.

1.6 Overview

The cyclotron orbit behavior is usually divided into that of central region, intermediate region and extraction region. In practice, the orbit problems in the intermediate radius region are usually minor [36], as will be seen in Chapter 3.

As was pointed out by H. Blosser [37], the required control of the internal or external beam quality depends predominately on the design of central region. The crucial problems in the central region of an SC with a closed source are those of capture efficiency, space charge losses, radial oscillation amplitude build-up, and source chimney clearness [38]. A central region design study for the K500 conversion was

undertaken by S. Snyder [39] in a study paralleling the extraction studies described herein; satisfactory central region configurations were achieved by Snyder, and this topic will therefore not be discussed further herein.

Beam extraction is much difficult in a high field synchrocyclotron [23] since: (1) The turn spacing varies in proportion to the energy gain per turn and inversely with the average magnetic field strength. and (2) To the extent that electric field is utilized in the proposed extraction system to offset part of the high magnetic field, the required electric field becomes more difficult to achieve, as the magnetic field is increased. Therefore, detailed design of the extraction system is a critical subject in considering the feasibility of converting the K500 to a sector-focused synchrocyclotron.

It is obviously better to use existing components if they will do the job. Therefore, the extraction systems studied for this conversion assume using existing K500 extraction components. (A detailed description of the K500 cyclotron extraction system can be found in Ref. [40].)

Three different extraction methods are explored in this thesis. (1) The traditional method of synchrocyclotron regenerative deflection uses two magnetic disturbances, a regenerator (a positive gradient bump) and a peeler (falling fringe field), to produce a $\cos 2\theta$ field perturbation, and induces radial oscillations with exponential increasing amplitude [41]. (2) The $\nu_r = 1$ excitation extraction system employs a first harmonic bump to make the orbits drift to an outward flowing asymptote at the $\nu_r = 1$ "stop band" (i.e. an energy interval where no closed orbit exists) [42]. and (3) Precessional extraction, in which a smaller first harmonic field bump, is used to produce a coherent precession of the desired amplitude as the beam accelerates through the $\nu_r = 1$ resonance and as a result of this precession, post-resonance acceleration gives enhanced radial separation to assist with clearing the septum [43].

Relevant background details of cyclotrons and of the K500 in particular are provided in Chapters 2, 3, 4 and 5. The regenerative extraction process is discussed in Chapter 6, while excitation of the $\nu_r = 1$ resonance mechanism and the precession method are described in Chapters 7 and 8, respectively.

Chapter 9 gives conclusions and summary. We find that the regenerative method gives rise to the best extraction performance and this K500 adapted synchrocyclotron should provide 5-30 nA of 250 MeV protons, which comfortably meets the beam requirements of cancer therapy.

Chapter 2

Basic Orbit Theory and Numerical Codes

The first section of this chapter reviews intuitive explanations and insights as to the basic and important properties of closed orbits. This is followed by sections which review the numerical codes used in the extraction studies which are the main focus of this thesis. The "equilibrium orbit" (EO) code is explored rather fully because the numerical methods in it also form the key components of other NSCL orbit codes. The Z^4, Charge Sheet and DEFLZ800 are described in a less detailed way.

2.1 Theoretical Calculation of Focusing Frequencies

2.1.1 Kerst and Serber Equations

Kerst and Serber in 1941 [44] developed first-order expressions for the particle position as a function of time in an axially symmetric magnetic field, $B(r, \theta, z) = B(r, z)$. The radial equation in the median plane is

$$m\ddot{r} = mr\dot{\theta}^2 + qr\dot{\theta}B_z(r) \tag{2.1}$$

Closed orbits or equilibrium orbits are those which repeat upon traversing an azimuth of 2π. In an axially symmetric field with a z = 0 plane of symmetry, the closed orbits are circular and located in the z = 0 plane, the "median plane" of the magnet. In such a field $B(r,\theta,z) = B(r,z)$, the equilibrium radius satisfies $r = qB(r,z=0)/p$.

For other orbits, the radius can be written in terms of small oscillations about the closed $r = r_o$ orbit, namely:

$$r(t) = r_o + x(t), \;\; x \ll r_o \tag{2.2}$$

Expand the field in the small oscillation variable, retaining terms only to the first order.

$$B_z(r) = B(r_o) + x \cdot \frac{dB}{dr}|_{r=r_o} + \cdots \tag{2.3}$$

Express $\dot{\theta}$ in terms of r, $\dot{r}$ and constant v^2, yielding

$$\dot{\theta} = \sqrt{\frac{v^2 - \dot{r}^2}{r^2}} \sim \omega_o(1 - \frac{x}{r_o}) \tag{2.4}$$

$$\omega_o \equiv \frac{v}{r_o} \tag{2.5}$$

Substitute the expressions for $r(t), B_z$ and $\dot{\theta}$ into the equation of radial motion and keep only the first order terms. This procedure leads to the Kerst-Serber equation for radial motion:

$$\ddot{x} + \omega_o^2(1+k)x = 0 \tag{2.6}$$

where $k = \frac{r}{B}\frac{dB}{dr}$. Define natural frequency units

$$\nu_r \equiv \frac{\omega_r}{\omega_o} = \sqrt{1+k} \tag{2.7}$$

The linear oscillation in r about r_o can be written as

$$x = A_r cos\, \nu_r \theta \tag{2.8}$$

$$\theta = \omega_o t \tag{2.9}$$

where A_r is the amplitude of radial betatron oscillation. The corresponding solution for the radius of the particle in real space is

$$r(t) = r_o + A_r cos\, \nu_r \theta(t) \tag{2.10}$$

Similarly, the Kerst-Serber equation for the axial motion and its solution are

$$\ddot{z} + \nu_z^2 z = 0 \tag{2.11}$$

$$z = A_z cos\, \nu_z \theta \tag{2.12}$$

$$\nu_z^2 = -k \tag{2.13}$$

where A_z is the amplitude of the vertical betatron oscillation.

2.1.2 Radial Stability

The necessary conditions for radial stability in an axially symmetric magnetic field, that is, the circumstances under which an ion, if displaced radially from the equilibrium orbit, will tend to return to it rather than move away from it, are derived as follows. Locally, this axial symmetric magnetic field can be written approximately as

$$B_z(r) \doteq B_z(r_e)(\frac{r}{r_e})^k \tag{2.14}$$

where r_e is the radius of equilibrium orbit and k is field index. In addition, at every instant the electromagnetic force qvB supplies the centripetal force mv^2/r needed for a circular motion. Thus for equilibrium we must have

$$\frac{mv^2}{r_e} = qvB_z(r_e) \tag{2.15}$$

If $k > -1$, then at $r > r_e$ the magnetic force exceeds the centripetal force needed for an orbit of radius r so that the ion is driven inward towards the equilibrium path, while at $r < r_e$ the particle is forced outward toward r_e. This is the condition for radial stability. It is apparent that the radial focusing force will be stronger the more the field increases - that is, the larger the value of the field index k.

Considering the nonlinear driving force F acting on the radial motion in a three sector field, we shall write by omitting higher order terms in F [45],

$$F = cx^2 cos3\theta \tag{2.16}$$

where c is a constant characterizing the strength of the force. When the defocusing force F just balances the linear attracting force which is proportional to field index k, we thereby obtain the threshold amplitude A_c of stable motion by treating F as a perturbation on the linear motion.

$$A_c \propto \mid \nu_r - 1 \mid \tag{2.17}$$

2.1.3 Axial Stability

For a radially decreasing field, $k \leq 0$, and accompanying this condition is an outward bulging curvature of the magnetic field lines. The force which acts on the projectile is perpendicular both to the field and to the velocity of the ion. Because of the outward bowing of the field lines, the radial component of the field will supply an

axial focusing force which drives the ions back towards the mid-plane. On the other hand, if the field increases outward, $k > 0$, the lines of force bulge towards the center and the forces are such as to produce axial instability.

Up to the present point, the problem of stability has been approached by considering the action of the magnetic field upon a single ion. In actuality, every particle travels in the company of a great many similar particles, and these exert electric and electromagnetic forces on each other.

The assembly of particles accelerated in a continuous wave (CW) cyclotron can be represented as a "pie" shaped distribution, i.e. fixed azimuthal width with continuous distribution of charge density in the vicinity of the median plane from the initial radius to the full one. Assuming a uniform distribution of charge density inside the pie shaped slice (which is quite a good approximation since the turn length increases with r while the turn separation decreases as 1/r), the electric force can be calculated using the Gauss theorem by neglecting edge field. When the electrostatic force of repulsion exceeds the attractive magnetic force, the axial instability occurs. Under these assumptions, the space charge limit current I_{cw} in CW cyclotrons is [36] [46]

$$I_{cw} = 2h\,\epsilon_o\,\omega_o\,\nu_{zo}^2\,\frac{E_1}{q}\,\frac{\Delta\phi}{2\pi} \tag{2.18}$$

where $2h$ is the beam's full height, ϵ_o the permittivity of free space, ω_o the ion orbital frequency, ν_{z0} the single particle axial focusing frequency in natural frequency unit, E_1 the energy gain per turn, q the ion charge, and $\Delta\phi$ the beam azimuthal width.

In a synchrocyclotron the axial space charge limit is modified because the beam is pulsed. The radio frequency decreases in a synchrocyclotron in order to match the change in the frequency of revolution of the ideal synchronous ion due to relativistic mass increase with energy during acceleration process. Once the frequency has reached its minimum value, corresponding to the final energy, it has to increase

again to start a new cycle of acceleration. The total time spent to complete one RF modulating cycle is called the RF modulation period $T_m = 1/f_m$, the corresponding modulation frequency denoted f_m. Consequently, only particles which start in a time window, the "capture time" Δt, relative to the starting time of the ideal synchronous ion will be caught into phase stable oscillations and be accelerated to final energy owing to the process of RF modulation. Defining the capture efficiency as $\epsilon_c = \Delta t/T_m$, the axial space charge current limit I_{sc} in a synchrocyclotron can then be written as

$$I_{sc} = \epsilon_c \cdot I_{cw} \tag{2.19}$$

2.1.4 The Smooth Approximation

Analytic determination of focusing frequencies in a general azimuthal-varying-field (A.V.F.) machine is quite complicated. The analytical techniques used by different authors to obtain solutions involve some approximations and derive the answer in the form of infinite series.

K. R. Symon [9] derived analytic expressions for the focusing frequencies by applying the "smooth approximation" method (i.e. assuming that the betatron wavelengths are long in comparison with the sector length). The formulae contain only the leading terms and are rather crude for 3-sector machines but they do shed insight on how the field parameters determine the focusing frequencies. The formulae are

$$\nu_r{}^2 = 1 + k + \cdots \tag{2.20}$$

$$\nu_z{}^2 = -k + \frac{N^2}{N^2 - 1} F(1 + 2tan^2\zeta) + \cdots \tag{2.21}$$

where $k = \frac{R}{<B>} \frac{d<B>}{dR}$ (the average field index), $< B >$ is the azimuthal average axial field along the particle orbit, R is the radius of the equivalent circle whose circumference is equal to the orbit length, N is the sector number (3 for the K250 synchro-

cyclotron), F is the magnetic flutter at radius R and is defined by $F = \frac{<B^2>-<B>^2}{<B>^2}$, and ζ is the spiral angle defined in Figure 2.1.

2.1.5 Thomas Principle

The purpose of this subsection is to give qualitative explanations for Thomas focusing, which says that it is possible to employ a magnetic field which increases with increasing radius but yet permits the orbits to exhibit axial as well as radial stability.

Imagine a machine in which the pole faces are built so that the gap between the poles becomes alternately larger and smaller as one goes around the machine. Because the magnetic field is approximately inversely proportional to the axial gap, the field varies with azimuth; regions where it is high are colloquially known as hills and where it is low as valleys. Because of this azimuthal change in field strength, there is an azimuthal curving of the field lines so that they are convex towards the centers of the valleys. In a field of this sort the equilibrium orbit of a particle weaves back and forth about a circle, bending more sharply in the hills, less sharply in the valleys, and forming a scalloped path. The non-zero radial velocity v_r interacts with the azimuthal field B_θ associated with the bulging field lines on the boundaries between hills and valleys. Therefore an axial force is produced which turns out to be directed always toward the median plane - flutter focusing.

Suppose that the boundaries between hill and valley are spiraled. Then at every boundary the fringing field has a radial component B_r, with a gradient that points in at one edge and out at the other. In passing through these radial fields, a particle with azimuthal velocity v_θ will experience a net axial focusing force produced from focusing at one boundary and defocusing at the other - alternating gradient focusing. In addition, taking account of the different path lengths in the focusing and defocusing fields due to orbit scalloping, gives rise to another focusing force - Laslett focusing.

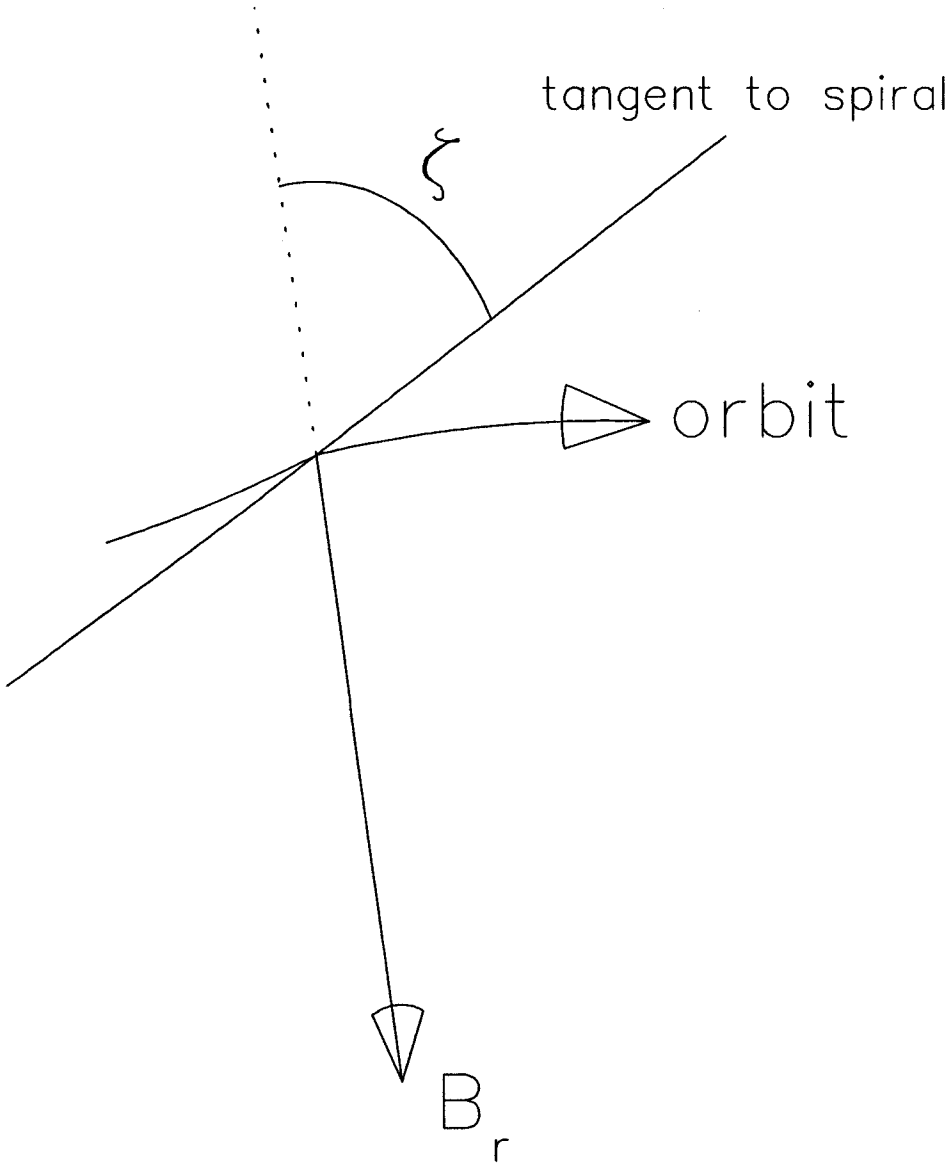

Figure 2.1: Field components and the relation of the spiral angle ζ to the radius of the orbit and to the tangent of the spiral.

The alternating gradient focusing and the Laslett focusing add to give a doubled focusing effect - the factor 2 multiplying the $tan^2\zeta$ term in Equation 2.21.

2.2 Equilibrium Orbit (EO) Code

The important properties of the closed orbits and of the linear radial and vertical oscillations about them can be obtained accurately by using NSCL EO code, developed by M. M. Gordon [47]. Given the median-plane magnetic field in polar coordinates, the program uses direct numerical integration of the canonical equations of motion, together with special iteration and extrapolation procedures, to compute the equilibrium orbits. After the closed orbits are found, the program calculates various properties of the orbit including the linear radial and vertical oscillations, and period about this orbit. For each energy the program searches for and locates the closed orbit by finding a solution of the equations of motion for which r, p_r satisfy the periodicity condition. This is achieved by starting with an initial guess for r and p_r and then integrating the canonical equations of motion for one period. The error in the closure is then used to compute new r, p_r guesses and the process is repeated until the closure meets a predetermined requirement, or a preset number of iterations have been performed. For the first energy value the initial guess is input. For subsequent energy values the initial guess is extrapolated from the previous solutions.

A typical ν_r and ν_z vs. radius calculated in the K250 perfect field (which will be presented in a later chapter) with the smooth approximation (Symon's analytic formula) and with the EO code are shown in Figure 2.2 for comparison. The formulas show good agreement with computer results except at the outer edge of the pole tips. The disagreement probably arises due to the flutter derivatives [48] which are usually quite large near the pole tip outer edge.

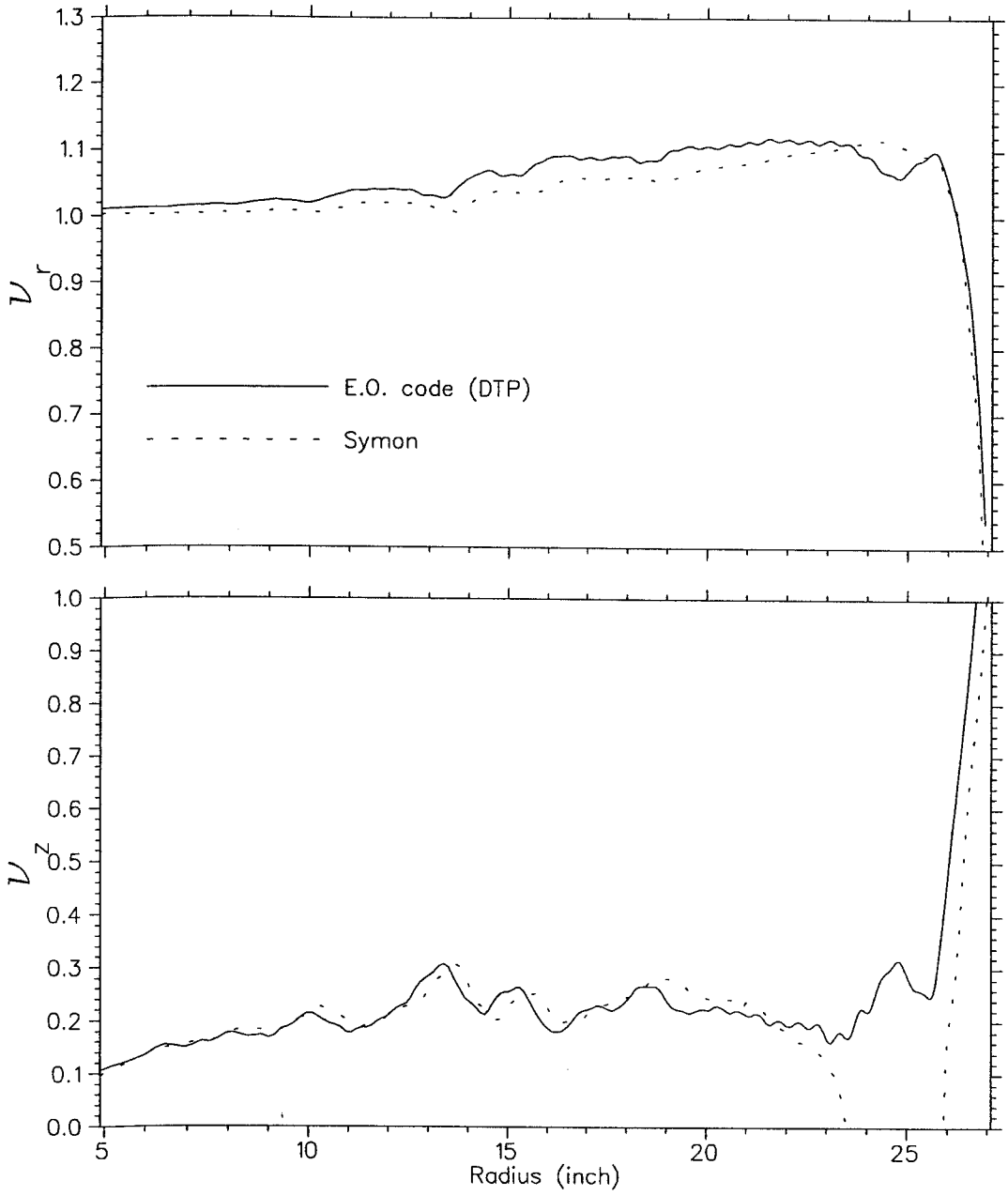

Figure 2.2: Plots of ν_r and ν_z vs. radius calculated in the K250 120^0 field. Solid curves are computer results, broken curves are Symon's formula (Equations 2.20 and 2.21)

.

2.2.1 DTP Field Interpolation Scheme

The magnetic field of the K500 cyclotron was measured on a polar grid with steps $0.5''$ and 1°. Lacking an analytical function to describe the magnetic field, interpolation in the measured grid is used to obtain fields and derivatives at intermediate points as needed for the particle orbit tracking calculations. It is apparent that both the interpolation method and the step size of the stored magnetic field are crucial to the accuracy of the field value and derivatives. The double-three-point (DTP) interpolation scheme is the standard method used in most NSCL orbit codes, and the truncation error of this method is therefore analyzed in this subsection.

The DTP is a linearly weighted and uniform spacing ($= \Delta x$) interpolation method. To interpolate between two points x_2, x_3, the left hand neighbor x_1 and the right hand neighbor x_4, are used with x_2 and x_3 to determine a left and right second order polynomial; the interpolated value is the average of these two polynomials weighted according to the distance from x_2 and x_3, respectively. This method is simple and, moreover, its first order derivative is continuous; the usual four point, third order polynomial, formula does not give the nice property of continuous first derivative from interval to interval, however, the DTP will not fit the end grid points if used outside the x_2, x_3 interval (whereas the usual four point third order polynomial would).

Looking at the DTP in more details we first note that for a given three even-spacing points in x, there is a unique quadratic polynomial connecting through them. The notation used herein is shown in Figure 2.3 . For the set $(x_1, y_1), (x_2, y_2), (x_3, y_3)$ and the set $(x_2, y_2), (x_3, y_3), (x_4, y_4)$, the quadratic polynomial functions connecting them are denoted as Y_a and Y_b, respectively. Define $r = \frac{x - x_2}{\Delta x}, x_2 \leq x \leq x_3$ (denoted $x \in [x_2, x_3]$), $\Delta x = x_3 - x_2$ and let y = f(x) which describes the exact dependence y on x. Then, basing on Taylor's theorem and taking r = 1/2, the resulting formulas

for interpolation truncation errors are derived approximately as follows.

Y_a can be written as

$$Y_a(x) = \frac{1}{2}(r^2 - r) \cdot y_1 + (-r^2 + 1) \cdot y_2 + \frac{1}{2}(r^2 + r) \cdot y_3 \tag{2.22}$$

The truncation error, ΔY_a, associated with the quadratic formula Y_a, presumably steming mainly from the omission of the terms higher than second order (i.e. $Y_a(x) \cong y_2 + f'(x_2)(x - x_2) + \frac{f''(x_2)}{2!}(x - x_2)^2$), is estimated as follows using Taylor's theorem

$$\Delta Y_a \cong \frac{f'''(\epsilon)}{6}(x-x_1)(x-x_2)(x-x_3) = \frac{f'''(\epsilon)}{6}(\Delta x)^3 r(r-1)(r+1),\ \epsilon \in [x_1, x_3] \tag{2.23}$$

where $f'''(\epsilon)$ denotes $\frac{\partial^3 y}{\partial x^3}\,|_{x=\epsilon}$. Taking r=1/2, yields

$$\Delta Y_a \cong \frac{-f'''(\epsilon)}{16}(\Delta x)^3 \tag{2.24}$$

Similarly, Y_b and its truncation error are

$$Y_b(x) = \frac{1}{2}(r^2 - 3r + 2) \cdot y_2 + (-r^2 + 2r) \cdot y_3 + \frac{1}{2}(r^2 - r) \cdot y_4,$$

$$\Delta Y_b \cong \frac{f'''(\zeta)}{6}(x - x_2)(x - x_3)(x - x_4)\ \ \zeta \in [x_2, x_4]$$

$$= \frac{f'''(\zeta)}{6}(\Delta x)^3 r(r - 1)(r - 2)$$

$$\cong \frac{f'''(\zeta)}{16}(\Delta x)^3_{r=1/2} \tag{2.25}$$

In the orbit programs at our lab,

$$Y \equiv -(r - 1) \cdot Y_a + r \cdot Y_b \tag{2.26}$$

The corresponding error ΔY is

$$\Delta Y = -(r - 1) \times \Delta Y_a + r \times \Delta Y_b$$

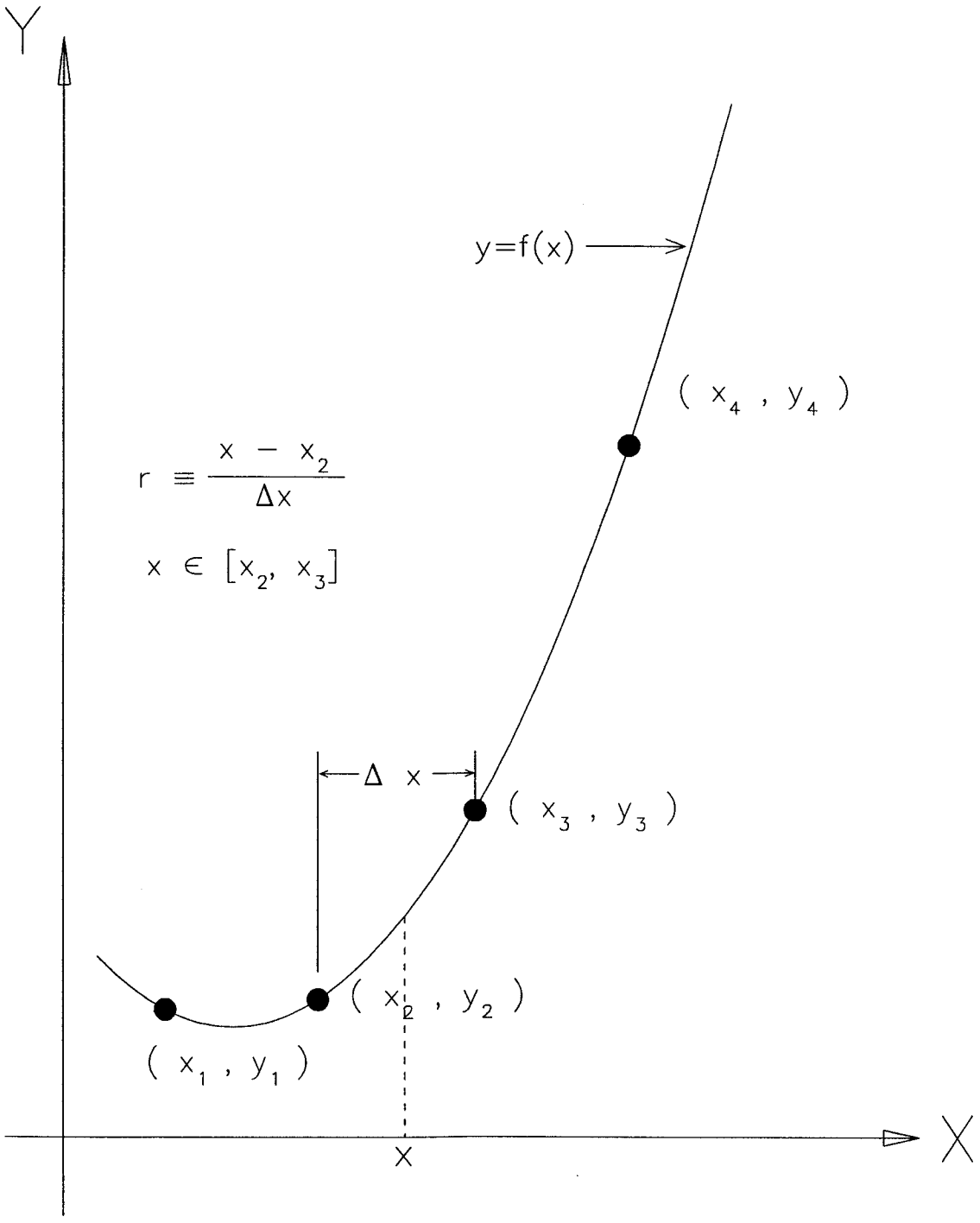

Figure 2.3: Coordinate system used in analysis of the double-three-point interpolation.

$$\cong \frac{1}{2} \times (\Delta Y_a + \Delta Y_b)_{r=1/2}$$
$$\cong \frac{1}{32}(\Delta x)^3[-f'''(\epsilon) + f'''(\zeta)]$$
$$\cong \frac{f''''(\eta)}{16} \times (\Delta x)^4 \ \eta \in [x_1, x_4] \tag{2.27}$$

The first derivative in the orbit program is expressed as, from Equation 2.26

$$\frac{dy}{dx} = \frac{1}{\Delta x}\frac{dy}{dr} = \frac{1}{\Delta x}[(-r^2 + 1.5r - 0.5) \cdot y_1 + (3r^2 - 3.5r) \cdot y_2$$
$$+(-3r^2 + 2.5r + 0.5) \cdot y_3 + (r^2 - 0.5r) \cdot y_4] \tag{2.28}$$

In conclusion, the interpolation error in the DTP method is proportional to the fourth power of the step size. (A comparison of the DTP method with an eleven point finite difference method, which is expected to be more realistic and accurate, is given in Chapter 4).

2.2.2 Runge-Kutta Integration

The fourth-order Runge-Kutta method, which is known to solve the coupled first order differential equations very accurately, has been employed in NSCL orbit programs to integrate the equations of motions. Its truncation error is proportional to the fifth power of the step size at each integration step. To demonstrate the essence of this method and capture the main ideas as simply as possible, the integration procedure will be illuminated for one variable only. The corresponding differential equation is

$$\frac{dy}{dx} = f(x, y) \tag{2.29}$$

A variable k is defined as

$$k_1 = hf(x_o, y_o)$$
$$k_2 = hf(x_o + \frac{h}{2}, y_1)$$

$$k_3 = hf(x_o + \frac{h}{2}, y_2)$$
$$k_4 = hf(x_o + h, y_3) \tag{2.30}$$

where h is the integration size and x_o, y_o are the values at the beginning of the step. This method is iterative; the derivative equation is evaluated four times during the step. For each iteration, k is evaluated at the y value resulting from the previous one. At the same time, each new y value is calculated by adding a weighted sum of the k values to either the initial y or the one from the previous iteration; final forms are shown here.

$$y_1 = y_o + \frac{1}{2}k_1$$
$$y_2 = y_1 - \left(1 - \sqrt{\frac{1}{2}}\right) k_1 + \left(1 - \sqrt{\frac{1}{2}}\right) k_2$$
$$y_3 = y_2 + \left(\frac{1}{2} - \sqrt{\frac{1}{2}}\right) k_1 - k_2 + \left(1 + \sqrt{\frac{1}{2}}\right) k_3$$
$$y_4 = y_3 + \frac{1}{6}\left[k_1 + 2\left(1 + 2\sqrt{\frac{1}{2}}\right) k_2 - 4\left(1 + \sqrt{\frac{1}{2}}\right) k_3 + k_4\right] \tag{2.31}$$

At the end of each integration step, the resulting value of $y = y_4$ at $x_o + h$ provides the initial conditions in the next cycle and the entire process is repeated.

2.2.3 Iteration Scheme

This iteration process in EO code is an extension of the familar Newton method. Symbols, definitions and derivations are adopted from M. M. Gordon's paper [47] in this and the following subsection.

The canonical equations of motion in cylindrical coordinates in the given median

plane field $B(r,\theta)$ with θ as the independent variable are

$$\frac{dr}{d\theta} = \frac{rp_r}{p_\theta}, \tag{2.32}$$

$$\frac{dp_r}{d\theta} = p_\theta + qrB(r,\theta). \tag{2.33}$$

The values of r and p_r as functions of θ are calculated by integrating these equations of motion using the Runge-Kutta method. Searching for a closed orbit then reduces to finding the pair of initial values (r_i, p_{ri}) at $\theta = \theta_i$ which satisfy the periodicity condition $r(\theta_f) = r(\theta_i)$ and $p_r(\theta_f) = p_r(\theta_i)$, where $\theta_f = \theta_i + \theta_o$ and θ_o is the periodicity. For example, $\theta_o = 360^0/N$ in a field with N sectors and no imperfection.

The linear radial oscillation equations relative to a reference orbit (r_o, p_{ro}) are obtained by making the substitution $r \rightarrow r_o + x$, $p_r \rightarrow p_{ro} + p_x$ into the median plane equations of motion and retaining linear terms. The resulting transfer matrix is denoted as $X(\theta, \theta_i)$ which determinant is equal to 1 from the Liouville theorem.

The errors in the trial values of (r_i, p_{ri}) are calculated from

$$\xi_1 = r(\theta_f) - r_i \tag{2.34}$$

$$\xi_2 = p_r(\theta_f) - p_{ri} \tag{2.35}$$

If the errors are not both zero to within a preset tolerance, as required by the periodicity condition, we proceed to calculate improved trial values. To do so, we assume the true closed orbit differs from the trial orbit only in first order; then we have

$$\begin{pmatrix} r_c \\ p_{rc} \end{pmatrix}_\theta = \begin{pmatrix} r \\ p_r \end{pmatrix}_\theta + X(\theta, \theta_i) \begin{pmatrix} \delta r_i \\ \delta p_{ri} \end{pmatrix} \tag{2.36}$$

so that $r_c(\theta_i) = r_i + \delta r_i$ and $p_{rc}(\theta_i) = p_{ri} + \delta p_{ri}$. Thus (r_c, p_{rc}) and (r, p_r) are, respectively, the coordinates of the closed orbit and trial orbit (already computed), and δr_i and δp_{ri} are the correction being sought.

Applying Equation 2.36 at $\theta = \theta_i$ and $\theta = \theta_f$, and taking the difference, we then obtain

$$0 = \begin{pmatrix} \xi_1 \\ \xi_2 \end{pmatrix} + [X(\theta_f, \theta_i) - I] \begin{pmatrix} \delta r_i \\ \delta p_{ri} \end{pmatrix} \tag{2.37}$$

which then yields the corrections and provides improved values for the initial conditions. These values are then used to repeat the entire process until the convergence tolerance is satisfied (or until an "excessive number of trials" fault is triggered).

2.2.4 Calculation of ν_r, ν_z, and Orbit Period

From the canonical equations of motion for the linear radial and vertical oscillations, the transfer matrices of the linear oscillations $X(\theta, \theta_i)$ and $Z(\theta, \theta_i)$ can be obtained using the values of r, p_r and p_θ of the median plane closed orbit. This $X(\theta, \theta_i)$, together with $Z(\theta, \theta_i)$, provide complete information about the linear betatron oscillations.

We simplify the discussion by letting y stand for either x or z. Thus the matrix Y stands for X or Z, while ν_y stands for either ν_r or ν_z. $Y(\theta_f, \theta_i)$, $\theta_f = \theta_i + \theta_o$, is recognized as the transfer matrix for one complete period starting at θ_i. Hence, in accordance with Floquet's theorem, the eigenvalues of this matrix are

$$\lambda = exp(\pm i\sigma) \tag{2.38}$$

where

$$\sigma = \nu_y \theta_o \tag{2.39}$$

$$cos\sigma = \frac{1}{2}[Y_{11}(\theta_f, \theta_i) + Y_{22}(\theta_f, \theta_i)] \tag{2.40}$$

Thus, if $\mid cos\sigma \mid \leq 1$, then σ is real and the motion is stable, but if $\mid cos\sigma \mid > 1$, then σ is complex and the motion is generally unstable.

In keeping with general practice, we write the matrix $Y(\theta_f, \theta_i)$ in the standard form,

$$Y(\theta_f, \theta_i) = I cos\sigma + J(\theta_i) sin\sigma \tag{2.41}$$

where I is the unit matrix, and

$$J(\theta_i) = \begin{pmatrix} \alpha_i & \beta_i \\ -\gamma_i & -\alpha_i \end{pmatrix} \tag{2.42}$$

which defines the parameters α_i, β_i and γ_i. These quantities are related to the known matrix elements by

$$\begin{aligned} \alpha_i sin\sigma &= \frac{1}{2}[Y_{11}(\theta_f, \theta_i) - Y_{22}(\theta_f, \theta_i)] \\ \beta_i sin\sigma &= Y_{12}(\theta_f, \theta_i) \\ \gamma_i sin\sigma &= -Y_{12}(\theta_f, \theta_i) \end{aligned} \tag{2.43}$$

When σ is real, by assuming $\beta_i > 0$, the value of $\sigma = \nu_y \theta_o$ is determined by Equations 2.40 and 2.43. When σ is complex, the program uses $\mid cos\sigma \mid$ to find the imaginary part of ν_r and ν_z.

The differential equation for the time t, which is canonical, is written as

$$\frac{dt}{d\theta} = \frac{r}{\frac{p_\theta}{p} \cdot v} \tag{2.44}$$

The orbit period is obtained by integrating the above equation for one complete period from t = 0 at $\theta = \theta_i$.

2.3 Magnetic Charge Sheet Program

This program [49] calculates the median plane field produced by the magnetic extraction apparatus, assuming that the iron is uniformly magnetized in the vertical

direction. The uniform magnetization assumption is quite accurate at the high field levels employed in superconducting cyclotrons and allows one to calculate the median plane field generated by the saturated iron in terms of a simple surface current flowing in horizontal loops around the sides of each piece of steel; this then leads to a field formula involving a single line integral around the closed-current contour. The scale factor B_o is set internally to 21.4 kilogauss. As reported by Gordon [50] for standard magnet steel, the assumption of saturation works very well for external field all the way down to about 6 kilogauss. Therefore, the accuracy of these calculations are expected to be reasonably satisfactory in superconducting machines.

Following the analysis of M.M. Gordon [49], consider a piece of iron having horizontal surface $z = z_1$ at bottom and $z = z_2$ at top ($z_2 > z_1 \geq 0$). For each piece given above the median plane, there is a matching piece symmetrically located below the plane. The median plane field produced by these two pieces of saturated steel is denoted by B_{zoi}. From Maxwell equations (for example, in the book Classical Electrodynamics by J. D. Jackson), the saturated blocks of iron with uniformly distributed magnetic moment are equivalent to uniform currents ($\vec{j} = \vec{M}_o \times \vec{n}$, $\mu_o M_o = B_o = 2.14$ tesla) on the surface parallel to the external field. After some manipulation, the B_{zoi} can be written as:

$$B_{zoi} = \frac{B_o}{2\pi}\{\oint[1 - \frac{z_1}{R_o}] \times \frac{(y-y')dx' - (x-x')dy'}{(x-x')^2 + (y-y')^2}_{z'=z_1} \tag{2.45}$$

$$- \oint[1 - \frac{z_2}{R_o}] \times \frac{(y-y')dx' - (x-x')dy'}{(x-x')^2 + (y-y')^2}_{z'=z_2} \}$$

where $r = (x, y, z = 0)$ is the point at which the magnetic field to be evaluated, and $r' = (x', y', z')$ gives the location of a particular current element. The distance R_o is given by

$$R_o = ((x-x')^2 + (y-y')^2 + z'^2)^{1/2} \tag{2.46}$$

Making the substitutions

$$x' \to 1/2(x_j + x_{j-1}),\ y' \to 1/2(y_j + y_{j-1}) \tag{2.47}$$
$$dx' \to x_j - x_{j-1},\ dy' \to y_j - y_{j-1},$$

the contour integral is evaluated numerically in this program by simply replacing the integral with a sum over a sequence of n straight-line segments which join the points (x_j, y_j), where j = 0, 1, 2, ..., n. Here, $(x_n, y_n) = (x_o, y_o)$ is required in order that the contour be closed.

Since the integrands involve only simple algebraic expressions, the numerical integration is quite rapid. The accuracy can be tested and improved by systematically increasing n.

The magnetic extraction apparatus under consideration can be subdivided into a finite number of such pieces. The resultant median plane field $B_{zo} = \sum B_{zoi}$ is obtained through superposition by adding up the contributions from all of the divided pieces having flat vertical surfaces.

2.4 General Spiral Gap Code Z^4

The Z^4 orbit code [51] developed by M.M. Gordon is used in the pre-extraction orbit computations. This code calculates the nonlinear effect of the field and the Z motion using a magnetic field Taylor-expanded off the median plane up to fourth order, and provides an accurate evaluation of the important coupling effects between the radial and vertical motion. The median plane magnetic field is required for input and is pre-stored in a polar grid. The field is assumed to have a mid-plane symmetry and the B_z is expanded to Z^4. The rest of the components of the magnetic field, B_θ or B_r, are determined in such a way that $\nabla \cdot B = 0$ is satisfied. The formulas used in

the field expansion are the following

$$B_z = -[B(r,\theta) - \frac{z^2}{2}B'(r,\theta) + \frac{z^4}{24}B''(r,\theta)] \tag{2.48}$$

$$B_r = -z\frac{\partial}{\partial r}C(r,\theta,z) \tag{2.49}$$

$$B_\theta = -\frac{z}{r}\frac{\partial}{\partial \theta}C(r,\theta,z) \tag{2.50}$$

where $C(r,\theta,z) = B(r,\theta) - \frac{z^2}{6}B'(r,\theta)$. Here $B' = LB(r,\theta)$ and $B''(r,\theta) = LB'(r,\theta)$, where L represents the cylindrical two dimensional Laplace operator ($L \equiv \frac{1}{r}\frac{\partial}{\partial r}(r\frac{\partial}{\partial r}) + \frac{1}{r^2}\frac{\partial^2}{\partial \theta^2}$). Thus, B_z has terms of order z^2 and z^4 off the median plane, while B_r and B_θ have z and z^3 terms.

The equations of motion for r, p_r, z and p_z used in the Z^4 orbit code are as follows:

$$\frac{dr}{d\theta} = \frac{rp_r}{p_\theta} \tag{2.51}$$

$$\frac{dp_r}{d\theta} = p_\theta + qrB_z - q\frac{rp_z}{p_\theta}B_\theta \tag{2.52}$$

$$\frac{dz}{d\theta} = \frac{rp_z}{p_\theta} \tag{2.53}$$

$$\frac{dp_z}{d\theta} = -qrB_r + q\frac{rp_r}{p_\theta}B_\theta \tag{2.54}$$

where (B_r, B_θ, B_z) are the orthogonal polar components of the total field, obtained from Equations 2.48, 2.49 and 2.50 by applying the DTP method on pre-stored median plane maps of the field, and of B' and B''. Given the field components, the fourth-order Runge-Kutta subroutine is employed to integrate the equations of motion with respect to θ. The treatment of accelerating gap crossings in the Z^4 code is approximate (impulse approximation), i.e. the particle's energy remains constant until it crosses a gap, and then the energy and momentum change abruptly according to the conditions at the gap. This is an accurate simplification away from the cyclotron central region

due to the fact that $\hat{E}$ field is fundamentally weak relative to $\hat{B}$ field except in the central region and also the $\hat{E}$ field is highly localized spatially.

2.5 DEFLZ800 Code

The DEFLZ800 code [52] is used after the beam enters the extraction system. This program treats only linear vertical motion and calculates the coupling of the radial into the vertical motion, but omits the reverse coupling of vertical into radial. The treatments of electrostatic deflectors and focusing bars is also approximate in this program: The effect of the electric field E is calculated simply by decreasing the median plane field $(-B_z)$ by an amount E/v, where v is the particle's velocity. And the magnetic field inside the aperture of the focusing bar is just determined by two parameters - field bias ΔB and focusing gradient $\partial B/\partial x$.

The DEFLZ800 program is, however, quite "good" and much faster than its complicated counterpart Z^4 code which is supposed to be extremely realistic and therefore very accurate. Comparison of DEFLZ800 runs with Z^4 runs has been done by Marti and Jeon [53] who showed that the difference in central ray position computed by these two codes was less than 100 mils at the exit of the last focusing bar, but DEFLZ800 is roughly one thousand times faster than Z^4. The CPU time in Z^4 for a particle to complete the extraction journey after it enters the channel is about 1 min; it is extremely slow due to the fact that fringe fields of all the extraction devices are taken into consideration [53]. (We still face tradeoff between better calculations and computational cost in spite of the advance of computer today!)

Chapter 3

The K250 Magnetic Field and Its Properties

The choice of main and trim coil currents to give an approximately optimal magnetic field is discussed in this chapter. Following this, the main features of this three-fold-symmetry magnetic field in the K250 synchrocyclotron extraction region are analysed, and properties of the radial phase space are reviewed to display the fundamental performance features of this machine.

3.1 Decision of the K250 Magnetic Field

The general features of the MSU K500 magnet are extensively reported in Ref. [54]. Only some important features will be recalled. A median plane plan view of the K500 cyclotron is given in the upper part of Figure 3.1, and a vertical section view of the K500 magnet is at the bottom. The vertical section is taken along a spiral line centered on a hill and superimposed on a similar valley cross section (center plug not included). The hills have constant axial gap for radii between 3.5″ and 25.75″ and both hills and valleys have an average spiral constant of 1/13 (rad/inch). The two superconducting coils are located radially between 30″ and 35.6″, and the section closer to the median plane is about 1/3 of the total coil height. Thus the two sections

will be referred to as small coil and large coil respectively, and their currents are indicated as I_α and I_β.

There are 13 trim coils located on each spiral sector pole, made of two layers of 5 turns each of 0.25″ square hollow conductor and approximately equally spaced from 3.5″ to 25″ radius. The measured average field ($B_{av}(r) \equiv \int_0^{2\pi} B(r, \theta, z = 0) d\theta/2\pi$) of the trim coils all have a similar form; one of them is shown in Figure 3.2 at excitation 360 A.

The 120° field mapping over the points on the I_α, I_β plane, with all the trim coils turned off, was measured using the flip coil method in the period from December 1980 to March 1981 [54]. It is concluded from this paper that the data have an accuracy of ±0.03% limited mainly by the slow change of the calibration over a period of a few days. The currents and central field for some of the measured points are listed in Table 3.1. The fields anywhere on the I_α, I_β plane are predicted based on the interpolation technique.

The coil current setup in the proposed K250 proton synchrocyclotron is listed in Table 3.2. The corresponding median plane field contour is shown in Figure 3.3. The spiral structure of the hill, the azimuthal variation from hills to valleys, and the field fall-off at the magnetic edge are all shown clearly in this figure.

In the following, the customary Fourier expansion of the magnetic field will be used: Namely

$$B(r, \theta) = B_o(r) + \sum B_n(r) cosn(\theta - \phi_n(r)) \tag{3.1}$$

where $B_o(r)$ is the average field as a function of radius and $B_n(r)$ is the nth harmonic amplitude. For 120^0 field maps, only the third harmonic and multiples thereof are present. The average field, and amplitudes and phases of the third and sixth leading

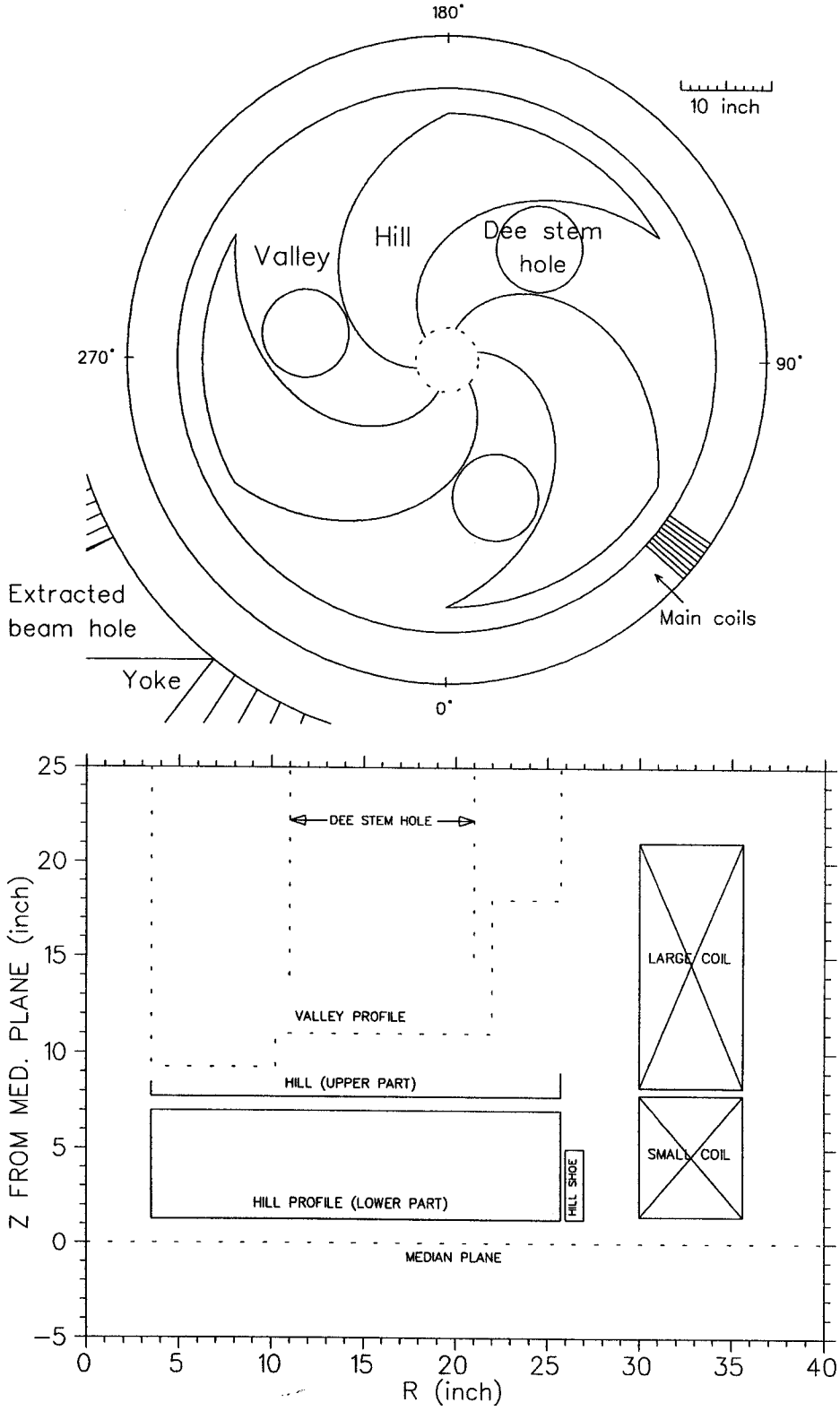

Figure 3.1: Top: median plane plan view of the K500 cyclotron. Bottom: radial profile of the K500 cyclotron through a spiral line centered on a hill and superimposed on a similar valley cross section.

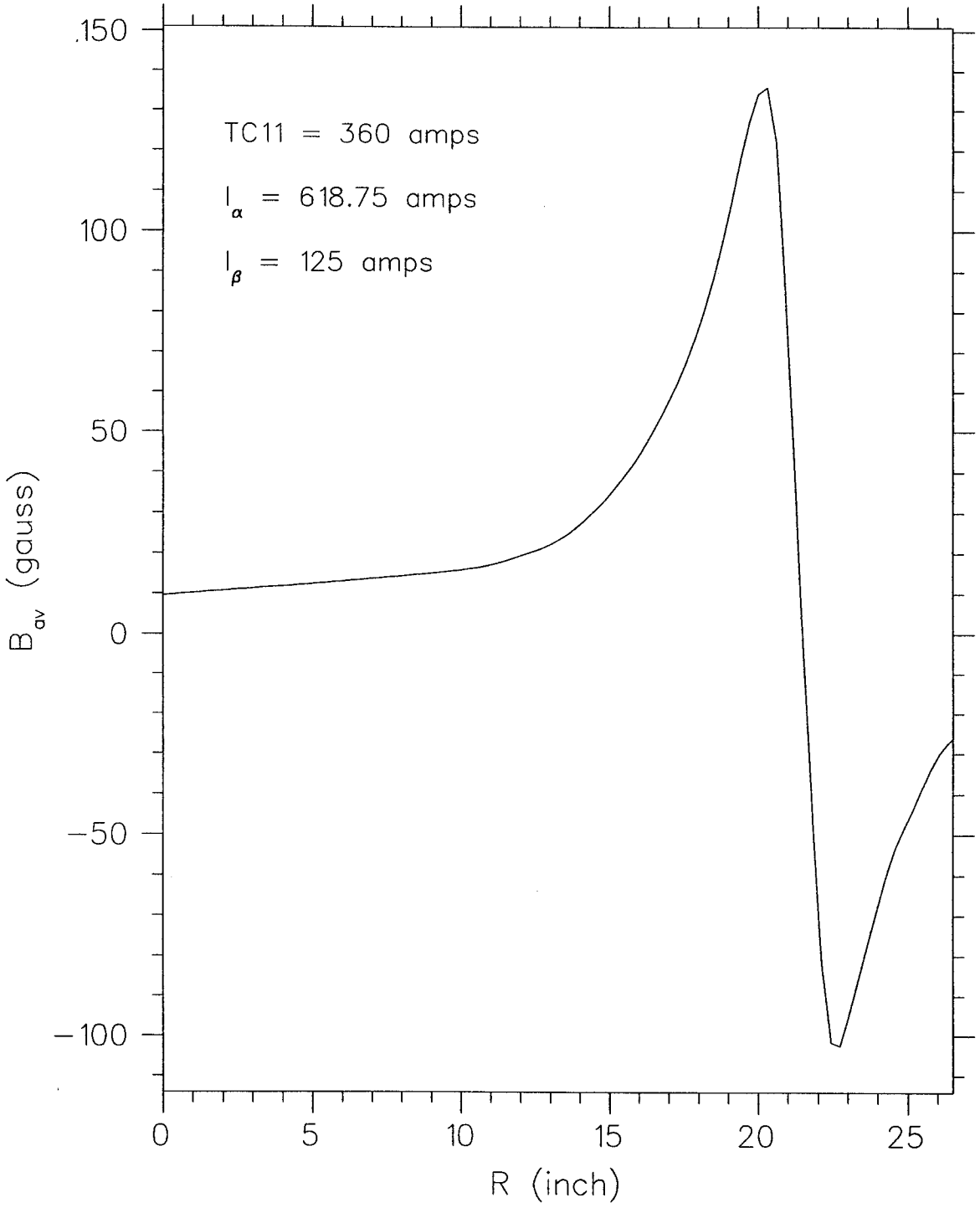

Figure 3.2: Average field ($B_{av}(r) \equiv \int_0^{2\pi} B(r_o, \theta, z = 0) d\theta/2\pi$) at excitation 360 A, equal currents in three sectors, for the trim coil 11, measured at main coil currents (amps) $I_\alpha/I_\beta = 618.75/125$, from Ref. [54].

Table 3.1: Data of 120^o magnetic field maps with trim coil turned off.

Field number	I_α (Amp)	I_β (Amp)	B_o (Kilogauss)
1	450	200	28.9
2	550	100	27.9
3	650	0	26.9
4	487.5	350	34.1
5	537.5	300	33.6
6	587.5	250	33.1
7	687.5	150	32.2
8	525	500	39.1
9	625	400	38.2
10	725	300	37.2
11	562.5	650	44.0
12	662.5	550	43.1
13	762.5	450	42.2
14	600	800	48.8
15	700	700	48.0
16	800	600	47.1

Table 3.2: Coil currents associated with the K250 proton synchrocyclotron.

Coil	Current (ampere)
Large main coil	180
Small main coil	700
Trim coil 1	0
Trim coil 2	0
Trim coil 3	-100
Trim coil 4	-200
Trim coil 5	-300
Trim coil 6	-300
Trim coil 7	-300
Trim coil 8	-300
Trim coil 9	-200
Trim coil 10	-100
Trim coil 11	0
Trim coil 12	100
Trim coil 13	100

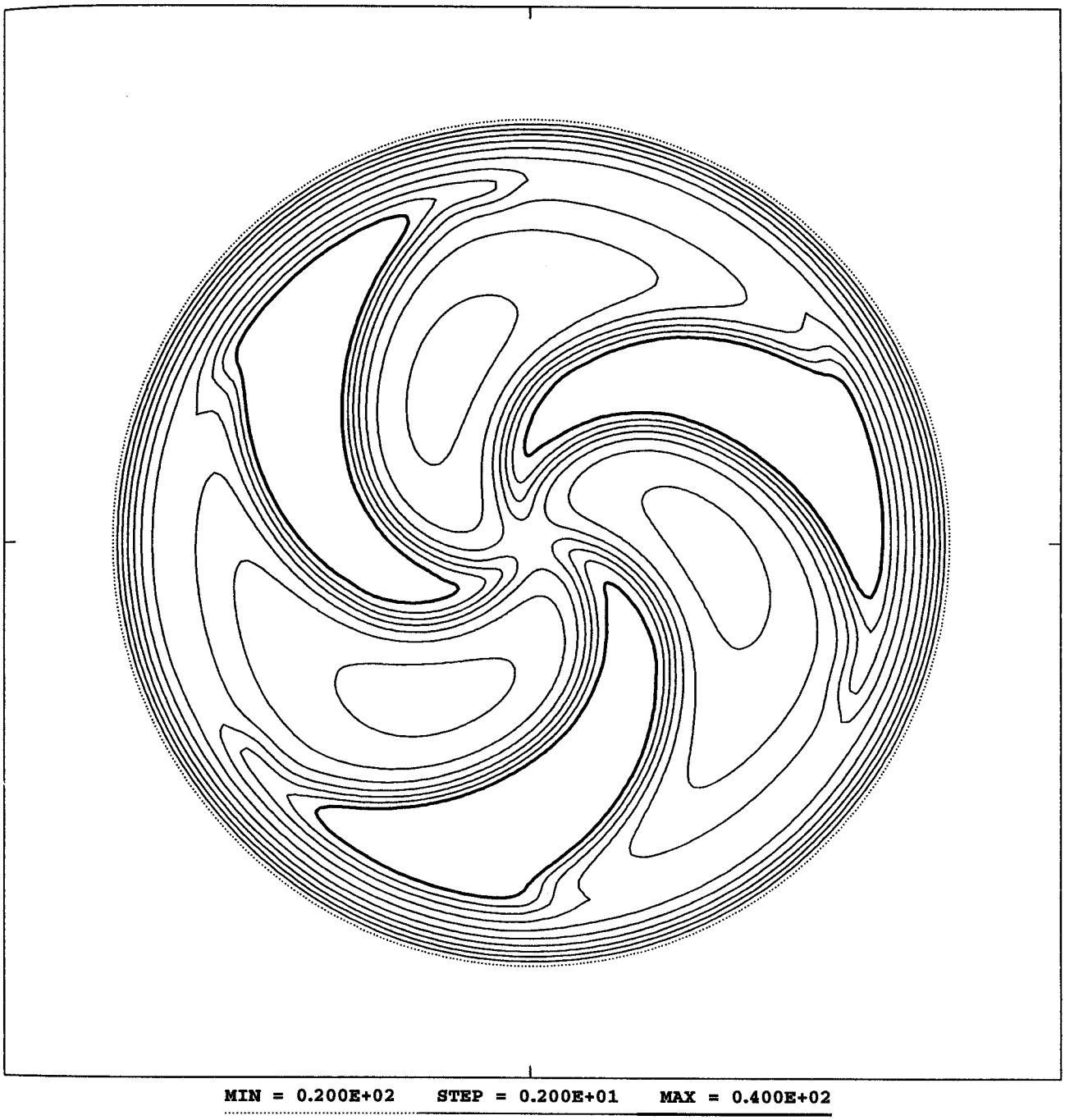

Figure 3.3: Contour plot of the median plane field map of the K250 field. Coil currents are at the values given in Table 3.2. Imperfection field components are omitted so that the plot has exact 120° symmetry. Contour spacing is two kilogauss with the dotted contour at the outside at 20 kilogauss and the double weight contour in the outer part of each hill at 40 kilogauss.

harmonic components as function of radius are given in Figure 3.4. The function $\phi_n(r)(n = 3, 6, \cdots)$ is determined by the spiral curve of the hill (valley).

The excitation $I_\alpha = 700A$, $I_\beta = 180A$ of main coils can sustain 250 MeV protons. Moreover, the associated field is approximately optimal because of the following reasons: (1) It gives acceptable focusing in the intermediate energy region, as will be seen later. (2) Its sharp field edge (Figure 3.4) alleviates the problems of beam extraction. (3) There are several advantages associated with its closeness to isochronous field, namely, the rising magnetic field (Figure 3.4) compared to the falling field [55]:

- The range of frequency modulation decreases which reduces the problems of getting a high repetition rate. The orbital frequency as function of radius and energy, for protons in this field, is given in Figure 3.5.

- With the dee voltage and final energy being fixed, the initial orbit radii are larger so that the ions have a better chance to clear the source, due to lower central magnetic field.

- The reduced frequency range owing to lowering of the central magnetic field decreases the initial $d\nu_{rf}/dt$ as well as ν_{orbit}, and thereby increases the capture efficiency.

All the trim coil currents are well below the maximum current rating of the power supply which is 400 A. The negative sign of trim coil current indicates that the field produced by this trim coil at the center of the magnet is opposite to that of the main coils. The principal purpose of trim coils in such a synchrocyclotron is to adjust vertical focusing locally by changing field derivative, $\Delta\nu_z \approx \frac{-\Delta k}{2\nu_z}$ from smooth approximation. As in Chapter 2, the focusing frequencies ν_r and ν_z are defined as ratios of the actual focusing frequencies, with which linearly displaced orbits oscillate

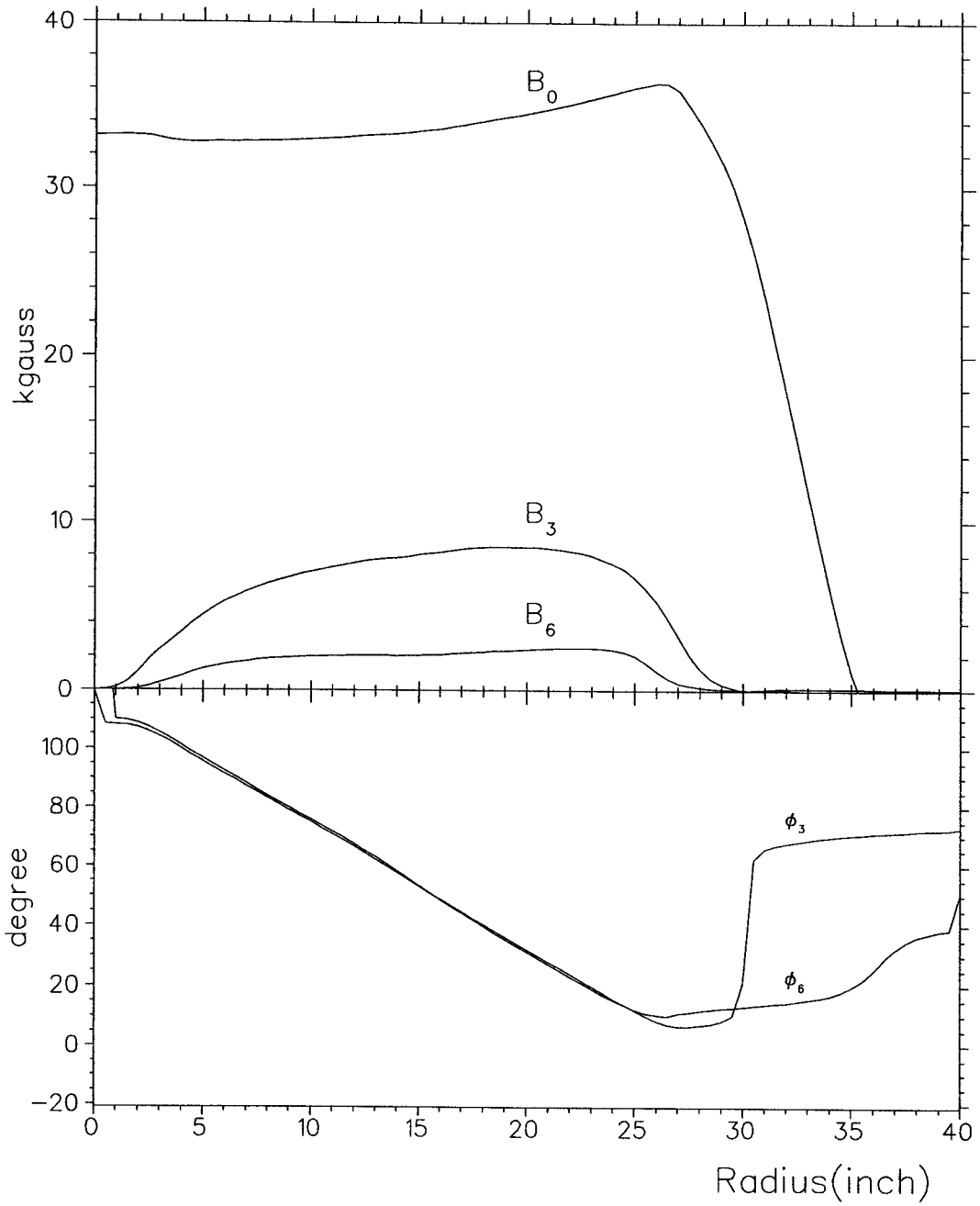

Figure 3.4: Plots of $B_0, B_3, \phi_3, B_6, \phi_6$ of the K250 field vs. radius (coil currents at the values given in Table 3.2).

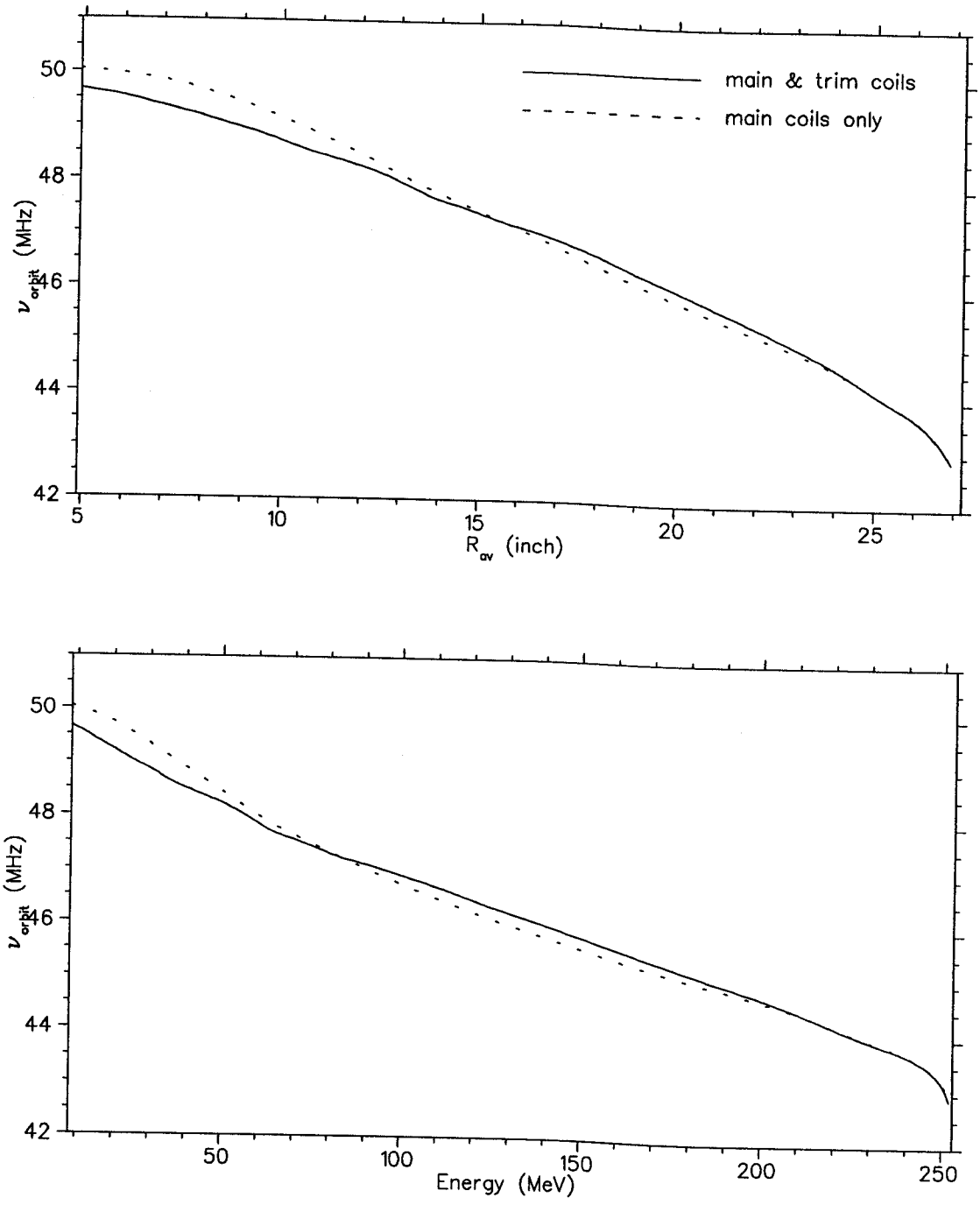

Figure 3.5: Plots of orbital frequency ν_{orbit} as function of radius (top) and energy (bottom) in the K250 synchrocyclotron perfect field. The solid curves are associated with trim coils on, the dotted curves with all trim coils off. Note that an isochronous field gives a constant orbital frequency.

relative to the closed orbit, to the orbital frequency and are hence dimensionless. The numerical results of radial and vertical focusing frequency calculations in the K250 perfect field, with and without trim coils turning on, are shown in Figure 3.6.

The maximum stable radial betatron oscillation amplitude (A_c), the radial distance in the phase space from the equilibrium orbit to the furtherest unstable fixed point, calculated by using the EO code, is plotted as function of energy in Figure 3.7. It is evident that the stability limit is much larger than the beam size in the intermediate radius region. Hence the orbit problem in this region are expected to be minor.

3.2 Radial Phase Space Studies in the K250 120^0 Field

The nature of the extraction process can best be understood by examining radial phase plots which show p_r vs. r for orbits with given energy at some selected azimuthal position. They provide a qualitative insight as to relationships between particle behavior and magnetic field features.

The axially symmetric field is employed in the following argument to provide the insight and intuition to the equilibrium orbits, the final energy and the extraction radius for sector machines. From relation $p/q = \rho B$ (ρ is the instantaneous radius of curvature) and the profile of a B field (upper panel of Figure 3.8), we see that in general for a given p/q, there are two possible closed orbits, if there are any at all (lower panel of Figure 3.8). Such orbits are either stable or unstable according as near neighbor orbits remain close to, or drift away from, the fixed point orbit, respectively. The r_c is the upper limit of extraction radius and ρB_c, at which the related two orbits are collapsed into one closed orbit, corresponds to the maximum energy which the

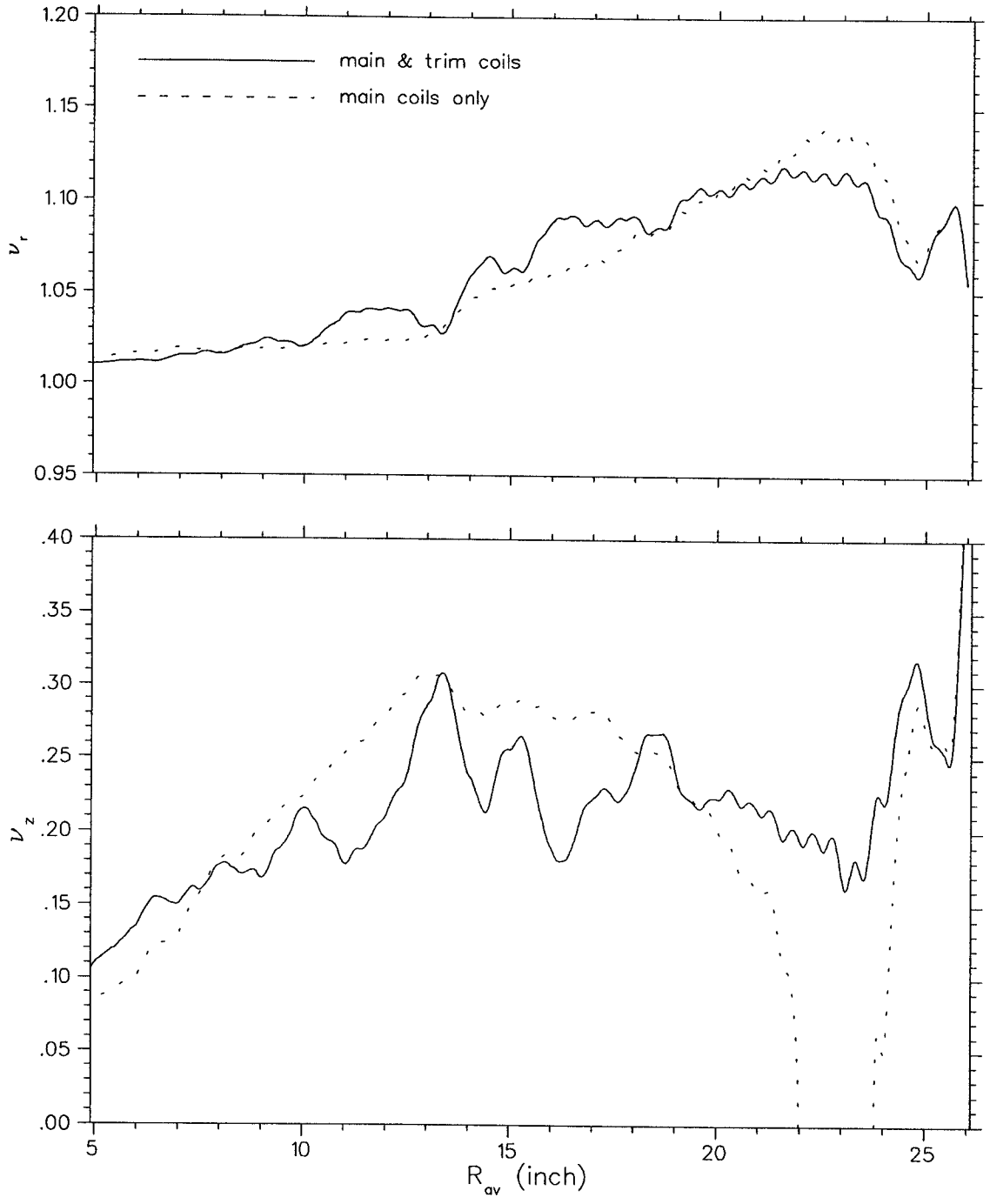

Figure 3.6: Plots of ν_r and ν_z as function of radius in the K250 synchrocyclotron perfect field. The solid curves are associated with trim coil on, the dotted curves with all trim coils off.

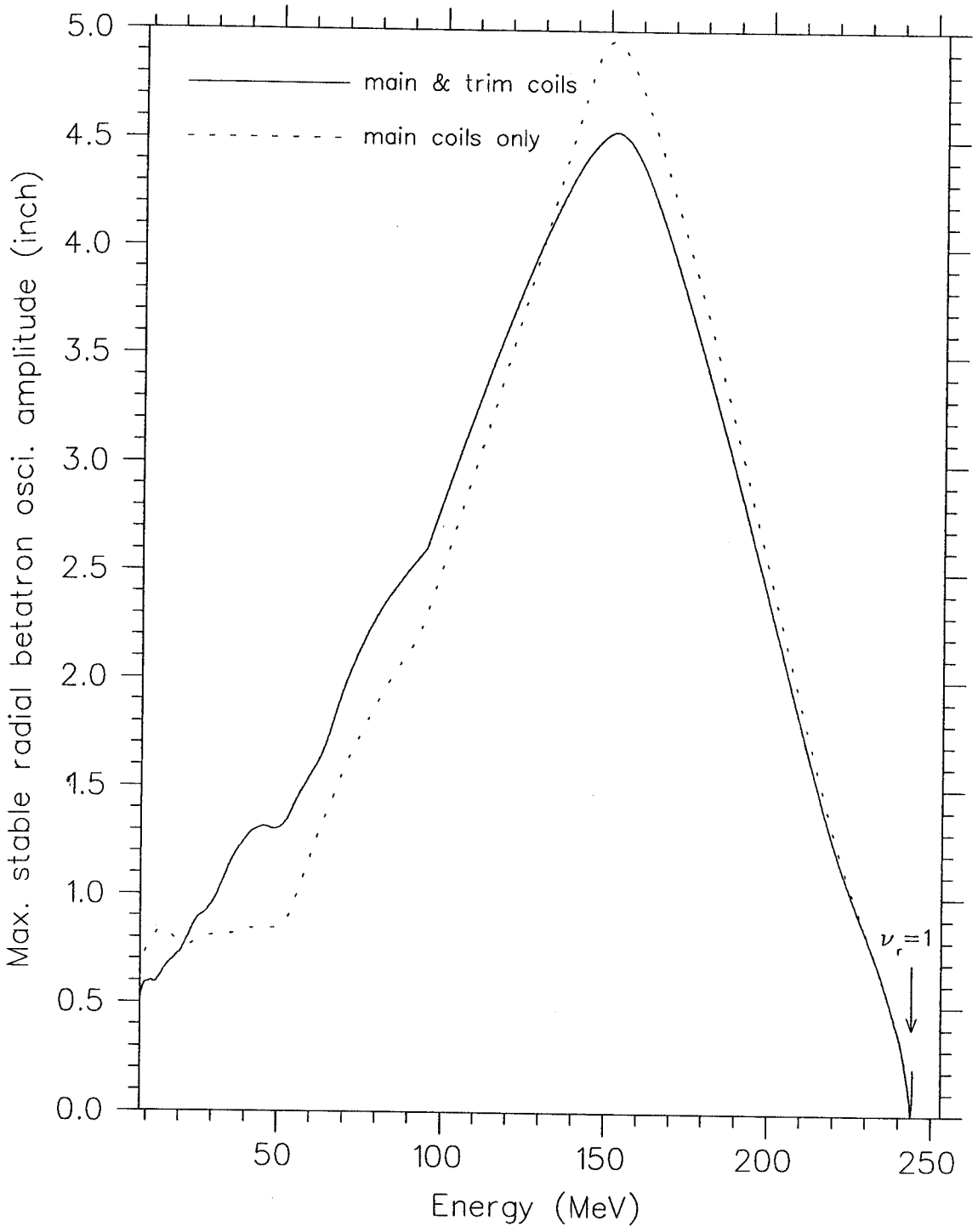

Figure 3.7: Plot of maximum stable radial betatron oscillation amplitude A_c (the radial distance in the phase space from the equilibrium orbit to the furtherest unstable fixed point) calculated by using the EO code, as function of energy in the K250 synchrocyclotron perfect field. The solid curve is associated with trim coils on, the dotted curve with all trim coils off. Recall that $A_c \propto \mid \nu_r - 1 \mid$.

magnet can bend into a closed orbit.

The closed orbits acquire orbit shape which encloses high magnetic field region. There are thus four pairs of closed orbits in a 3 sector machine, associated to the center (r = 0) of the field and the three hills. However, the stable orbit associated with the center of the field is the only orbit (of the total eight) suitable for particle acceleration due to its linearity.

The static (also called coasting or non-accelerated) phase space orbits, along with seven fixed points at E = 243 MeV, are plotted in Figure 3.9. It shows a typical static phase plot at an energy somewhat smaller than the $\nu_r = 1$ resonance energy. Recall that $x = A_r cos(\nu_r \theta)$, where A_r is the amplitude of betatron oscillation. The direction of flow can therefore be determined by the value of radial focusing frequency. If $\nu_r > 1$ the flow is counterclockwise; $\nu_r < 1$ is clockwise flow. Besides, flow lines never cross and have to satisfy the continuity requirement. One important feature of the radial phase space is the size of the stable region. The maximum stable radial amplitude could be gleaned from the radial phase space plot and an approximate measure of this size is given by the distance in the phase space from the equilibrium orbit to the nearest unstable fixed point, as is clearly exemplified in this graph.

The static phase plot associated with the outer unstable fixed point at E = 243 MeV in the K250 120^0 field is shown in Figure 3.10. The separatrices at an energy of 243 MeV are indicated by the crossed solid lines obtained by tracking the static orbits starting at points very close to this outer unstable fixed point.

Radial phase space plots at $\theta = 0$ showing the positions of fixed points at various energies in the K250 120^0 field are given in Figure 3.11 and Figure 3.12.

Figure 3.11 shows that the stable area shrinks to zero at an energy of 243.8 MeV at which $\nu_r = 1$. Note that the resonance $\nu_r = 1$ is characterized by a point in energy

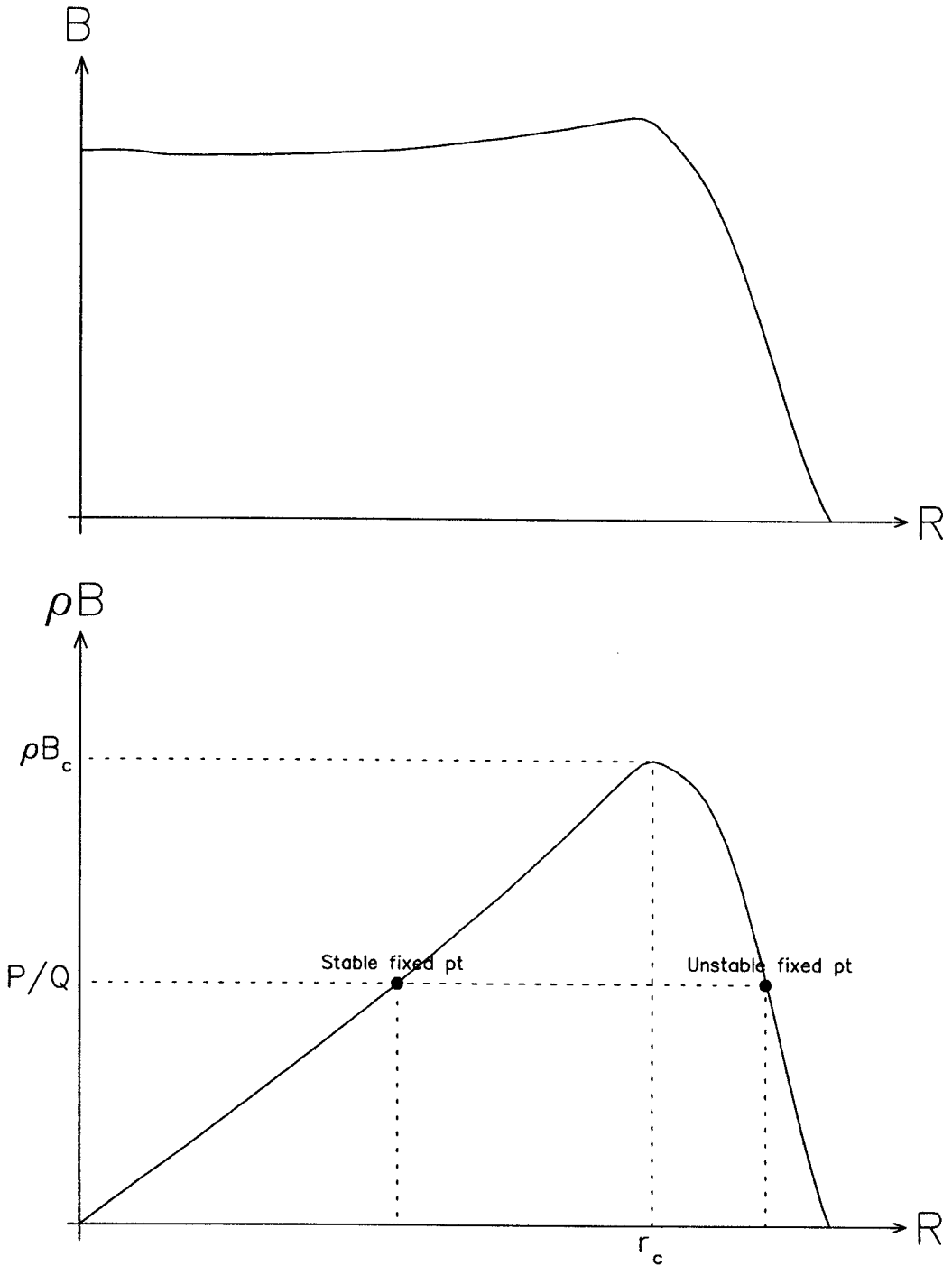

Figure 3.8: The profile of a average B field in the K250 synchrocyclotron and the associated plot of ρB and p/q vs. r.

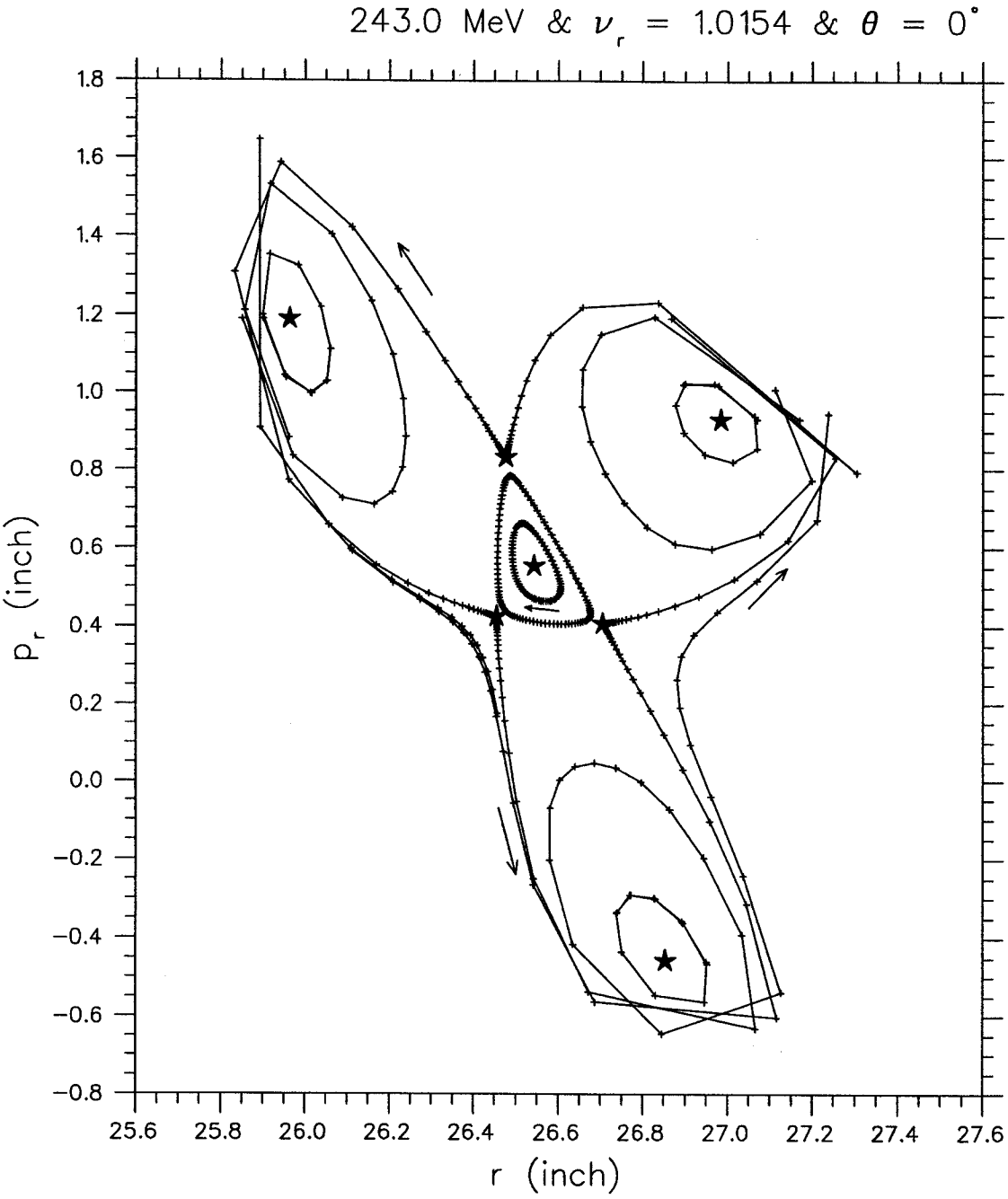

Figure 3.9: Static phase space plot, accompanied with seven fixed points at E = 243 MeV and $\theta = 0°$ in the K250 120^0 field. The lines connect positions on successive revolutions of orbits evolving from some given starting conditions. Note momentum is expressed in length unit (cyclotron unit) by dividing $m_o\omega_o$, where m_o is the rest mass of protons and $B_o = 3.316$ tesla assuming in the unit conversion.

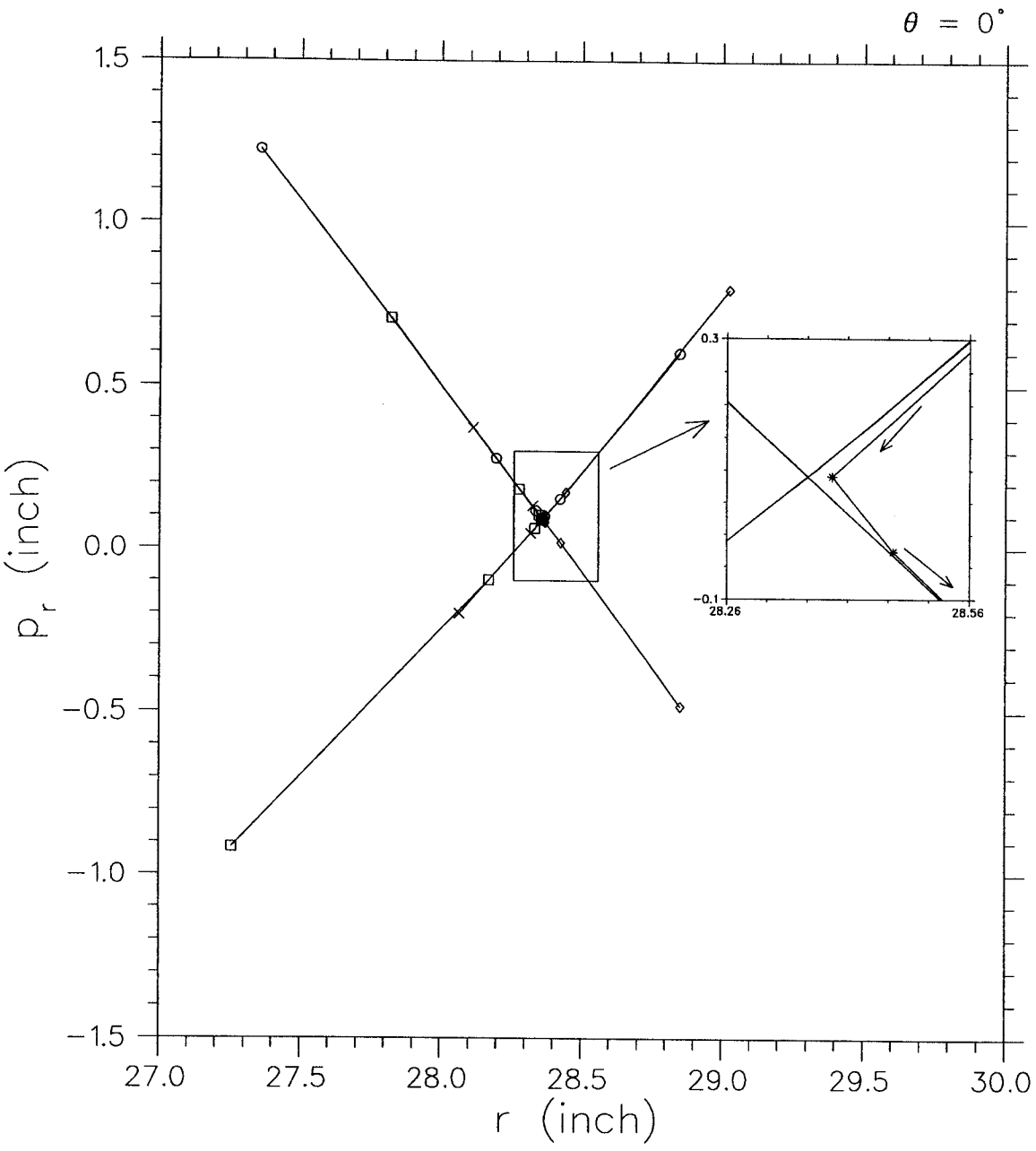

Figure 3.10: Phase plot shows the outer unstable fixed point and its associated separatrices at E = 243 MeV in the K250 120^0 field. The separatrices are computed by tracking coasting (static or non-accelerated) orbits backward and forward starting at points very close to the outer unstable fixed point and plotted once per turn (0^o). The separatrices and a coasting orbit which starts at a point 30 mil away from the fixed point are shown in the right small panel using magnified scale.

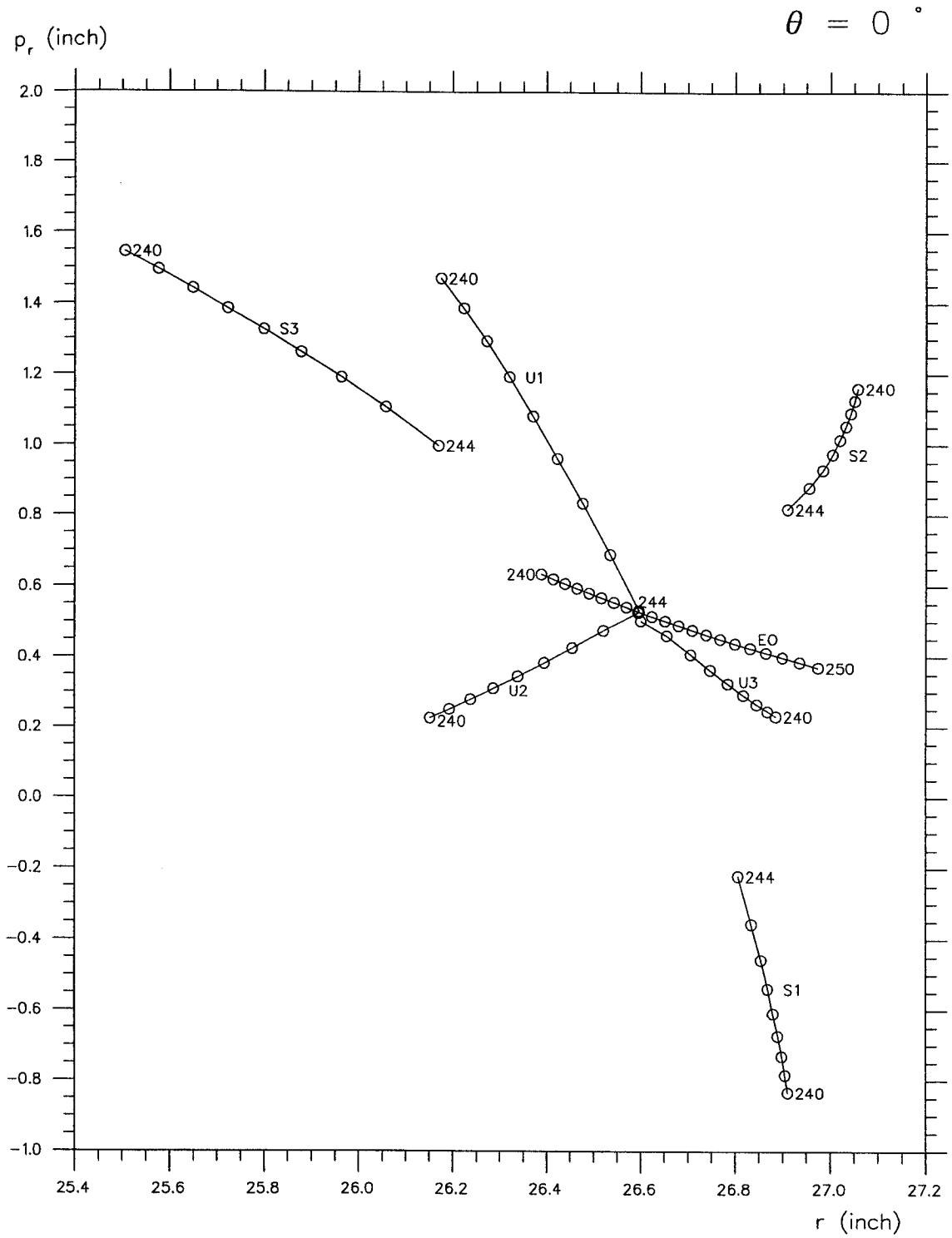

Figure 3.11: A radial phase space plot showing the locations of fixed points at various energies in a magnetic field with perfect 3 sector symmetry; the numerical labeling beside the points gives the energy in MeV; the scales are in cyclotron units. Unlabeled points are at energies equally spaced, 0.5 MeV, between labeled points. The label U indicates a hill-type unstable fixed point, S a hill-type stable fixed point and E.O. the fixed point associated with the center of the magnetic field. Number 1, 2 and 3 indicate the stable and unstable pair with the same hill.

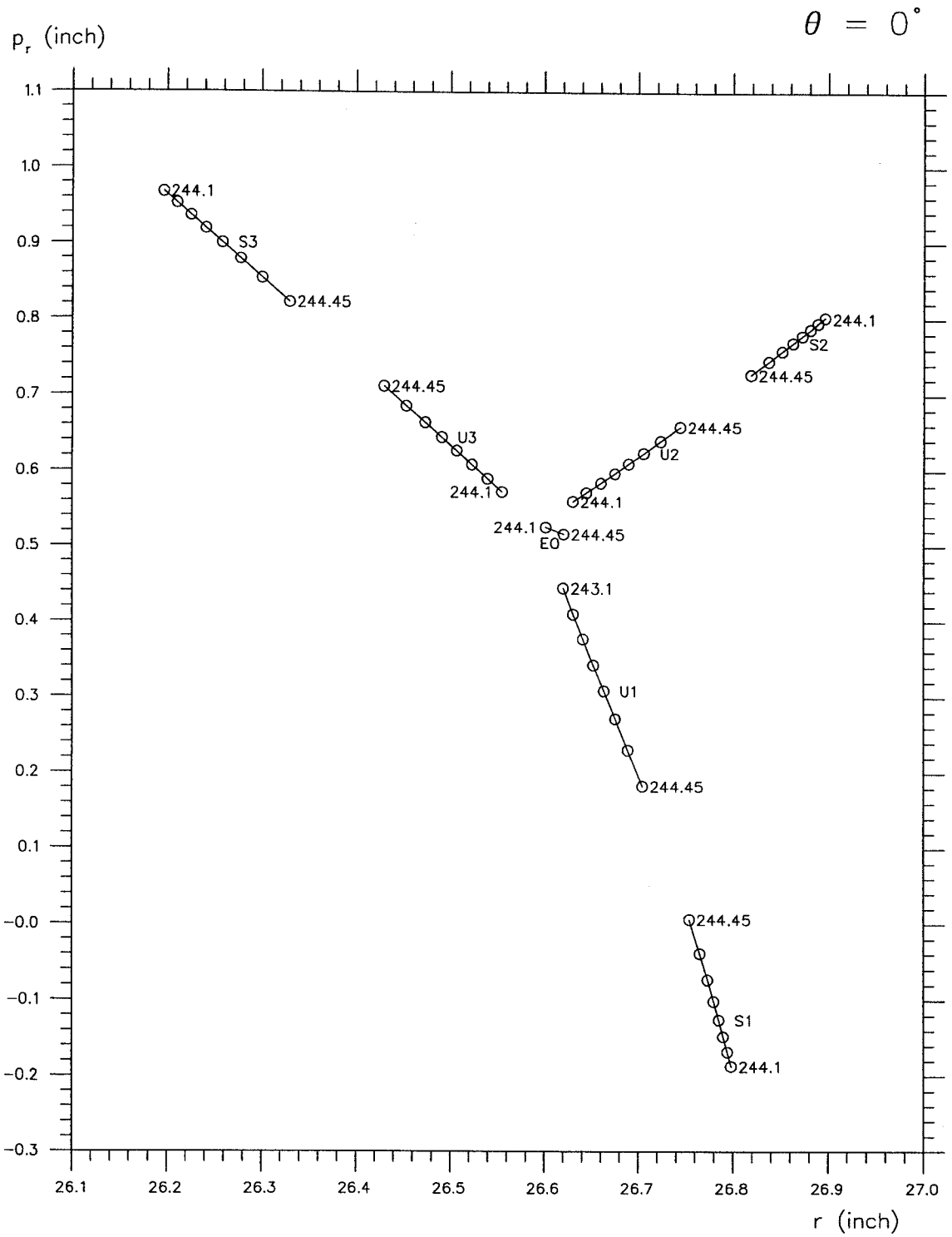

Figure 3.12: Plot of fixed points in the vicinity of $\nu_r = 1$ shows that a rapid renewing for the stability area. In addition, it shows the annihilation of the three pairs of hill-type fixed points at an energy about 244.5 MeV.

(no stop band) in such a perfect three sector field. Of special interest is the rapidly reappearing central stable region right after $\nu_r = 1$ (Figure 3.12). From this graph, we see that the hill type fixed points are annihilated in pairs at an energy of about 244.5 MeV. Beyond this energy, only two fixed points exist (E.O. and outer unstable) both associated with the machine center. This rapid renewing and shrinkage of the stable region at energies just above and below the resonance $\nu_r = 1$, caused by the sharpness of the edge field, implies that in the absence of field imperfections or with sufficiently small imperfections at the $\nu_r = 1$ radius, the beam could be recaptured by the stable region and remain compact. We thus expect that the well-centered particles might traverse this resonance without getting lost.

Figure 3.13 and Figure 3.14 show the behaviour of a beam-like phase space area as it is accelerated through the resonance $\nu_r = 1$. The maximum useable beam area roughly increases two times in radial phase area as the energy gain per turn rises from 10 keV/turn to 20 keV/turn. The "triangle" distortion induced by the $\nu_r = 1$ resonance traversal is illustrated as following. As the radial space area shrinks to zero, the off-centered phase space orbits are to move around one of the outside stable fixed points. After being recaptured by the renewed central stable region, the orbits have already been pulled toward hill-type stable fixed points; therefore beam distortion is induced. Note also that the x, p_x behaviour depends strongly on the field imperfections, especially the first harmonic component, in the vicinity of $\nu_r = 1$ resonance, which will be discussed in Chapter 4.

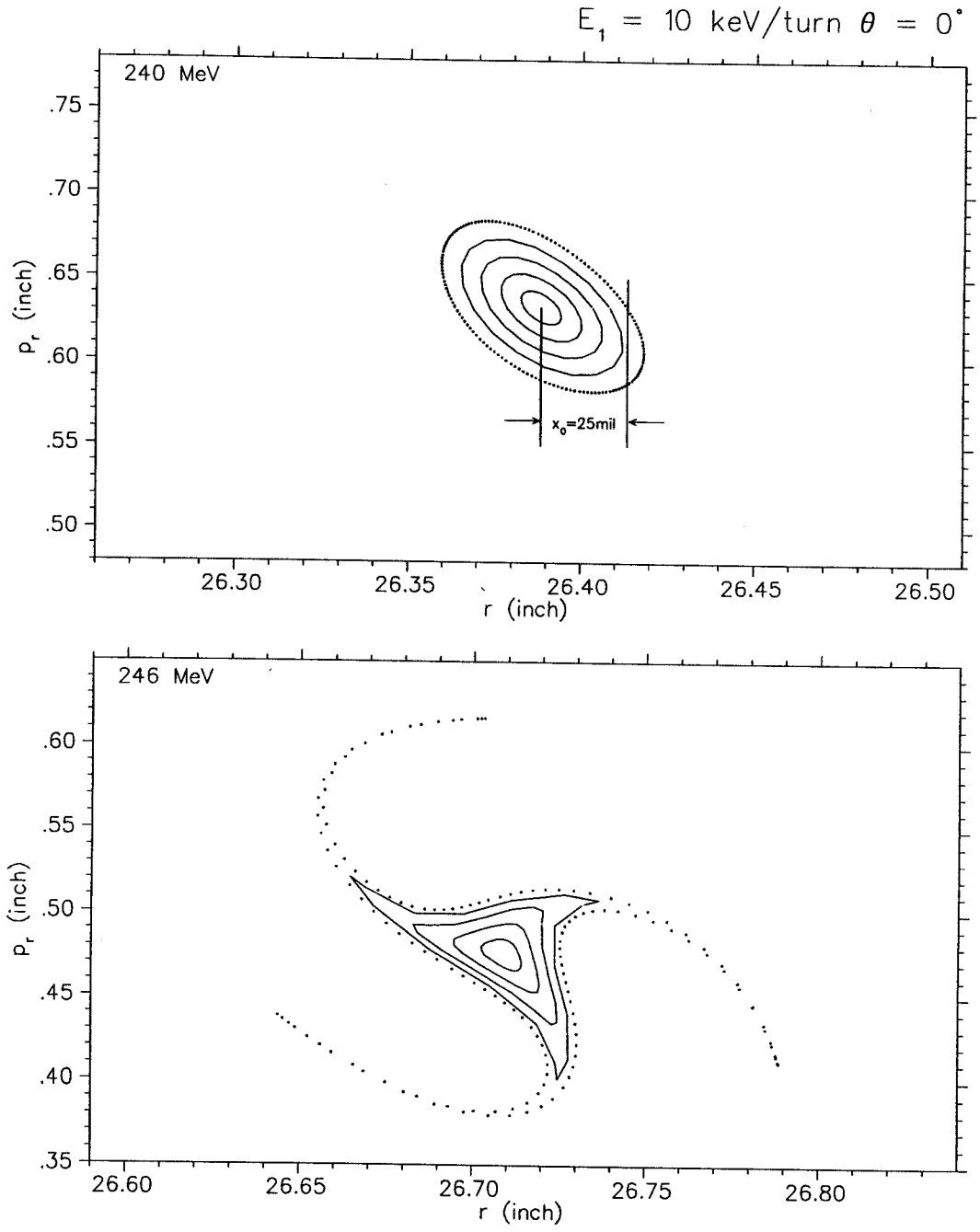

Figure 3.13: Radial phase plots at E=240 MeV and 246 MeV, $\theta = 0^o$, in the K250 120^0 field. Upper panel shows five coasting orbits associated with initial displacements in radius of 5, 10, 15, 20 and 25 mil relative to the equilibrium orbit. Lower panel shows the corresponding orbits at E=246 MeV, which start on the eigenellipses in the upper frame and are accelerated, assuming constant energy gain 10 keV per turn. The dotted curves indicate the estimated acceptance of radial space region inside which most of the orbits can be recaptured by the renewed central stable region after passing $\nu_r = 1$.

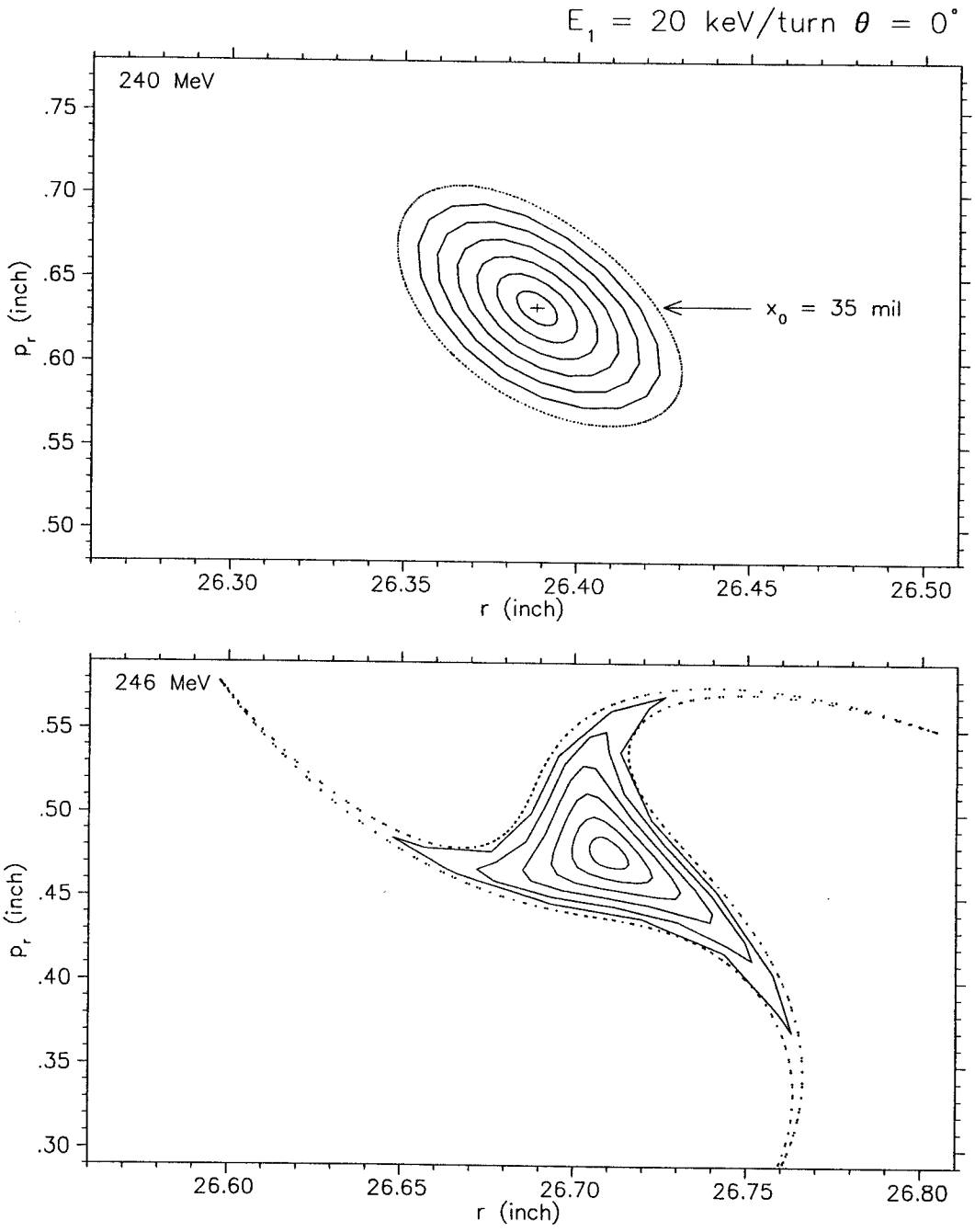

Figure 3.14: Radial phase plots at E=240 MeV and 246 MeV, $\theta = 0^o$, showing the acceptance of the $\nu_r = 1$ resonance in the K250 120^0 field with 20 keV/turn constant energy gain. It shows the transmission limit of the $\nu_r = 1$ resonance corresponds to roughly a 35 mil eigenellipse at E = 240 MeV.

Chapter 4

Resonance Limitations

In the process of beam extraction, the intrinsically low energy gain per turn for synchrocyclotrons poses very difficult problems at the transitions of the various resonances which occur in the extraction region. In this chapter, approximate analytic resonance formulas are presented for qualitative guidance. I am in debt to the authors who did the original work. Although the derivations are too simplified to give quantitative estimation for three sector spiral machines, they nevertheless provide insight into the effect of various field characteristics.

4.1 Resonances at the Extraction Region

Table 4.1 lists the average radius and energy at which important resonances occur in the extraction radius region, calculated by EO code with the DTP and the FD interpolation methods employed. The eleven-point finite difference method [56], denoted FD, which is supposed to do better interpolation computations, is used to check the double three point method, which is the standard scheme in NSCL orbit codes.

From Table 4.1, it is clear that the resonance pattern inferred from these two interpolation methods are identical, and the locations of the resonances are almost the same. Therefore, we expect that the interpolated errors associated with the DTP

Table 4.1: Average radius and energy of important focusing resonances in the extraction region of the K250 120^0 field.

	double-three-point		11pt finite difference	
resonances	R_{av}(inch)	energy(MeV)	R_{av}(inch)	energy(MeV)
$\nu_z = \frac{1}{2}$	26.03	241.2	25.95	239.7
$\nu_r = 2\,\nu_z$	26.06	241.6	25.99	240.3
$\nu_r = 1$	26.20	243.8	26.15	243.1
$\nu_z = 1$	26.70	250.3	26.69	250.2
$\nu_r + 2\,\nu_z = 3$	26.89	251.8		

method should not damage the credibility of results of the extraction calculations.

4.2 Half Integer Resonance $\nu_z = \frac{1}{2}$

Following the analysis of Baartman and Gordon [57] [58], at the half integer resonance, $\nu_z = \frac{1}{2}$, stability is lost if there is a first radial derivative of the first harmonic of the magnetic field. Assume that the deviation of the equilibrium orbit from a circle is relatively small (i.e. a machine with a large number of sectors or one where the flutter field is a small fraction of the average field). Then we can write down the differential equation to describe the vertical motion,

$$\frac{d^2z}{d\theta^2} + \nu_z^2 z = bzcos\theta \tag{4.1}$$

where $b = \frac{<R>}{<B>}\frac{dB_1}{dR}$.

Using the Born approximation, one can obtain a solution by treating the driving field, b, as a perturbation. It can be shown that this driving force changes ν_z to ν_z^* given by [58]

$$(\nu_z^* - \frac{1}{2})^2 = (\nu_z - \frac{1}{2})^2 - (\frac{b}{2})^2 \tag{4.2}$$

At $\nu_z = 1/2$, ν_z^* has an imaginary part $Im(\nu_z^*) = b/2$. Since $z \sim e^{i\nu_z\theta}$, this implies an exponentially growing betatron amplitude. Also, ν_z^* has an imaginary part over a

range $\Delta\nu_z = b$ around $\nu_z = 1/2$. If the incoherent oscillations within the beam prior to the resonance are characterized by a maximum amplitude A, then after acceleration through the resonance, this amplitude will be increased by ΔA given approximately by

$$\Delta A = A[\frac{\pi b}{2}]^2 [\frac{E_1}{d\nu_z/dE}]^{-1} \tag{4.3}$$

where E_1 is the energy gain per turn. This predicts that the amplitude gain will vary as the square of the driving term due to the fact that both the strength of the resonance and the number of turns spent in the stop band are proportional to this term.

4.3 Integer Resonances $\nu_r = 1$ and $\nu_z = 1$

As particles accelerate through the $\nu_r = 1$ resonance, the oscillation amplitude grows at the rate of $\pi\varepsilon_o R$ per revolution [45], where R is the radius of the orbit. The parameter ε_o in this expression is the ratio of the strength of the first harmonic bump to the strength of the average field. This result can be derived approximately by solving the following differential equation, valid under the assumption of small deviation of the equilibrium orbit from a circle.

$$\frac{d^2x}{d\theta^2} + \nu_r^2 x = g\,cos\theta \tag{4.4}$$

where x, $x \ll R$, is the displacement from the equilibrium orbit and $g = \varepsilon_o R$. The particular solution x_p is

$$x_p = \frac{g}{\nu_r^2 - 1} \times (cos\theta - cos(\nu_r\theta)) \tag{4.5}$$

Using appropriate trigonometry, this solution reduces to

$$x_p \simeq \frac{g\theta}{2} sin\theta \tag{4.6}$$

for $\nu_r \simeq 1$. Therefore the oscillation amplitude growth rate is equal to $\pi\varepsilon_o R$ per turn.

One can also obtain the formula for the coherent amplitude A_{res}, the induced total amplitude growth after crossing the $\nu_r = 1$ resonance, by using the technique of action-angle variables. Define

$$x = \frac{A}{\sqrt{\nu_r}} cos\psi$$
$$\psi = \nu_r\theta + \phi \tag{4.7}$$

Substituting x and its derivatives into the equation of motion and assuming $\frac{\partial\nu_r}{\partial\theta} \ll 1$, we get after some rearrangement

$$\frac{\partial A}{\partial\theta} = -\frac{g}{\sqrt{\nu_r}\, cos\theta\, sin\psi}$$
$$\frac{\partial\psi}{\partial\theta} = \nu_r - \frac{g\, cos\theta\, cos\psi}{\sqrt{\nu_r}\, A} \tag{4.8}$$

To first order, these can be written as

$$\frac{\partial A}{\partial\theta} = -\frac{g}{\sqrt{\nu_r}} cos\theta\, sin(\int \nu_r d\theta) \tag{4.9}$$

and integrated to yield

$$\Delta R = \frac{g\,\pi}{\sqrt{\nu_t}} \tag{4.10}$$

Substituting the expression for g, the coherent radial oscillation amplitude produced is given approximately by [59] [1]

$$\Delta R = \pi\,\varepsilon_o\, R \cdot [d\nu_r/dn]^{-\frac{1}{2}} \tag{4.11}$$

where $(d\nu_r/dn)$ is the change in ν_r per turn; that is $(d\nu_r/dn) = E_1 \cdot (d\nu_r/dE)$. The term $[d\nu_r/dn]^{-\frac{1}{2}}$ can be regarded as the effective duration of the resonance n_{eff}.

[1] The original formula in this paper is expressed in the cyclotron units and it states that the resultant coherent oscillation of amplitude A caused by an nth harmonic field error B_n at $\nu_r = n$ resonance is $A = \frac{\pi}{\nu_t^{1/2}} \frac{\beta}{n\gamma} B_n$, where ν_t is the change in ν_r per turn.

Similar to the above derivation, one can easily show that after accelerating through the $\nu_z = 1$ resonance, the beam will have developed a coherent vertical oscillation whose amplitude is given approximately by [60]

$$\Delta Z = \pi \varepsilon_o R \cdot [E_1 \times |d\nu_z/dE|]^{-\frac{1}{2}} \tag{4.12}$$

4.4 Non-linear Coupling Resonances $\nu_r = 2\nu_z$ and $\nu_r + 2\nu_z = 3$

Among the essential nonlinear coupling resonances, those requiring the greatest attention in this three sector machine are the third order resonances : $\nu_r = 2\nu_z$, $\nu_r + 2\nu_z = 3$. (For example, the third order resonance $\nu_r = 2\nu_z$ stems from the driving term xz^2 in Hamiltonian). The higher order resonances are presumably negligible because the displacement from the E.O. is small in most of the accelerating process except the first and the last few turns. In general, if the beam is reasonably well-centered on the equilibrium orbit, then the acceleration through a nonlinear coupling resonance should proceed without significant damage, provided the resonance is traversed fairly rapidly [60]. However, this will not be a proper claim for synchrocyclotrons because the energy gain per turn is too small to pass the resonance quickly.

A nice mechanical analogue of the coupling resonance is a simple spring pendulum. If the resonance condition is satisfied ($\frac{W_{vertical}}{W_{horizontal}} = \frac{p}{q}$ p, q in integer and p+q the order of resonance), let the pendulum swing vertically and after a while it will oscillate horizontally.

The amplitude of the axial motion arising from a coupling resonance is approximately calculated as follows when the resonant condition is kept up long enough so that the radial oscillation dies down and the axial mode builds up. If the kinetic energy T of lateral motion is transferred completely from one mode to the other, so

$T_x = T_z$. one can easily show

$$\frac{A_x}{A_z} = \frac{\nu_z}{\nu_r} \tag{4.13}$$

where A_x, A_z are oscillation amplitudes of radial and vertical motion respectively. In the $\nu_r = 2\nu_z$ resonance, we see that any radial oscillation amplitude is multiplied by two when the energy is transferred to the axial mode. Therefore, partial or total vertical loss of ions is expected to occur if the beam is not well centered radially or the beam size is too big.

The coupling (Walkinshaw) resonance at $\nu_r = 2\nu_z$ is usually regarded as a formidable barrier for synchrocyclotrons. However, this resonance can be passed if the machine has good internal beam quality and if the field is suitably shaped (eg, Tokyo synchrocyclotron [61]). Both the strength of the driving force at the resonance and the resonance width depend critically on the radial derivative of the average magnetic field and on the amplitude of oscillation.

A. A. Garren [62] gave the following results. If one keeps only the largest nonlinear terms and neglects the higher order derivatives of the average magnetic field than the second degree ($k \equiv u' \equiv \frac{r_0}{B}\frac{dB}{dr_0}$ and $u'' \equiv \frac{r_0^2}{B}\frac{d^2B}{dr_0^2}$). Then one can find that the equations for $x = (r - r_0)/r_0$, $y = z/r_0$ [2] are approximately

$$\frac{d^2x}{d\theta^2} + \nu_x^2 x = \frac{1}{2}u''(y^2 - x^2) \tag{4.14}$$

$$\frac{d^2y}{d\theta^2} + \nu_y^2 y = u''xy \tag{4.15}$$

Regarding the nonlinear terms in the above equations as perturbations, and assuming the amplitudes and phases of the x and y oscillations to be slowly varying parameters,

[2] The notation have been changed here, and now writes ν_x and ν_y in place of ν_r and ν_z in this section.

then:

$$x = A_x sin(\nu_x\theta + \psi_x)\,,\;\; p_x = \nu_x A_x cos(\nu_x\theta + \psi_x)\,, \tag{4.16}$$

and similarly for y. Thus the equations of motion for A_x, A_y, ψ_x, and ψ_y are obtained, retaining only terms of low frequency, $\sigma \equiv 2\nu_y - \nu_x$:

$$\frac{dA_x}{d\theta} = -\frac{u''}{8\nu_x} A_y^2 cos\chi \tag{4.17}$$

$$\frac{dA_y}{d\theta} = \frac{u''}{4\nu_y} A_x A_y cos\chi \tag{4.18}$$

$$\frac{d\psi_x}{d\theta} = -\frac{u''}{8\nu_x}\frac{A_y^2}{A_x} sin\chi \tag{4.19}$$

$$\frac{d\psi_y}{d\theta} = -\frac{u''}{4\nu_y} A_x sin\chi \tag{4.20}$$

where $\chi \equiv \sigma\theta + 2\psi_y - \psi_x$. This system may be shown by setting $\nu_x = 2\nu_y$ in the various coefficients to have two invariants, A and C, defined by

$$4A^2 = 4A_x^2 + A_y^2 \tag{4.21}$$

$$C = \frac{u''}{\nu_x} A_y^2 A_x sin\chi - \sigma A_y^2 \tag{4.22}$$

where the first invariant A is the result of energy conservation.

From Equation 4.22 one may see that A_y^2 will oscillate between limits A_{ymin}^2 and A_{ymax}^2, positive solutions of the quartic equation for A_y^2 obtained by setting $sin\chi = \pm 1$. The limits A_{ymin}^2 and A_{ymax}^2 are close together for $\mid \sigma \mid \gg \mid u''A/\nu_x \mid$, corresponding to little change of axial amplitude, but if $\mid \sigma \mid \ll \mid u''A/\nu_x \mid$ they may be quite apart, and most of the oscillation energy may go into the axial mode. Thus the $\sigma = \pm \mid$

$u''A/\nu_x$ | define the edges of the stop band, whose center is located at the radius where $\nu_x = 2\nu_y$.

As particles are accelerated, the parameters σ, u'', ν_x and ν_y change continuously. Since σ changes most rapidly, the full stop band width is given approximately by

$$n_{eff} = \mid \frac{u'' \cdot A}{E_1 \cdot d\sigma/dn} \mid \tag{4.23}$$

From Equation 4.18 one can estimate the value of maximum z-amplitude gain per turn as

$$\frac{dz}{dn} \mid_{max} \approx \frac{\pi u''}{r_0} \times x_0 \times z_0 \tag{4.24}$$

where x_o, z_o are the initial oscillation amplitudes before the particle crossing this resonance.

The effect of resonance $\nu_r + 2\nu_z = 3$ could be dealt with similarly.

Chapter 5

Longitudinal (Synchrotron) Motion and Its Implications

An unusual dee structure is suggested for the proposed K250 synchrocyclotron; dees in two adjacent valleys of the K500 cyclotron are galvanically coupled across the center to become a single electric dee and the third dee is removed; even-spaced accelerating gaps are then no longer present. The formulae in this chapter are derived mainly following the path given in Livingood's book [63].

The maximum energy gain per revolution $q \cdot V_{max}$ is equal to $q \cdot V_{dee}$ for this proposed RF system, where V_{dee} is the dee voltage. Therefore, the resulting relation between energy gain per turn E_1, phase angle ϕ and dee voltage V_{dee} is $E_1 = q \times V_{dee} \times \cos\phi$. The phase reference angle ϕ is the angular difference between the RF and the particle. The synchronous phase angle, the phase angle of the ideal synchronous ion whose frequency of revolution is the same as that of the accelerating voltage at every instant of time, $\phi_s = 48.2^o$ is decided such that the largest number of ions can clear the source and then pass successfully the resonances at the extraction region; the largest external current is thus obtained.

In following sections, the principle of phase stability is explained and the equations are derived giving the frequency of the synchrotron oscillation, and the characteristics

of the stable region (the so-called Fish diagram), from which the bucket area can then be obtained. Furthermore, the frequency modulation and acceleration time are worked out by using the EO code to compute the orbital frequency at each energy. Finally, the validity of a time saving constant energy gain approximation and of the initial conditions in the extraction calculations are investigated in the last part of this chapter.

5.1 Basic Concepts

Synchrocyclotrons look and operate very much like cyclotrons and are able to avoid the energy limitation of the classical Lawrence-type fixed-frequency cyclotron by varying the frequency of the oscillator to match the motion of the ideal synchronous particle. As acceleration proceeds and the rotation frequency drops because of the increase in mass of the accelerated particles, a tuning element steadily lowers the frequency of the RF oscillator so that the orbital frequency of an ideal synchronous particle matches the frequency of the RF voltage at every instant of time. Most of the ions (nonsynchronous particles) are accelerated by benefit of the principle of phase stability; they gain energy at the same average rate as does a synchronous ion but oscillating about this average. Using this type of system, the upper energy limit of the cyclotron can be raised to whatever limit the bending power of the magnet allows, since the mass increase of the accelerated particles no longer causes a phase shift relative to the RF. One price paid for the greater energy is that the output current is vastly reduced, since each group of ions must be accelerated to high energy and then the oscillator returned to the starting frequency before it can pick up another group.

The separation of the motions of betatron (traverse) and synchrotron (longitudinal) oscillations leads to a quite simple treatment and sheds light on intuitive expla-

nation of cyclotron orbit behavior. Therefore, we focus on the longitudinal motion by analyzing the phase equation in this chapter.

The median plane view of the proposed RF of the K250 synchrocyclotron is given in Figure 5.1. It shows the coupled dee configuration in the central region and four accelerating gaps, 60^o apart.

The sinusoidally alternating voltage in synchrocyclotrons can be expressed as

$$V(t) = V_{dee} \times cos[\int_o^t \omega_{rf}(t)dt] \tag{5.1}$$

where $\int_o^t \omega_{rf}(t)dt$ is the RF angle $\theta_{rf}(t)$.

Let the RF angles when an ion crosses the accelerating gap i $(i = 1, 2, 3, 4)$ be θ_{rfi}, respectively. The energy gain per turn in conjunction with first harmonic mode operation (h = 1) is thus given by

$$E_1 = qV_{dee} \cdot [cos\theta_{rf1} - cos\theta_{rf2} + cos\theta_{rf3} - cos\theta_{rf4}]$$
$$= qV_{dee} \cdot [cos(\theta_{rf1}) - cos(\theta_{rf1} + \pi/3) + cos(\theta_{rf1} + 2\pi/3) - cos(\theta_{rf1} + \pi)]$$
$$= qV_{dee}cos\theta_{rf1} \tag{5.2}$$

Therefore, qV_{max}, the maximum energy gain per turn, is equal to qV_{dee}. Define

$$\phi \equiv \theta_{rf} - \theta_{particle} \tag{5.3}$$

With the particular spacing, gaps 2, 3 and 4, just cancel at every ϕ and so we fix the particle reference angle at the first accelerating gap, and finally obtain the expression

$$E_1 = q \times V_{dee} \times cos\phi \tag{5.4}$$

Since an increase of energy causes an increase in the period of revolution, the synchronous phase angle ϕ_s must be chosen to lie between 0^o and 90^o for the reason of the phase stability, as will be explained in the following section.

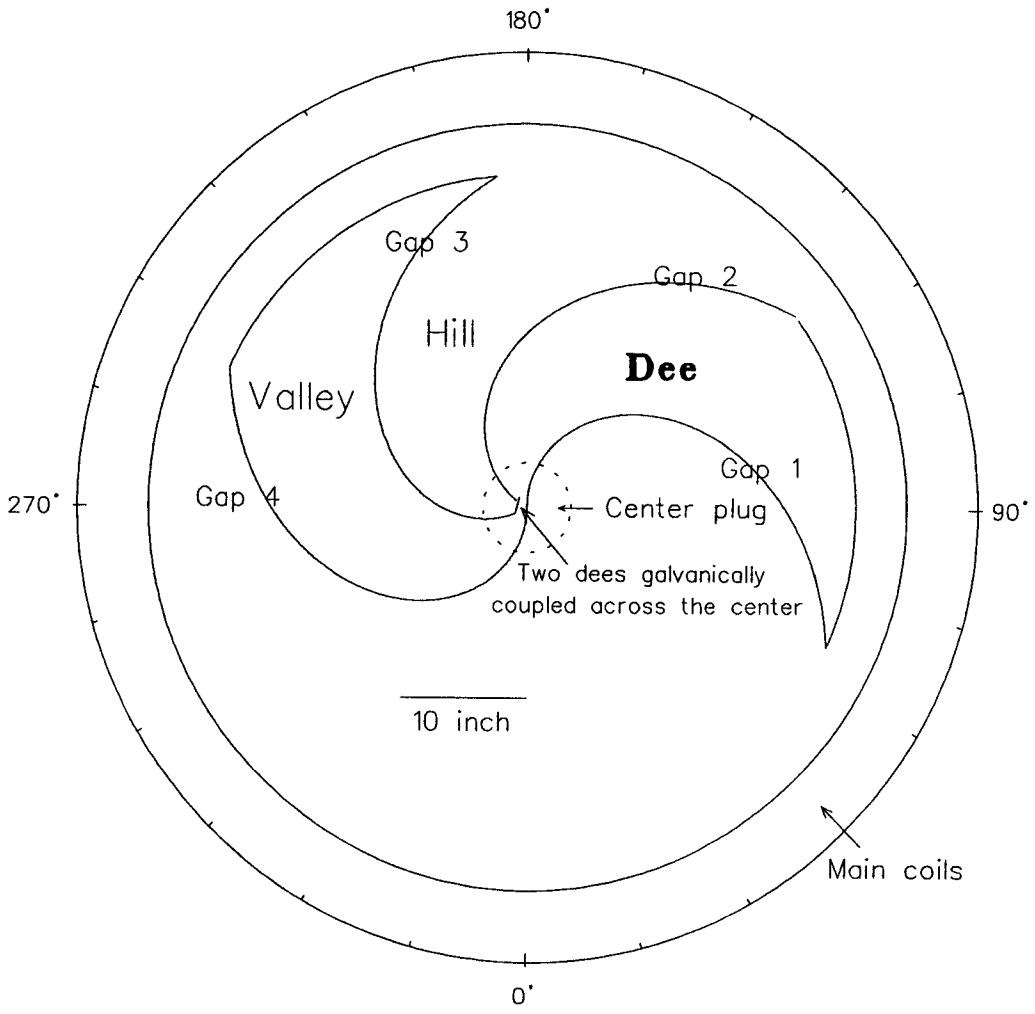

Figure 5.1: Median plane view of the proposed RF in the K250 synchrocyclotron. The four gaps are 60° apart azimuthally. It also shows the coupled dee configuration in the central region.

5.2 Principle of Phase Stability

The way in which phase stability acts in the K250 synchrocyclotron is illustrated in Figure 5.2. Consider a particle which has energy E_s but with phase ϕ_a ($-\phi_s < \phi_a < \phi_s$), as shown in Figure 5.2. It experiences an energy gain $\Delta E > \Delta E_s$ and hence immediately becomes nonsynchronous, for now $E > E_s$. This makes its period exceed the period τ_{rf} of the oscillator; so its phase one turn later is at ϕ_b, which is closer to ϕ_s. The energy is then raised again, though by a lesser amount, and the phase shifts further in the same direction. This process continues on subsequent turns until the particle's phase exceeds ϕ_s, reaching a maximum energy surplus from the synchronous value. The particle then comes to experiences an energy gain $\Delta E < \Delta E_s$, and the accumulations of energy difference start to fall. At ϕ', E becomes equal to E_s, and the ion is again synchronous. ϕ' is however not ϕ_s and so immediately on the next turn, the particle finds itself with an energy deficit compared to the synchronous value. Its revolution period is less than τ_{rf} and one turn later it is at a phase slightly less than ϕ'. The energy gained is below the synchronous value or it may even be negative, so that a further shift to smaller phase angle takes places. This continues until the accumulated energy increments total up to the new values of E_s; this occurs just as ϕ_a is again reached. A complete phase oscillation has thus transpired and thereafter the process repeats.

If one repeats the arguments with ϕ_s located between $-\pi/2$ and 0, it can be found that phase oscillations do not occur for a synchronous phase angle in the fourth quadrant.

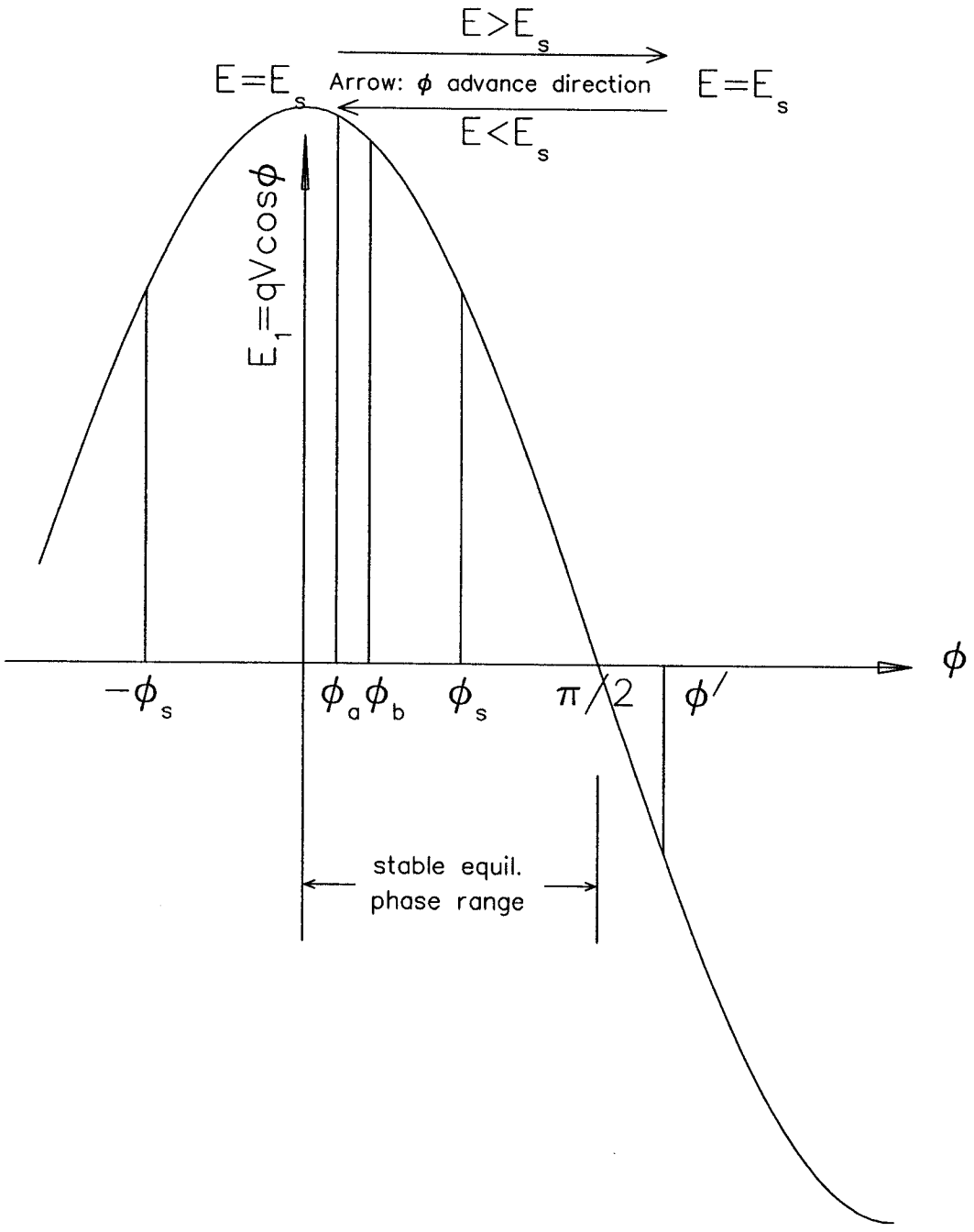

Figure 5.2: Possible excursions in phase of nonsynchronous ions. In order to save space, the successive values of the phase are plotted on a single wave.

5.3 The Phase Equation

The instantaneous difference in energy between a nonsynchronous and a synchronous particle is given by $\Delta E = E - E_s$; where the subscript s denotes the energy associated with a synchronous particle (i.e. a particle whose rotational frequency would just match the frequency of the accelerating voltage at that moment). By Equation 5.4, the change in the difference of their energies per unit angle is obtained dividing the change in the energy difference per turn by 2π.

$$\frac{d\Delta E}{d\theta} = \frac{qV_{dee}}{2\pi}[cos\phi - cos\phi_s] \tag{5.5}$$

If we are neglecting the small difference in the fields corresponding to synchronous and nonsynchronous particles, then we have

$$\frac{1}{d\theta} = \frac{1}{dt}\frac{dt}{d\theta} = \frac{1}{\omega}\frac{1}{dt} \cong \frac{1}{\omega_s}\frac{1}{dt} \tag{5.6}$$

The change in energy difference between a nonsynchronous and a synchronous particle is therefore given by

$$\frac{1}{\omega_s}\frac{d\Delta E}{dt} \cong \frac{qV_{dee}}{2\pi}[cos\phi - cos\phi_s] \tag{5.7}$$

In addition, the change in phase $d\phi$, in a time dt, can be written as (note $\omega_{rf} = \omega_s$)

$$\frac{d\phi}{dt} = \omega_s - \omega \tag{5.8}$$

Define

$$\frac{d\omega}{\omega_s} \equiv -\Gamma\frac{dE}{E_s} \tag{5.9}$$

Since Γ in general is a slow varying function of synchronous particle energy, combining Equations 5.8 and 5.9, then yielding

$$\frac{d\phi}{dt} = \omega_s - \omega \equiv -\Delta\omega \cong \omega_s\Gamma\frac{\Delta E}{E_s} \tag{5.10}$$

Consequently, ΔE can be expresses as

$$\Delta E \cong \frac{E_s}{\omega_s \Gamma} \frac{d\phi}{dt} \tag{5.11}$$

When this is substituted in Equation 5.7, the final result is

$$\frac{1}{\omega_s} \frac{d}{dt} \left(\frac{E_s}{\omega_s \Gamma} \frac{d\phi}{dt} \right) \cong \frac{qV_{dee}}{2\pi} [cos\phi - cos\phi_s] \tag{5.12}$$

This 2nd order differential equation expresses the time dependence of the phase ϕ of the nonsynchronous particle as a function of the phase, frequency, and energy of the synchronous particle and the magnetic field (through the factor Γ).

5.3.1 Frequency of Synchrotron Oscillation of Small Amplitude

Assume the excursion in phase is small, let $\xi \equiv \phi - \phi_s$, and ω_s and Γ change only slightly over short period of time. Then the phase equation becomes

$$\frac{d^2\xi}{dt^2} + \Omega^2 \xi = 0 \tag{5.13}$$

$$\Omega^2 = \frac{qV_{dee} \Gamma sin\phi_s}{2\pi E_s} \omega_s^2 \tag{5.14}$$

With $\phi_s = 48.2^o$, the ratio of period of synchrotron oscillation to that of betatron oscillation in the extraction region for the K250 synchrocyclotron is

$$\frac{\tau_{s.o.}}{\tau_{b.o.}} \simeq 860 \ \ (V_{dee} = 15kV) \tag{5.15}$$

$$\frac{\tau_{s.o.}}{\tau_{b.o.}} \simeq 610 \ \ (V_{dee} = 30kV) \tag{5.16}$$

5.4 The Phase Diagram

Since ω_s and Γ change only slightly over short intervals, by

$$\frac{d^2\phi}{dt^2} = \frac{d}{dt}\frac{d\phi}{dt} = \frac{d\phi}{dt}\frac{d}{d\phi}\frac{d\phi}{dt} \tag{5.17}$$

the phase equation (Equation 5.12) may be expressed as

$$\frac{d\phi}{dt}\frac{d}{d\phi}\frac{d\phi}{dt} - \frac{\Omega^2}{sin\phi_s}(cos\phi - cos\phi_s) = 0 \tag{5.18}$$

Multiply by $d\phi$ and integrate, then yield

$$(\frac{d\phi}{dt})^2 - \frac{2\Omega^2}{sin\phi_s}(sin\phi - \phi cos\phi_s) = C \tag{5.19}$$

where C is the integration constant and can be evaluated from the initial conditions. If ϕ_i is the initial phase and $\phi_i' \equiv (d\phi/dt)_i$ the initial phase velocity, we obtain

$$(\frac{d\phi}{dt})^2 = \frac{2\Omega^2}{sin\phi_s}(sin\phi - sin\phi_i - (\phi - \phi_i)cos\phi_s) + (\phi_i')^2 \tag{5.20}$$

Set initial condition $\phi_i = -\phi_s$, which represents an extreme displacement from ϕ_s (i.e., a minimum value of ϕ) if stable oscillations in phase are to occur. Consequently it follows that $(d\phi/dt)_i = 0$. Equation 5.20 then becomes

$$\frac{1}{\Omega}\frac{d\phi}{dt} = F(\phi, \phi_s) \tag{5.21}$$

where

$$F(\phi, \phi_s) \equiv \pm[\frac{2}{sin\phi_s}(sin\phi - \phi cos\phi_s + sin\phi_s - \phi_s cos\phi_s)]^{1/2} \tag{5.22}$$

Convert $d\phi/(\Omega dt)$ into expressions describing the difference in energy ΔE and the difference in the equivalent radii ΔR of the orbits of the synchronous and the non-synchronous ions. We have

$$\frac{1}{\Omega}\frac{d\phi}{dt} = \frac{\Delta E}{(\frac{E_s\Omega}{\omega_o\Gamma})} = \frac{\Delta R}{(\frac{R\Omega}{\alpha\beta^2\omega_o\Gamma})} = F(\phi, \phi_s) \tag{5.23}$$

where α is the momentum compaction and β is the relativistic parameter, v/c. The function $F(\phi, \phi_s)$ plotted as a function of ϕ for several values of ϕ_s is given in Figure 5.3. The bucket area inside the separatrices is the particle stable region. The intercepts with the F = 0 line represent the extreme amplitude of ϕ. The maximum excursions of synchrotron oscillation in energy and in radius occur at $\phi = \phi_s$. The function $F(\phi = \phi_s, \phi_s)$ plotted vs. ϕ_s is also given in Figure 5.3. One can draw the following general conclusions. With a large value of ϕ_s (near 90^o), the average energy gained per turn is small, wide oscillations in phase develop, the beam of ions exhibits a relatively great inhomogeneity of energy, and the current is big. On the other hand, with a small ϕ_s (near 0^o), there is a large average energy gain per turn, small oscillation in phase, little energy spread, and a relatively small current.

Given the choice of $\phi_s = 48.2^o$, the synchronous ion receives 2/3 maximum energy gain per turn and the nonsynchronous particles undergo the oscillations in phase, in energy, and in radius. The maximum permissible amplitude of synchrotron oscillation in energy and the corresponding radial displacement, associated with V_{dee}= 15 kV and $\phi_s = 48.2^o$, plotted versus the energy of the synchronous particle are shown in Figure 5.4, computed from Equations 5.9, 5.14 and 5.23, with the parameters Γ and dR/dE calculated by the EO code.

5.5 Acceleration Time and Frequency Modulation

The average energy gain per turn, $qV_{dee}cos\phi_s$, gives the following expression for the acceleration time

$$T = \int_0^{250MeV} \frac{dE}{\nu_s q V_{dee} cos\phi_s} \tag{5.24}$$

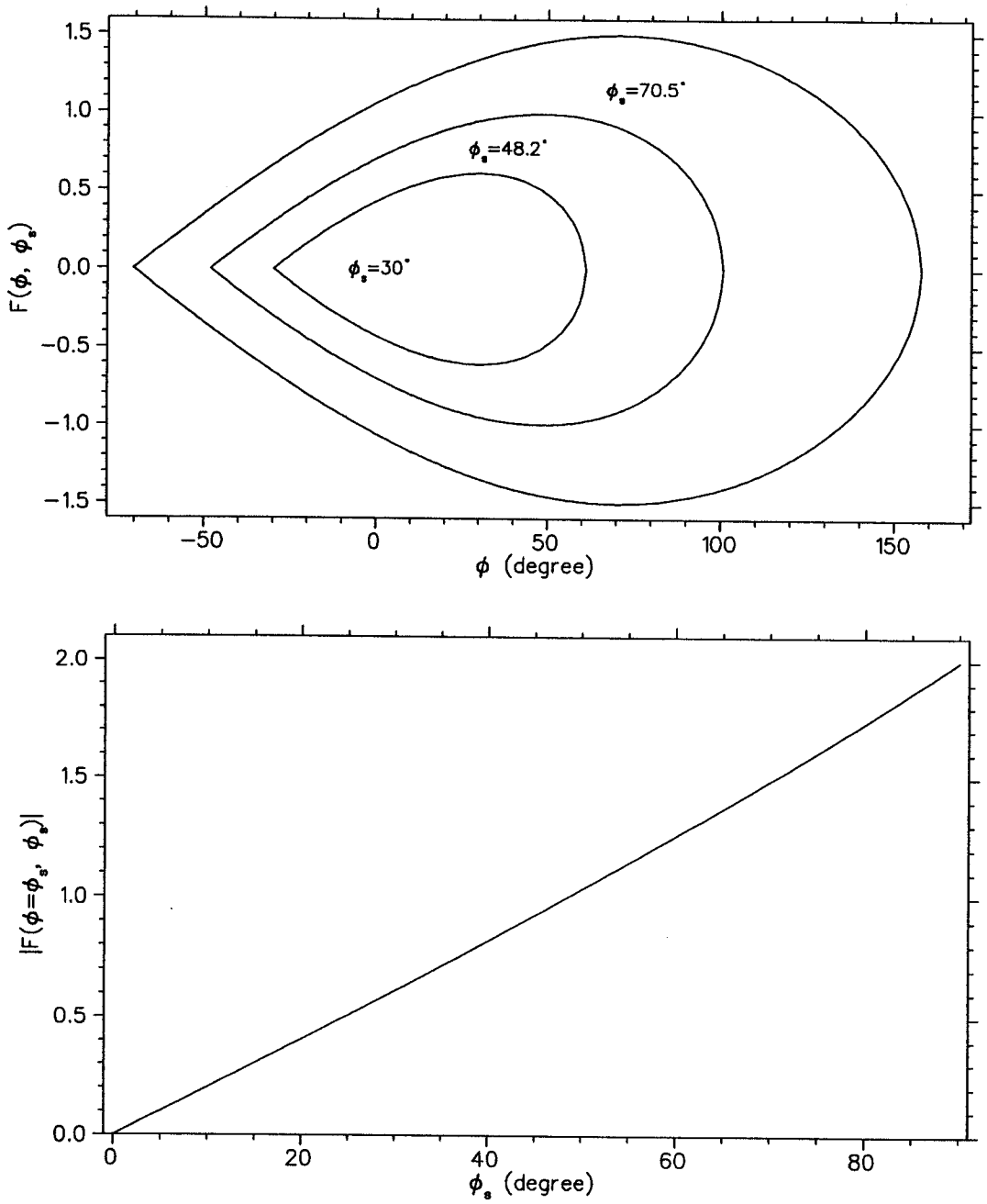

Figure 5.3: Top: the phase diagram for the case where $\phi_i = -\phi_s$. Numbers beside of curves give ϕ_s in degree. Bottom: Absolute values of $F(\phi = \phi_s, \phi_s)$ vs. ϕ_s gives the maximum excursion of synchrotron oscillation associated with the choice of synchronous phase ϕ_s.

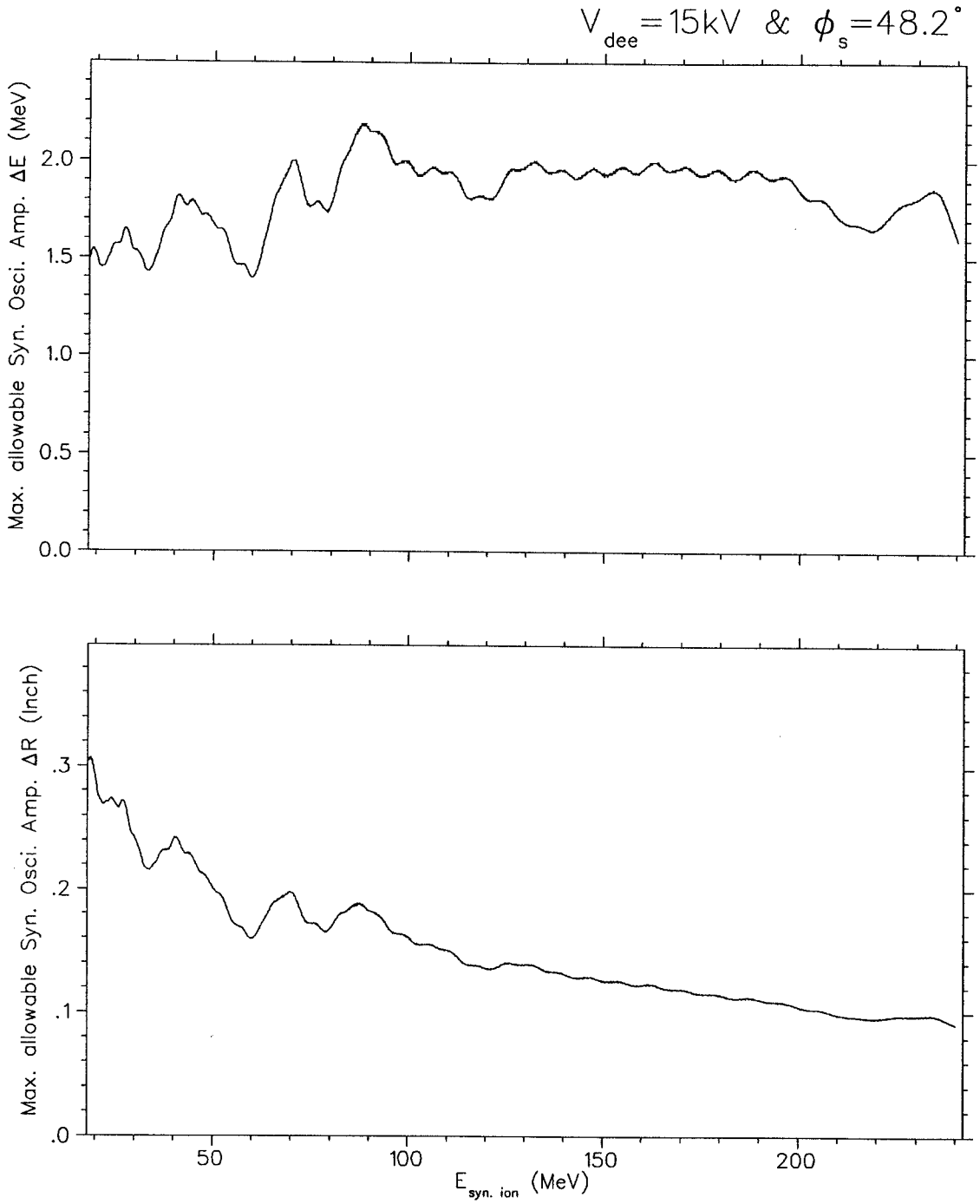

Figure 5.4: The maximum permissible amplitudes of synchrotron oscillation in energy and in radius are plotted with respect to energy of the synchronous particle. The calculations are done from Equations 5.9, 5.14, and 5.23.

Table 5.1: Parameters of the RF system

Dee voltage	15.00 kV	30.00 kV
Fixed energy gain	10.0 KeV/turn	20 KeV/turn
Acceleration time	0.53 ms	0.26 ms
Modulation frequency	$\leq$ 2kHz	$\leq$ 4 kHz
Initial frequency	50.55 MHz	50.55 MHz
Final frequency	43.22 MHz	43.22 MHz
Average time derivative	13.84 MHz/ms	27.68 MHz/ms

where $\nu_s = \omega_s/2\pi$ is the revolution frequency of the ideal synchronous ion. As a numerical example, for the case with fixed energy gain per turn 10 keV, the result is T = 0.53 ms. The proposed RF modulation frequency f_m is 1 kHz, corresponding to 1.0 ms period, which is thus feasible. For the synchronous particle, $\nu_{rf} = \nu_s$, we get

$$\frac{d\nu_{rf}}{dt} = \frac{d\nu_s}{dt} = \frac{d\nu_s}{dE}\frac{dE}{dN}\frac{dN}{dt} = \frac{d\nu_s}{dE} \times qV_{dee}cos\phi_s \times \nu_s \tag{5.25}$$

where ν_{rf} is the RF frequency and ν_s is the orbital frequency of the synchronous particle. From the above formula, the RF frequency as function of energy can be calculated by using the equilibrium orbit code. The resulting RF frequency time derivative $(-d\nu_{rf}/dt)$ is plotted in Figure 5.5. The wiggles in this graph are due to both spatial ripple in the field of the trim coils and to the DTP field interpolation scheme.

Finally, the required RF parameters for the K250 synchrocyclotron are listed in Table 5.1.

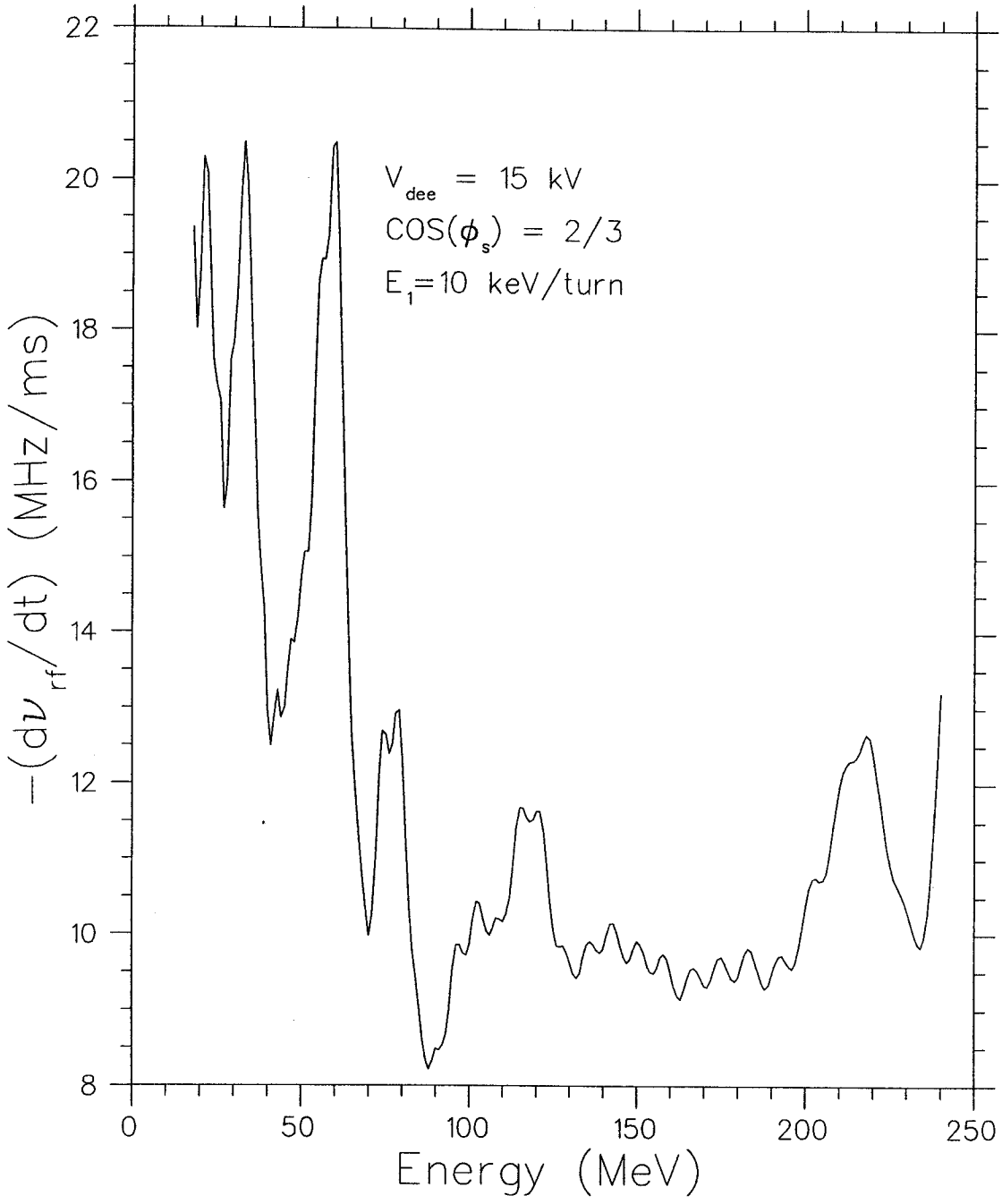

Figure 5.5: Plots of the RF frequency time derivative vs. energy with constant equilibrium phase $\phi_s = 48.2^o$ assumed throughout the acceleration.

5.6 Internal Current and Starting Betatron Motions in the Extraction Calculations

The average internal beam current I_{in}, in a synchrocyclotron is proportional to the peak current, I_{peak}, the capture efficiency, ε_c, and the beam bunch angular length, $\Delta\phi$ [55].

$$I_{in} = I_{peak} \cdot \varepsilon_c \cdot \frac{\Delta\phi}{2\pi} \tag{5.26}$$

$$I_{peak} = \epsilon_o \cdot \nu_o \cdot 2h \cdot E_1 \cdot \nu_{zmin}^2 \tag{5.27}$$

where E_1 is the energy gain per turn (proportional to the dee voltage), $2h$ the maximum beam height, ν_o the orbital frequency in the centre and ν_{zmin} the minimum values of the focusing frequency (Equation 5.27 is taken from Equation 2.18 with $\frac{\Delta\phi}{2\pi} = 1$ since this term is separately accounted for in Equation 5.26).

A simple theory of ion capture has been given by Bohm [64] and is reproduced here for reference convenience. Recall the initial conditions, $\phi_i = -\phi_s$ and $\phi_i' = 0$, lead to the maximum stable excursion from equilibrium phase ϕ_s and thus lead to the maximum phase velocity, ϕ_{imax}'. From Equations 5.20 and 5.14, we then obtain

$$(\phi_{imax}')^2 = \frac{2qV_{dee}\Gamma}{\pi E_s} \cdot \omega_s^2 \cdot (sin\phi_s - \phi_s cos\phi_s) \tag{5.28}$$

According to Equation 5.8, the phase velocity $\phi' = \omega_s - \omega$ measures the discrepancy between the angular frequency of the ion and that of synchronous particle. Because the catching process is determined only by the motion near the origin and all the ions have the same angular orbital frequency ω_o at the centre, Equation 5.28 tells how much the radio frequency may differ from ω_o for a particle still to be caught into phase stable oscillations. In other words, any particle starts from the ion source when

the RF frequency is such that

$$(\omega_{rf} - \omega_o)^2 \leq (\phi'_{imax})^2 \tag{5.29}$$

will perform stable phase oscillations and will be accelerated to final energy. Substituting Equation 5.28 in Equation 5.29, therefore, we obtain the total range of frequencies, $\Delta\omega_{rf}$, in which capture into phase-stable motion is possible

$$\Delta\omega_{rf} = 2\phi'_{imax} = 2\omega_o \times [\frac{2qV_{dee}\Gamma_o}{\pi m_o c^2}(sin\phi_s - \phi_s cos\phi_s)]^{\frac{1}{2}} \tag{5.30}$$

Since the rate of decrease of RF frequency is approximately constant, the range of time, Δt in which ions can starts in orbits which are phase stable, is

$$\Delta t = \frac{\Delta\omega_{rf}}{-d\omega_{rf}/dt} \tag{5.31}$$

Finally, the expression for the capture efficiency ε_c is obtained

$$\varepsilon_c \equiv \frac{\Delta t}{T_m} = \frac{-2\omega_o}{T_m(d\omega_{rf}/dt)} \times [\frac{2qV_{dee}\Gamma_o}{\pi m_o c^2}(sin\phi_s - \phi_s cos\phi_s)]^{\frac{1}{2}} \tag{5.32}$$

The beam's angular bunch length is determined by the choice of synchronous phase ϕ_s, by the dee voltage, and by the actual geometry of the central region. For smaller equilibrium phase angle, the angular bunch length decreases as a result of the smaller range of phase stability. On the other hand, particles with larger initial phase angles may not clear the source due to the negligible energy gain in the centre of the synchrocyclotron.

The capture efficiency, bunch angular length, internal current and beam quality therefore can not be accurately computed without knowing all the relevant parameters.

The internal beam intensity is thereby estimated approximately as follows: Based on ion source experiments by M. Mallory [65]: $I_{peak} = 12.74$mA with $V_{dee} = 30$ kV

and 1.57×9.525 mm^2 ion source slit gives 404 mm-mrad radial emittance and 390 mm-mrad axial emittance. We estimate that $I_{peak} = 270$ uA is achievable using a 0.33×0.95mm^2 source slit with dee voltage 15 kV, by assuming constant current density from the source. Because the beam is so tiny (inferred from the size of the source slit), it is expected to always stay in the linear area of the stable region until extraction occurs. Therefore, from Liouville's theorem, the beam should coincide with the invariant eigenellipse throughout the acceleration process before extraction. This in turn implies a beam with radial betatron oscillation amplitude of 30 mil and a vertical betatron amplitude 20 mil at E = 240 MeV.

From Table 1 in Ref. [55], it is clear that $e_c = 0.2\%$, $\Delta\phi = 20^0$ should be easily achieved in the K250 synchrocyclotron central region. Then the internal current turns out to be 30 nA from Equation 5.26. This value means that an extraction efficiency of approximately 30% will suffice to meet the intensity goal for a proton therapy system, namely a time average current of approximately 10 nanoamps.

5.7 Validity of Constant Energy Gain Approximation

It is important to recall that particles gain energy at the same average rate as does an ideal synchronous ion but oscillating from this average in synchrocyclotrons. Constant energy gain assumed in the calculations may therefore be a fair approximation. The accuracy of constant energy gain approximation is checked by using the $\nu_r = 1$ excitation extraction field, which will be presented in Chapter 6. The comparison of SYNZ^4 [1] runs to constant-energy-gain runs by using the Z^4 code are given in Table 5.2, Figure 5.6 and Figure 5.7. The energy histogram in 0.01 MeV steps, r vs. p_r, and z vs. p_z in cyclotron units at $\theta = 336^o$ are plotted in Figure 5.6, for those

[1] A modified version of the NSCL Z^4 orbit code to do synchrotron motion exactly.

particles which successfully enter the extraction channel. Figure 5.7 compares the distribution of final energies in 0.01 MeV steps, r vs. p_r, and z vs. p_z in cyclotron units at $\theta = 308^o$ (the last angle before the particles cross the 40″ edge of the stored magnetic field).

For particles which gain more energy than the average rate, the chance of surviving the resonance crossing is increased, and extraction is at higher energy. The particle with less than average energy rate gain does the opposite. As a result of these two factors, the distribution of final energies becomes flatter and broader; the extraction efficiency is therefore slightly reduced (about 2% in this case).

In conclusion, the constant energy gain approximation yields a good agreement with SYNZ[4] runs which include RF modulation in the calculations and deal with synchrotron motion realistically. Moreover, the computer time in constant-energy-gain calculations is substantially reduced relative to those of SYNZ[4] runs. The constant energy gain approximation will therefore be employed in Chapters 6, 7 and 8 which compare three candidate extraction systems.

Table 5.2: Extraction calculation results of the two versions of the Z^4 code.

	Exact synchrotron motion			Const E_1 approx.
Initial conditions (Synchronous ion: $E_{is} = 240$MeV, $\phi_s = 48.2^o$)				
E_i (MeV)	239.6	240.0	240.4	240.0
ΔE_i (MeV)	-0.4	0.0	0.4	0.0
$\Delta\phi_i$ (rf degree)	-20, -10, 0, 10, 20			x
A_r (mil)	30			30
A_z (mil)	20			20
No of rays	8250	8625	9000	1725
Code	$SYNZ^4$			Z^4
E_1 (keV/turn)	10 (average)			10 for all particles
Results of pre-extraction calculations				
CPU time (hr)	24.3	23.2	26.7	4.7
$\epsilon_{entry}(\%)$	79.9	84.6	76.3	83.3
ΔE (MeV)	1.54	1.39	1.81	0.95
E_{peak} (MeV)	243.12	242.96	242.89	242.96
Final results				
$\epsilon_{ex}(\%)$	15.4	18.0	15.4	17.8
zloss (%)	3.8	6.7	18.3	6.0
ΔE (MeV)	0.54	0.52	0.72	0.41
E_{peak} (MeV)	243.10	242.99	242.87	242.96

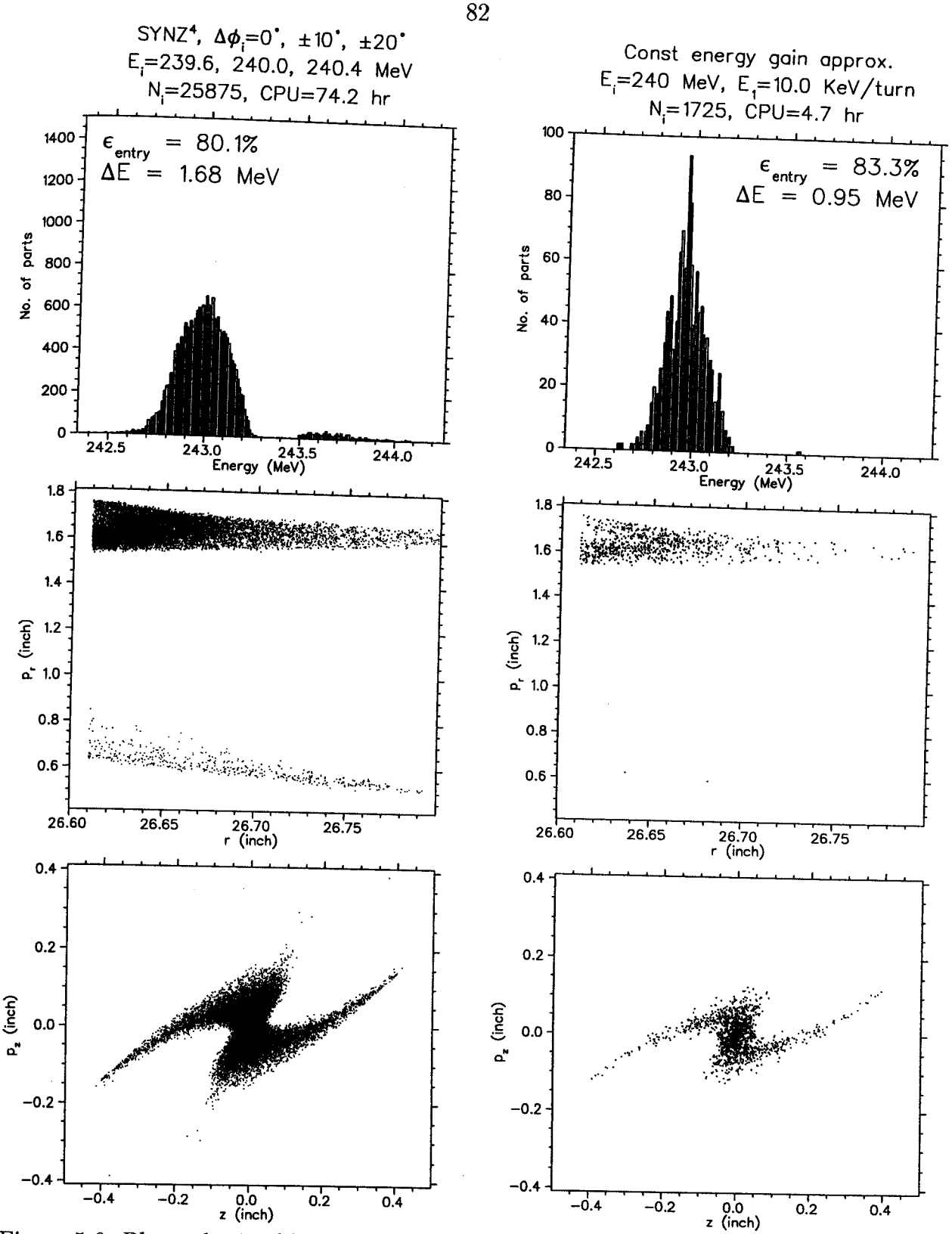

Figure 5.6: Plots, obtained by using the two versions of Z^4 code, show the distribution of energies in 0.01 MeV steps, r vs. p_r, and z vs. p_z in cyclotron units at $\theta = 336^o$ for those particles which successfully enter the extraction channel.

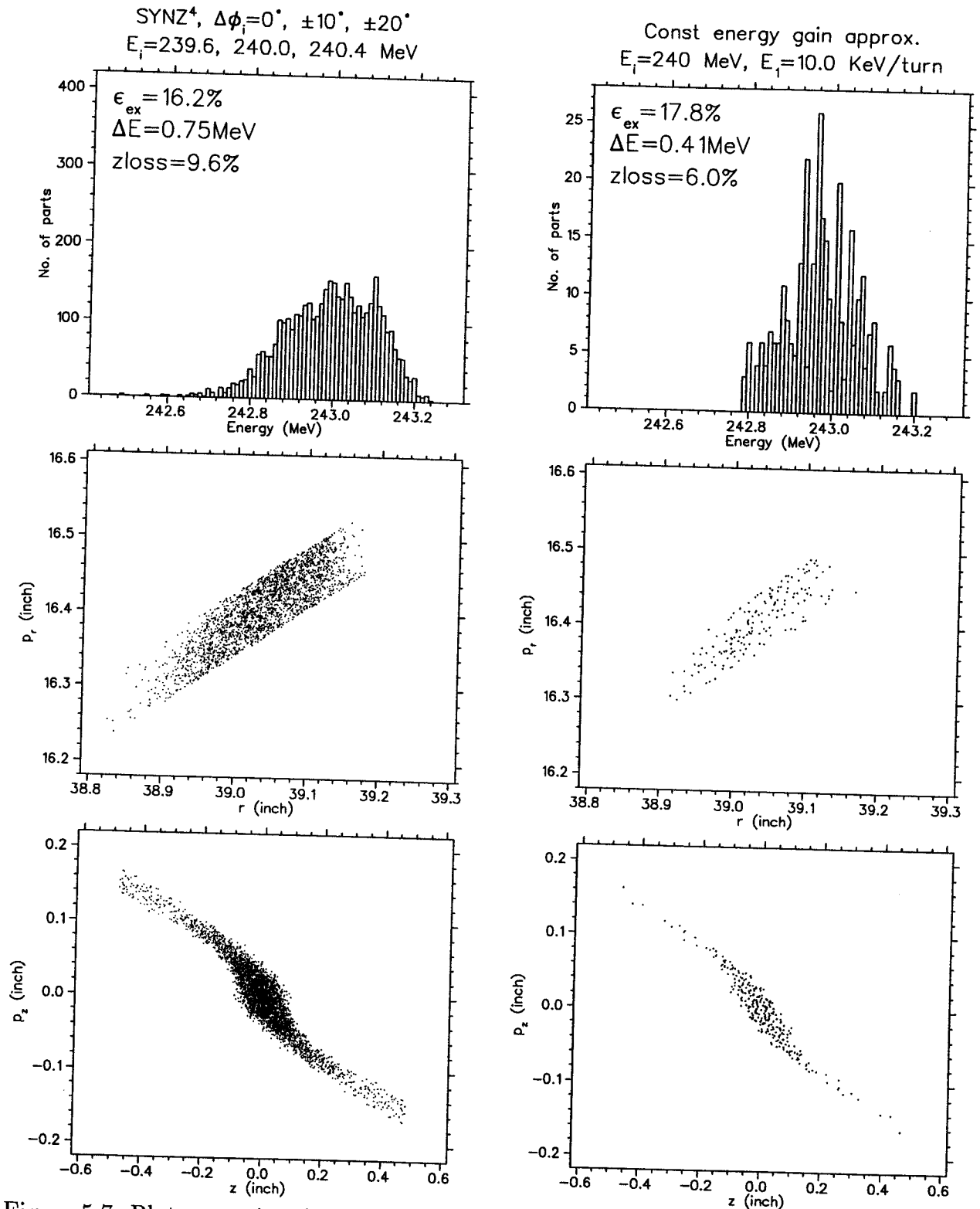

Figure 5.7: Plots, associated with the two versions of Z^4 code, show the distribution of final energies in 0.01 MeV steps, r vs. p_r, and z vs. p_z in cyclotron units at $\theta = 308^o$ where particles go off the field.

Chapter 6

Regenerative extraction

6.1 Introduction

"Regenerative extraction", the first system which we consider for extracting the beam from this synchrocyclotron (and the system which in the end seems most effective) is based on the process invented by Tuck and Teng and developed by LeCourteur in the 1950s [66] [67] [68]. The method as originally conceived uses two magnetic disturbances, a "peeler" and a "regenerator", usually 100° displaced. This $cos\, 2\theta$ dependence of the field disturbances induces radial oscillations with exponential increasing amplitude associated with the $\nu_r = 2/2$ stop band. The peeler introduces an outward impulse causing a phase delay, and the regenerator introduces inward impulse given a phase advance. After one revolution, the amplitude is increased and the phase is returned to the initial phase. As the beam accelerates out to the regenerator, the stability region corresponding to centered orbits shrinks and the separatrix limiting the stable region pulls gradually in through the beam spot. These dumped particles then move out along the asymptote until they reach the channel radius, at which point they either enter the channel or are lost depending on whether their position coincides with the channel aperture.

In general, the desired regenerator field shape can be produced by two blocks of

steel placed symmetrically above and below the median plane. Sometimes, the rapid fall off of the main field supplies the required peeler effect.

Our regenerator design is motivated by LeCouteur's work and is optimally found by extensive numerical calculations. LeCourteur [68] showed that a suitable regenerator strength would be

$$T = 0.2\rho + 0.2\rho^2 \tag{6.1}$$

One can also express the regenerator strength as

$$T = \frac{r_o}{B_o} \times \int \Delta B \, d\theta \tag{6.2}$$

where r_o and B_o are the radius and magnetic field measured at the start of the regenerator action. ΔB is the regenerator field and the integral is carried out on a circular orbit of radius $r_o + \rho$. The quantity ρ measures the distance from the last unperturbated orbit, and is measured in inches. The quantity θ is measured in radian.

As was pointed out in H. Blosser's paper [36]: The combination of energy spread, angular spread, vertical loss and a distorted object shape combine to make design of the extraction channel for synchrocyclotrons an extremely difficult problem. The typical energy spread, about 1-2 percent at the entrance of channel, corresponds approximately to the difference between the energy at which the stable region is just equal to the beam spot area and the energy at which the stable region has just vanished, whereas the exit beam will usually have spread of only a few tenths of a percent due to the limited momentum bandpass of the extraction system. In addition to the energy spread itself, the asymptote shifts in position on the phase diagram as the stable region shrinks, thereby imparting an additional spread in angle into the beam entering the channel. Distortion of the beam is induced by the half-integer resonance effect when the particle starts to increase the turn separation and becomes

off-center rapidly. Moreover, the axial instability may be induced at the coupling resonance by this beam off-center phenomenon.

The extraction efficiency, ε_{ex}, can be decomposed into two components

$$\varepsilon_{ex} = \varepsilon_{entry} \times \varepsilon_{trans} \tag{6.3}$$

where ε_{entry} is the channel entry efficiency and ε_{trans} is the transmission efficiency. The channel entry efficiency is given approximately by [69]

$$\varepsilon_{entry} \leq 1 - \frac{t}{\Delta r} \tag{6.4}$$

where t is the septum thickness of the first extraction element, Δr the turn to turn separation at the entrance of the first extraction channel. The equality in the above equation holds for the situation of no axial loss.

If the electrostatic deflector is used as the first channel, then 2-3 mm turn separation is probably sufficient to achieve high extraction efficiency, because the septum thickness of an electrostatic deflector can be 10 mils or less.

The typical extraction efficiency of synchrocyclotrons of the 1950s only reached a few percent level, and the external current reached in the territory of 0.05 μA. The extraction efficiency, external current and final energy of protons for selected synchrocyclotrons are listed in Table 6.1 [70] [71] [72], the last entry including improvements in an extensive upgrade program in the late 1960s.

The poor extraction efficiency for these old fashioned synchrocyclotrons is mainly owing to the poor quality of the internal beam, the thick walls of the magnetic channel which was used for the first element and insufficiently compensating field imperfections. High extraction efficiency, however, is desirable because the problems associated with septum cooling and machine activation due to high energy proton

Table 6.1: The extraction efficiency and external current of protons for selected synchrocyclotrons.

Name of machine	Energy (MeV)	Extraction eff. (%)	External cur. (μA)	First beam (year)	Res. $\Delta E/E$ (%)
Harvard	160	4	$\leq$0.05	1957	0.9
Berkeley	740	15	0.1	1946	x
Orig. Uppsala	192	1	0.005	1956	0.1
Impr. Uppsala	180	x	0.3	1991	x
Orig. CERN	592	10	0.1	1957	1
Impr. CERN	600	$\sim$70	5	$\sim$1975	$\sim$0.2

bombardment will be significantly reduced. The impressive 70 percent extraction efficiency for the CERN 600 MeV proton synchrocyclotron was achieved mainly by improving the quality of the internal beam and by the provision of a electromagnetic deflector, such that the disturbance in the main field are negligible [72]. We thus conclude that one of the crucial keys to achieving high extraction efficiency is good internal beam. Other extraction requirements, simply stated, are [42] [73] :

1. It must produce a sufficient separation between successive turns so that most of the ions can clear a septum and enter the exit channel.

2. Losses owing to axial blow up must be minimized.

3. The beam spot shape should be kept compact.

4. The extraction system should have sufficient aperture to transmit the desired current.

6.1.1 LeCouteur's Linear Regenerative Theory

The theoretical basis for the regenerative beam extraction [66] is briefly reviewed in this subsection. Assuming circular equilibrium orbits, the action of the peeler-

regenerator can be written as a series of impulses, thereby described by the transfer matrix

$$\begin{pmatrix} x \\ x' \end{pmatrix} = \begin{pmatrix} cos\nu_r f & \frac{sin\nu_r f}{\nu_r} \\ -\nu_r sin\nu_r f & cos\nu_r f \end{pmatrix} \begin{pmatrix} 1 & 0 \\ -R & 1 \end{pmatrix} \begin{pmatrix} cos\nu_r d & \frac{sin\nu_r d}{\nu_r} \\ -\nu_r sin\nu_r d & cos\nu_r d \end{pmatrix} \tag{6.5}$$

$$\times \begin{pmatrix} 1 & 0 \\ P & 1 \end{pmatrix} \begin{pmatrix} x_0 \\ x_0' \end{pmatrix} = \begin{pmatrix} \alpha & \beta \\ \gamma & \delta \end{pmatrix} \begin{pmatrix} x_0 \\ x_0' \end{pmatrix} \equiv \overline{M}_r \begin{pmatrix} x_0 \\ x_0' \end{pmatrix}$$

where x is the radial displacement from equilibrium orbit, x' is the corresponding velocity ($x' = dx/d\theta$), d is the angle between the peeler and regenerator ($f = 2\pi - d$), $P = -\frac{r}{B}\frac{\partial B}{\partial r} \times \theta_P$, $R = \frac{r}{B}\frac{\partial B}{\partial r} \times \theta_R$ and θ_P, θ_R azimuthal extension of the peeler and regenerator.

For the vertical motion, the transfer matrix $\overline{M}_v$ can be obtained by the following changes

$$\nu_r \rightarrow \nu_z\,, \quad P \rightarrow -P\,, \quad R \rightarrow -R \tag{6.6}$$

The stability condition is given by the trace of the matrix $\overline{M}$

$$\begin{aligned} &\alpha + \delta > 2 : unstable \\ &\alpha + \delta < 2 : stable \end{aligned} \tag{6.7}$$

For proper operation of the system, it is necessary to keep the vertical motion stable and to excite the radial motion. Then after n turns the radial motion can be written as

$$\begin{pmatrix} x \\ x' \end{pmatrix}_n = \overline{M}_r^n \begin{pmatrix} x_0 \\ x_0' \end{pmatrix} = K_1 e^{n\lambda} \begin{pmatrix} u \\ v \end{pmatrix} + K_2 e^{-n\lambda} \begin{pmatrix} u' \\ v' \end{pmatrix} \tag{6.8}$$

where e^{λ} and $e^{-\lambda}$ are the eigenvalues of the matrix $\overline{M}_r$ and can be found from the trace; $\begin{pmatrix} u \\ v \end{pmatrix}$ and $\begin{pmatrix} u' \\ v' \end{pmatrix}$ are the corresponding eigenvectors; K_1, K_2 are determined by $\begin{pmatrix} x_0 \\ x_0' \end{pmatrix}$. For a sufficiently large n, the last term of Equation 6.8 will dampen out,

and the phase of the oscillation is given by an eigenvector $\begin{pmatrix} u \\ v \end{pmatrix}$. The radial motion is therefore characterized by exponential increasing oscillation amplitude; the needed turn separation is achieved.

6.2 Extraction System

In this section the extraction system which we consider is assumed to consist of the existing pair of K500 electrostatic deflectors, a regenerator inside the empty dee in between, followed by the existing K500 magnetic channels of the passive type which are made with bars of saturated iron. Futhermore, all the channels are located in one of the existing rectangular holes in the K500 magnetic yoke.

The fields produced by the magnetic extraction elements are calculated by employing the charge sheet program [49]. These fields are added to the threefold symmetric 120° field map produced by iron, main coils and trim coils, thus giving the 360° total map which we use to study the beam dynamics.

6.2.1 Layout and Design Features

Our design process consisted of iterating back and forth between calculations of the field produced by the extraction devices, and computation of extraction orbits, in order to systematically improve the design parameters and optimize the extraction efficiency. Figure 6.1 shows the layout of our final design for the regenerative extraction system. It shows the arrangement of the extraction devices as well as the last five turns of a typical extracted orbit.

All the elements shown in Figure 6.1 are also listed in Table 6.2 together with their main parameters. E, R, M and C characterize an electrostatic deflector, the regenerator, a magnetic channel and a compensating bar, respectively. The parameters

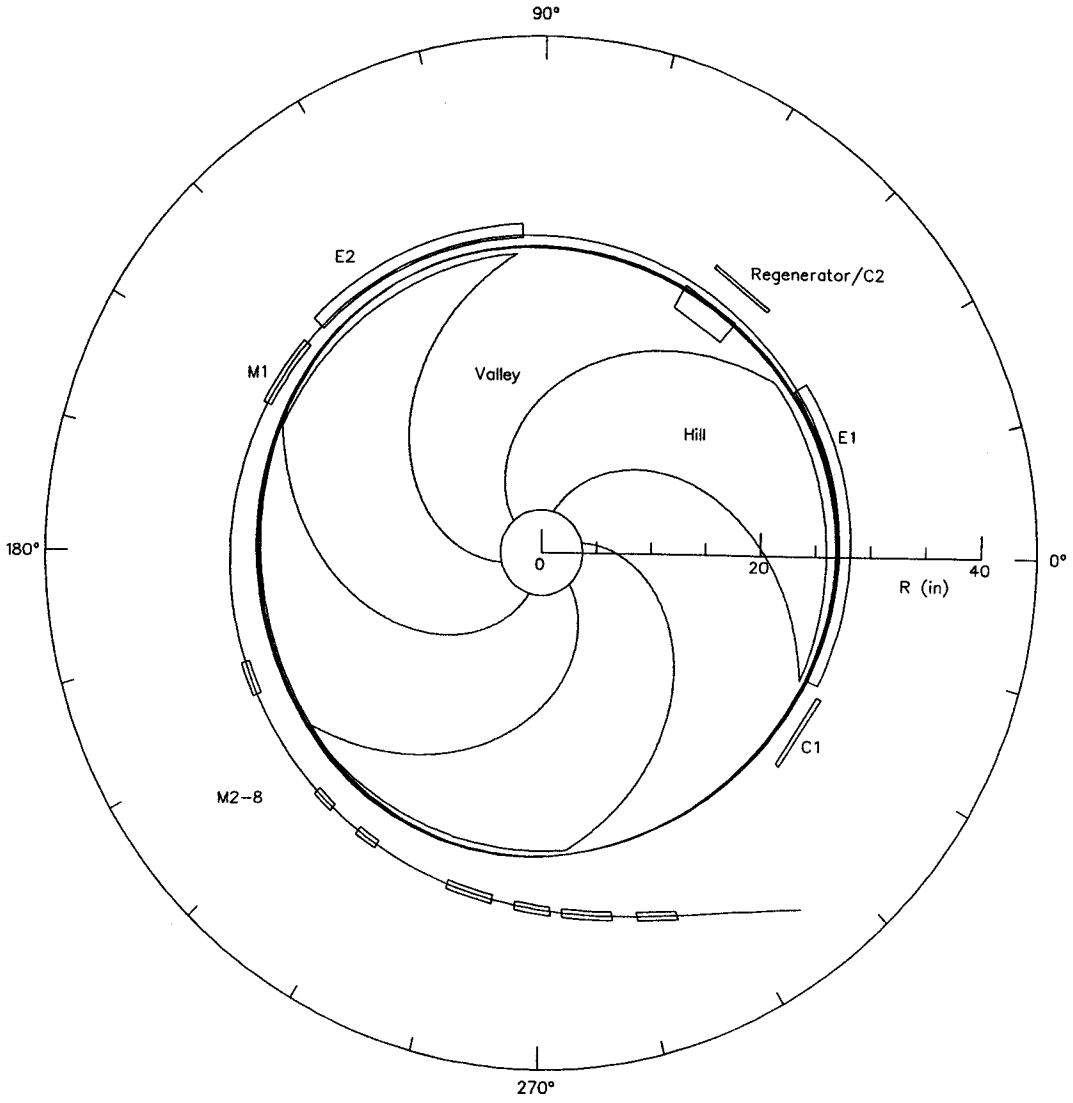

Figure 6.1: Layout of the extraction system showing the arrangement of the extraction elements as well as the last five turns of an extracted orbit.

Table 6.2: Extraction element parameters

	Θ_i (deg)	Θ_f (deg)	R_i (inch)	R_f (inch)	M.A. (inch)	E (kv/cm)	ΔB (kg)	$\partial B/\partial x$ (kg/inch)	R_c (inch)
E1	-24	32	26.66	27.31	0.4	94			
E2	94	136	27.56	27.99	0.4	94			
R	49	61							
M1	140	153	28.01	28.07	0.5		1.2	8.8	
M2	200	206	28.55	28.65	0.5		1.2	8.8	
M3	226	230	29.11	29.22	0.5		1.2	8.8	
M4	236	240	29.40	29.53	0.5		1.2	8.8	
M5	256	262	30.20	30.54	0.5		1.2	8.8	
M6	266	272	30.79	31.25	0.5		1.2	8.8	
M7	276	282	31.62	32.29	0.5		1.2	8.8	
M8	286	292	32.84	33.89	0.5		1.2	8.8	
C1	320	334							28.1
C2	46	58							29.5

are the initial and final azimuths of each element, Θ_i and Θ_f, the central ray radius R_i and R_f at angles Θ_i and Θ_f, the mechanical aperture M.A., the electric field E, the magnetic field bias ΔB, the focusing gradient $\partial B/\partial x$, and the compensating bar radius R_c defined in Figure 6.3.

Two electrostatic deflectors, the first one 56° long and the second 42° long, are positioned in correspondence with two successive hills. An electrostatic deflector is chosen as the first exit channel element both because of the thin septum and because of the ease with which an electric field can be confined to a desired region. In contrast, magnetic fields have a much higher bending power, but spread over a broad region, influence previous orbits and require laborious detailed trimming to restore these orbits to an acceptable state. Moreover, a 2-3 mm turn separation is sufficient to achieve high channel entry efficiency with the very thin septum of the electrostatic deflector. The electrostatic deflector is therefore a great help in meeting the extraction requirements.

The regenerator is placed in the valley between the two electrostatic deflectors - details of its design are discussed below.

Following the electrostatic deflectors and regenerator, there are eight magnetic channels, the first of which is 13^o long and is adjacent to the second deflector. The other seven channels are 6^o each, except M3 and M4 which are shortened to 4^o to avoid radial overfocusing. Figure 6.2 shows the cross section geometry of a typical focusing bar, and the median plane field and the corresponding field gradient as a function of x (the radial displacement from the center of the aperture). The strong gradient of the focusing bars opposes the radial defocusing gradient associated with the edge region of the machine field through which the extracted beam must pass. As shown in this graph, the focusing gradient is strong and nearly constant over 80 percent of the aperture, with an average 8.8 kg/inch for the aperture width of 0.5″. In addition, the focusing bar produces a negative (deflecting) field near the center of the aperture, which provides valuable assistance to the electrostatic deflectors in breaking the beam free of the strong magnetic field.

Relevant dimensions of the compensating bar C_1 and C_2 are shown in Figure 6.3. C_1 is designed to compensate the field perturbation on the inner orbit due to M_1, and is therefore at 180^o from the latter. C_2 compensates the overall effect of the seven remaining channels.

A section view of the regenerator is shown schematically in Figure 6.4. The three shims in front of the regenerator are used to reduce the undesired fringe field. The value of the combined field defect $\int \Delta B d\theta$ of the regenerator and its shims, and the corresponding field radial derivative as a function of radius are shown in Figure 6.5. The result using LeCouteur's formula is also shown in this graph.

The operation of the system is illustrated in Figure 6.6. Here the peeler (fall-off

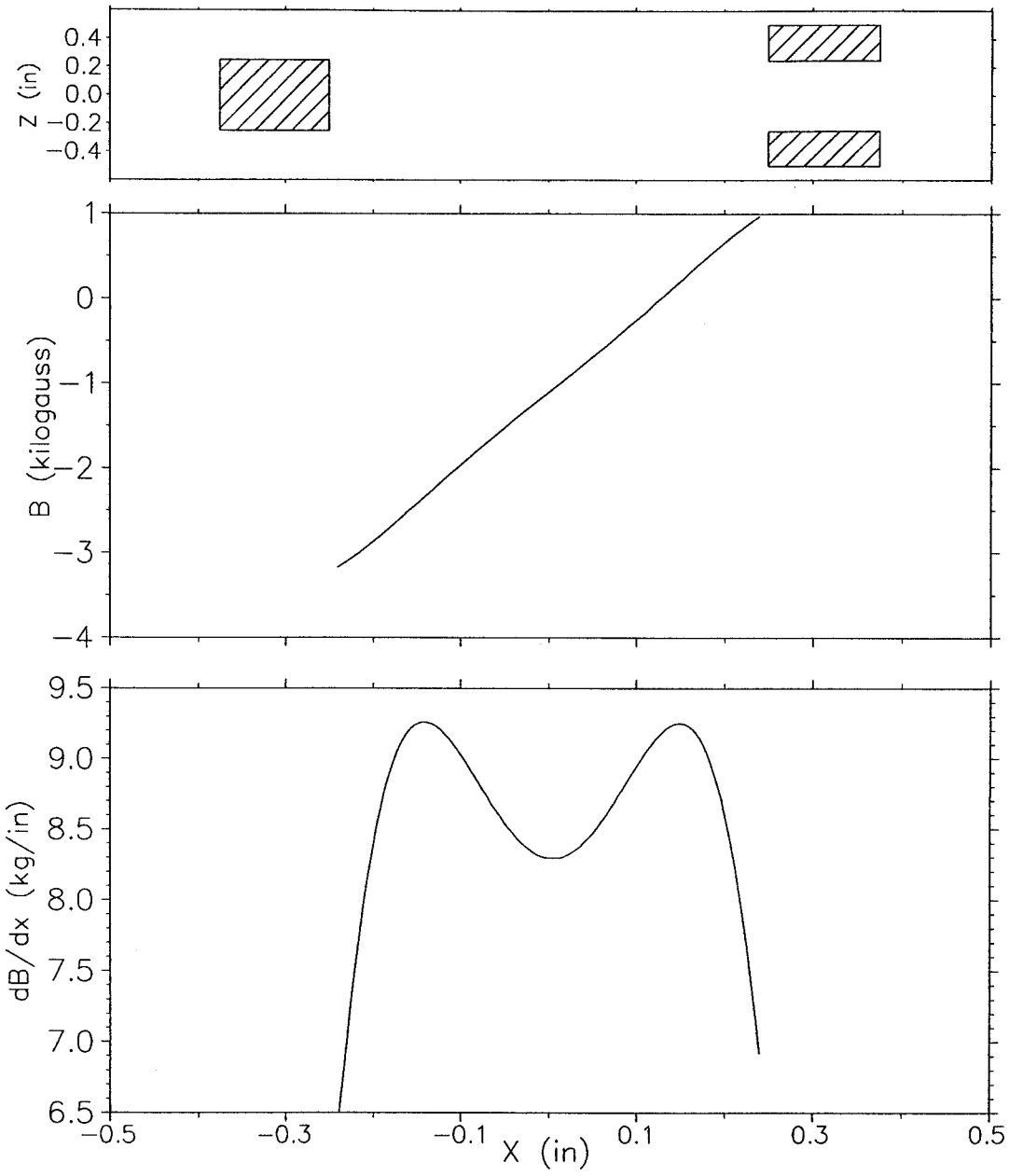

Figure 6.2: Top: schematic cross section of the magnetic focusing channel (Note x and z are not plotted in the same scale). The middle and lower panels represent the field and the gradient across the channel respectively.

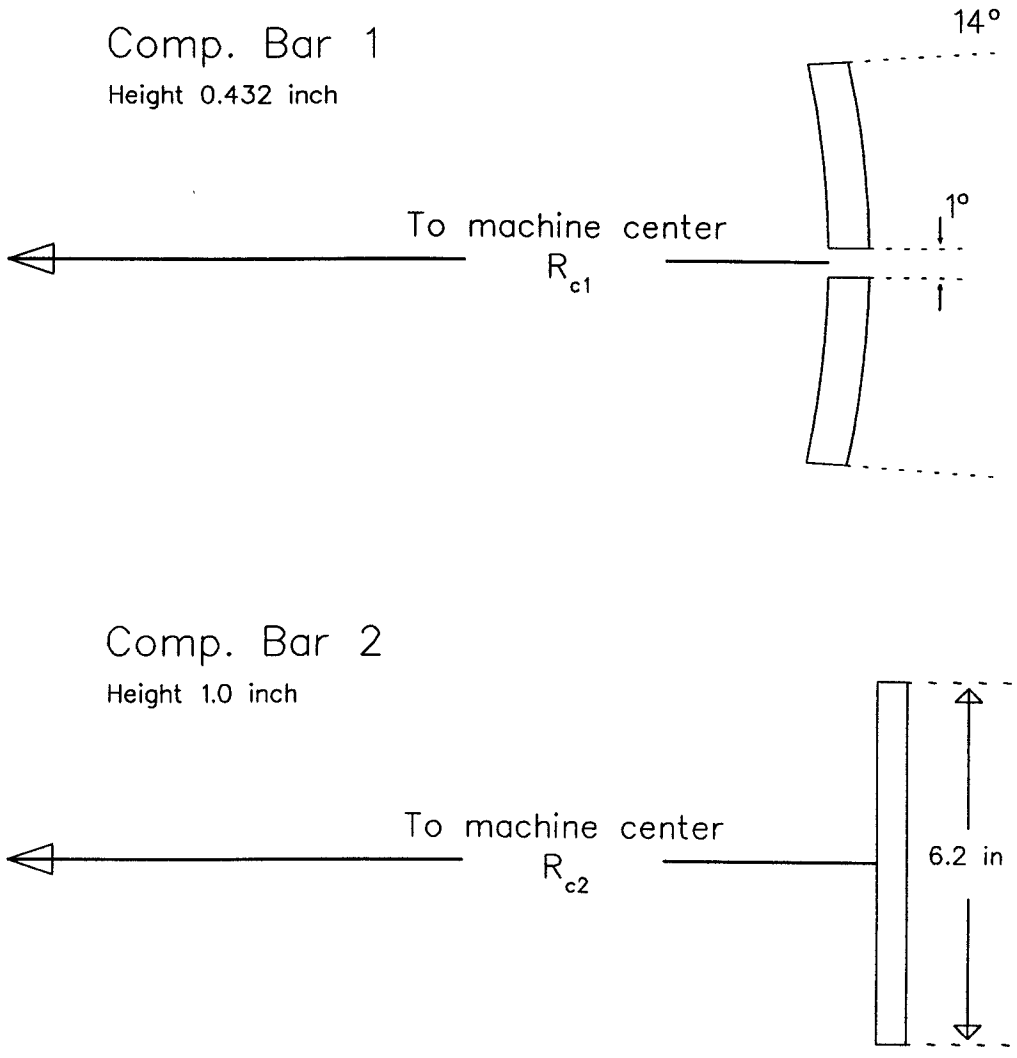

Figure 6.3: Median plane section of the compensating bars.

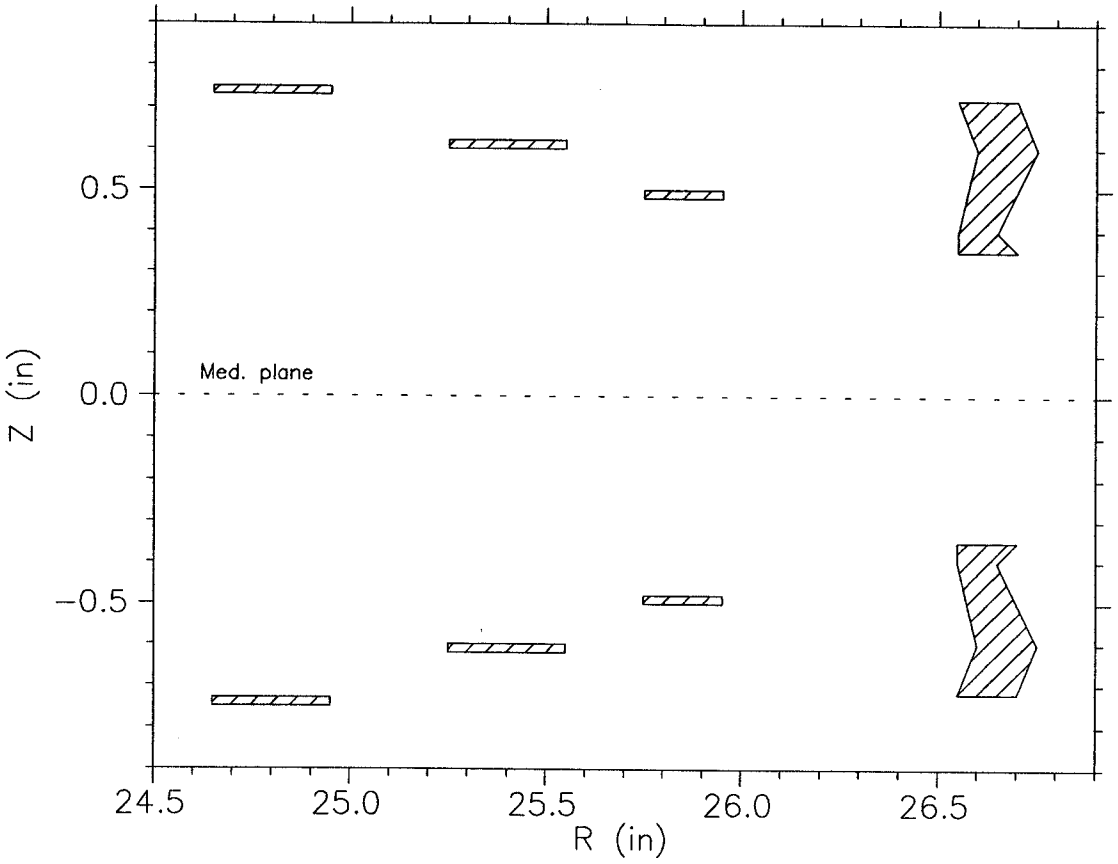

Figure 6.4: Regenerator and shim geometry.

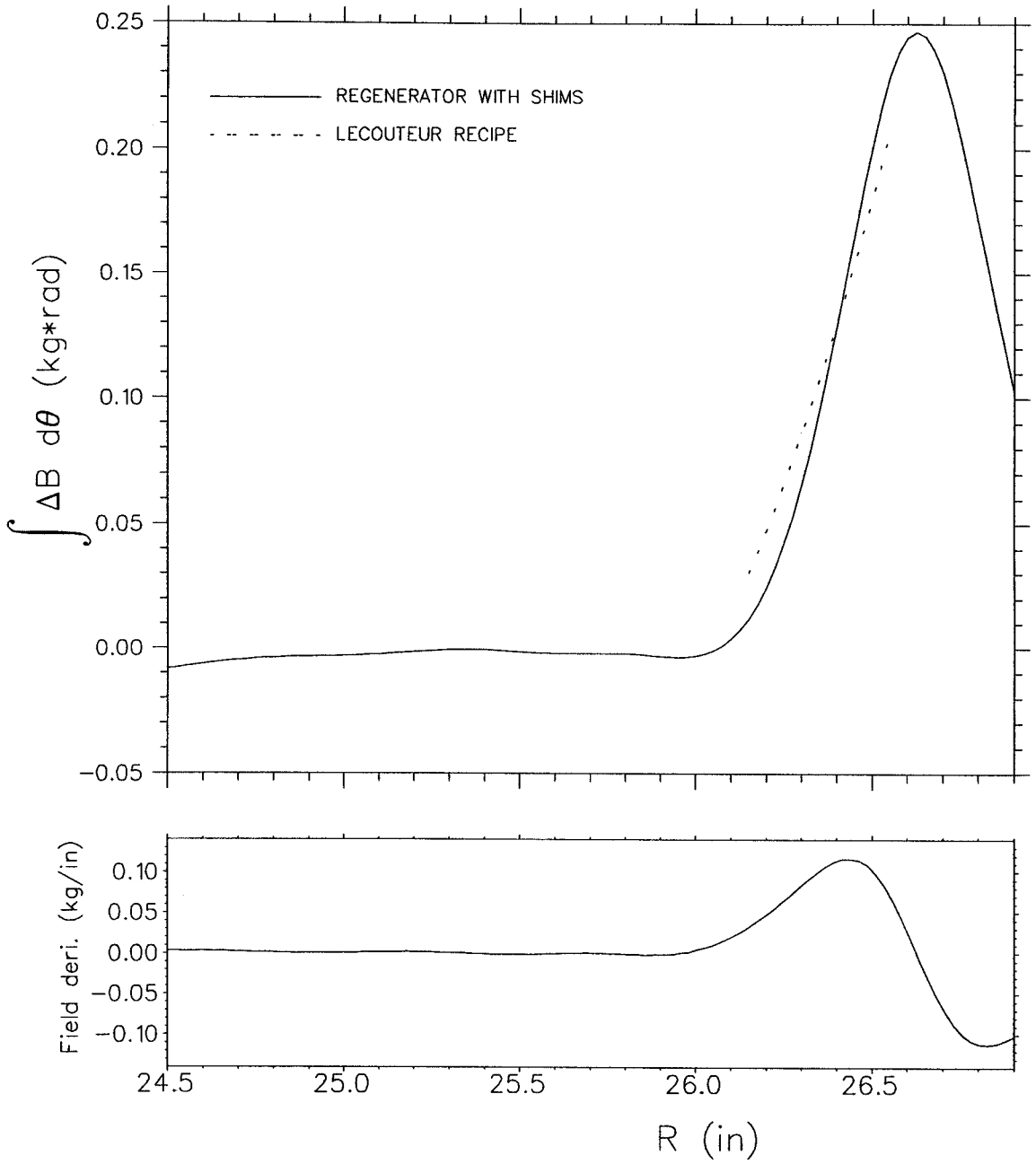

Figure 6.5: Regenerator field defect and its radial derivative as a function of radius.

edge field) introduces an outward impulse causing a phase delay, and the regenerator introduces inward impulse, giving a phase advance. After one revolution, the amplitude increases and the phase returns to the initial phase.

A bump coil (the outermost K500 trim coil with the coil on each hill powered separately to provide azimuthal adjustment) is employed to compensate for residual field imperfections produced by the focusing channels and compensating bars in the proximity of the $\nu_r = 1$ resonance in order to facilitate the resonance transverse. The correcting coil technique has been adopted by a number of cyclotron facilities, like that of Tokyo cyclotron (denoted electromagnetic shims) [61], Uppsala cyclotron (denoted harmonic coils) [74], etc. The first harmonic radial profile of this bump coil is shown in Figure 6.7. The field contribution from the bump coil is thus to good approximation simply

$$B_{bump}(r,\theta) = B_1(r) \times cos(\theta - \phi_1) \tag{6.9}$$

and this is the form assumed by the orbit tracking programs. The amplitude and phase of the first harmonic bump are denoted as B_1 defined in Figure 6.7 and ϕ_1, respectively.

6.3 Beam Dynamics

6.3.1 Pre-extraction Orbit Computations

The radial and vertical focusing frequencies as a function of energy in the regenerative extraction field are given in Figure 6.8. As in previous chapters the focusing frequencies ν_r and ν_z are plotted as ratios of the actual focusing frequencies to the orbital frequency and are hence dimensionless. The fringe fields of the extraction elements cause the central stable region to shrink to zero area at 243.3 MeV, the $\nu_r = 1$ region,

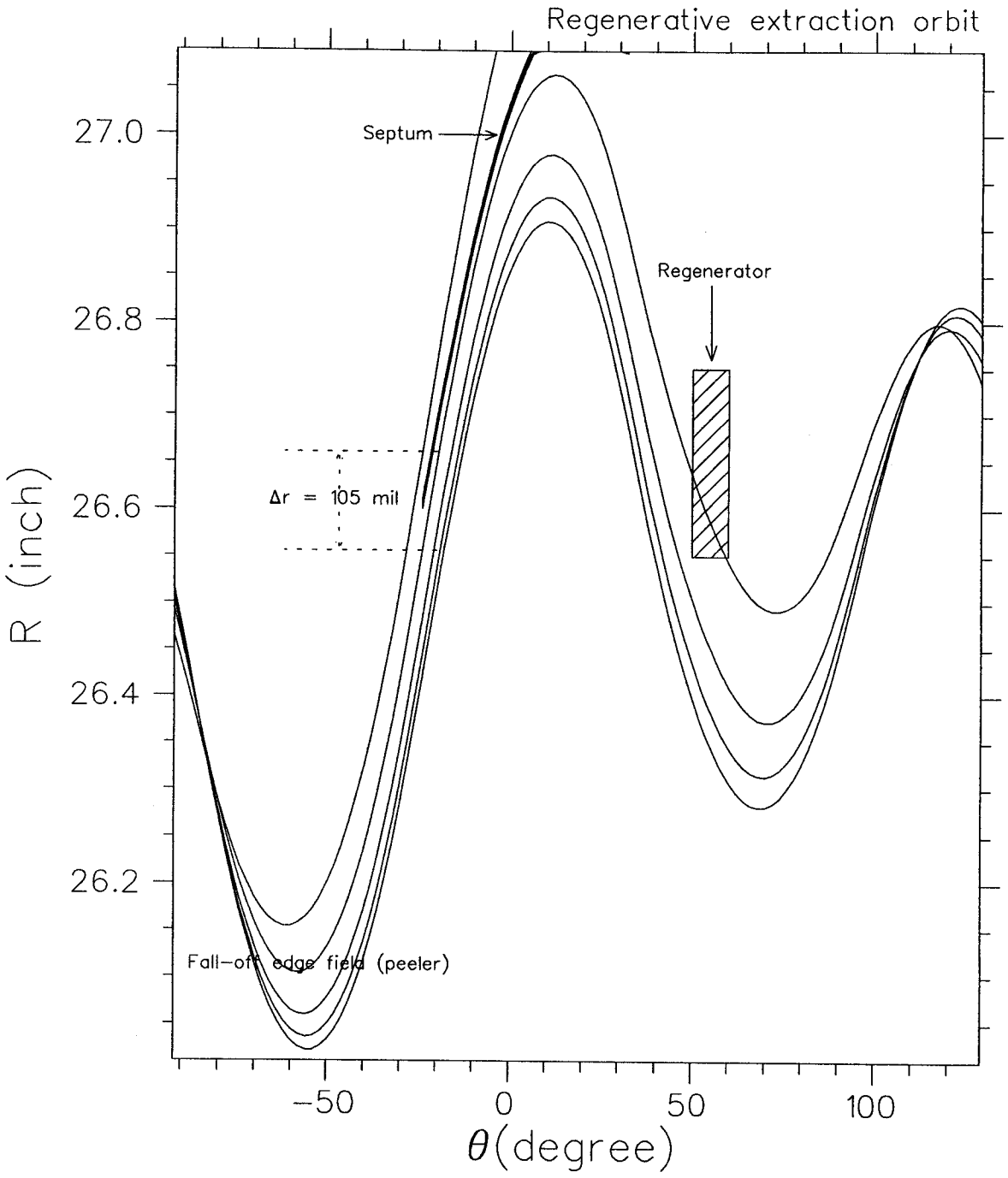

Figure 6.6: Plot of r vs. θ for the last five turns of an extracted orbit showing the action of regenerator-peeler system. The radial motion is characterized by exponential increasing oscillation amplitude; the resultant turn separation at the entrance of the channel is about 0.1″. Two nodes of oscillation are clearly seen at -80^o and 110^o.

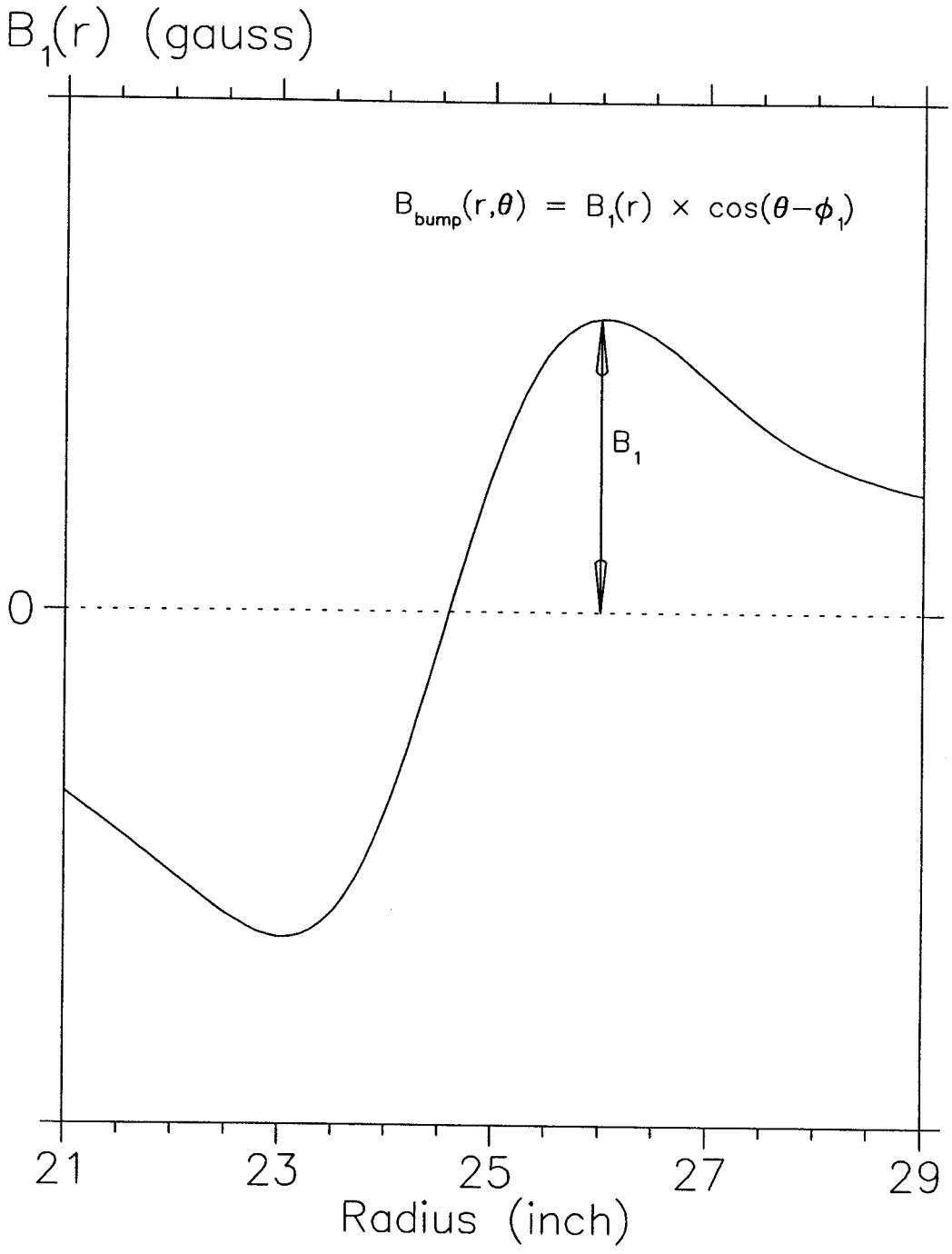

Figure 6.7: First harmonic bump used in extraction calculations as function of radius.

Table 6.3: The resonances in the extraction region.

Resonance	Driven by	Occurs at (MeV)
$\nu_z = \frac{1}{2}$	$\frac{\partial B_1}{\partial r}$	240.70 - 241.84
$\nu_r = 2\nu_z$	field derivatives & amplitude	241.19
$\nu_r = 1$	B_1	243.30 - 243.52
$\nu_r = \frac{2}{2}$	regenerator	246.8 $\rightarrow$

and then reappear at 243.52 MeV. In addition, the regenerator, due to its strong field gradient, shifts ν_r into the $\nu_r = 2/2$ stop band at an energy of 246.8 MeV.

The important features of the major resonances encountered near the edge of the machine are listed in Table 6.3. The $\nu_r = 1$ resonance, in particular, occurs when the average field ceases to increase with radius and turns over into the usual magnetic edge fall off. In the absence of the field imperfections the central stable region vanishes instantaneously at the resonance energy and then reappears. On the other hand, if field imperfections are included, a forbidden band (or stop band) where no central stable region exists occurs due to the influence of the field imperfections.

Figure 6.9 shows these features in a radial phase plot sequence where the energy is increased from below to above the $\nu_r = 1$ resonance. It shows the behavior of the separatrices in the phase space as the resonance is traversed. The "one-corner opening" orientation associated with the field imperfections at $\nu_r = 1$ radius is clearly indicated in the upper two panels.

In the vicinity of the resonance, a substantial fraction of the beam would be outside the stability limit. The large number of turns the particles spent in the unstable region in combination with the fast motion of the phase "fluid" shown in Figure 6.9 may result in beam loss.

Figure 6.10 shows the schematic radial phase space plots which depict the tran-

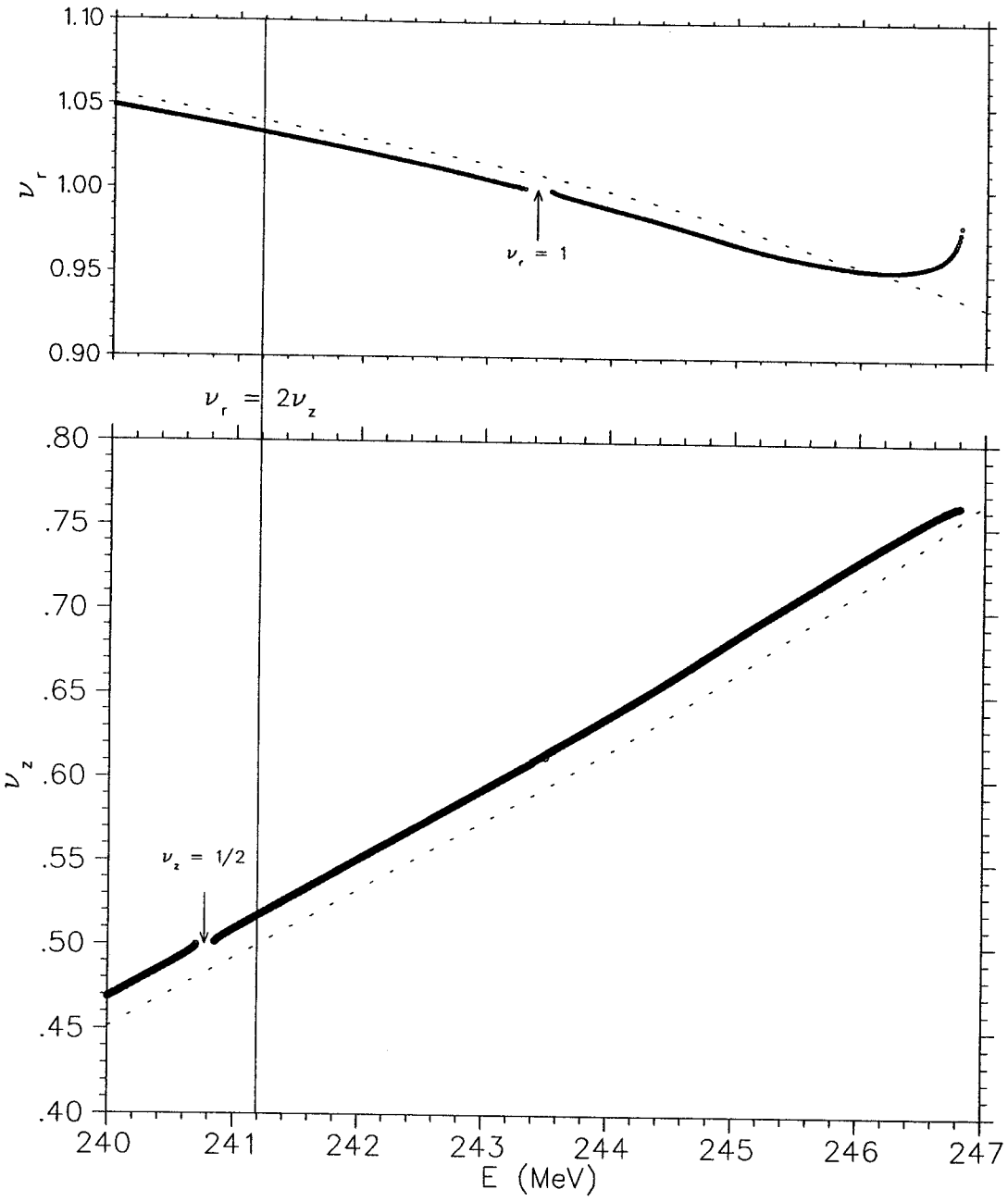

Figure 6.8: Plots of focusing frequencies as function of energy in fields with (solid curves) and without (broken curves) fringe field, produced by the extraction devices (a $B_1 = 2.7$ gauss bump used).

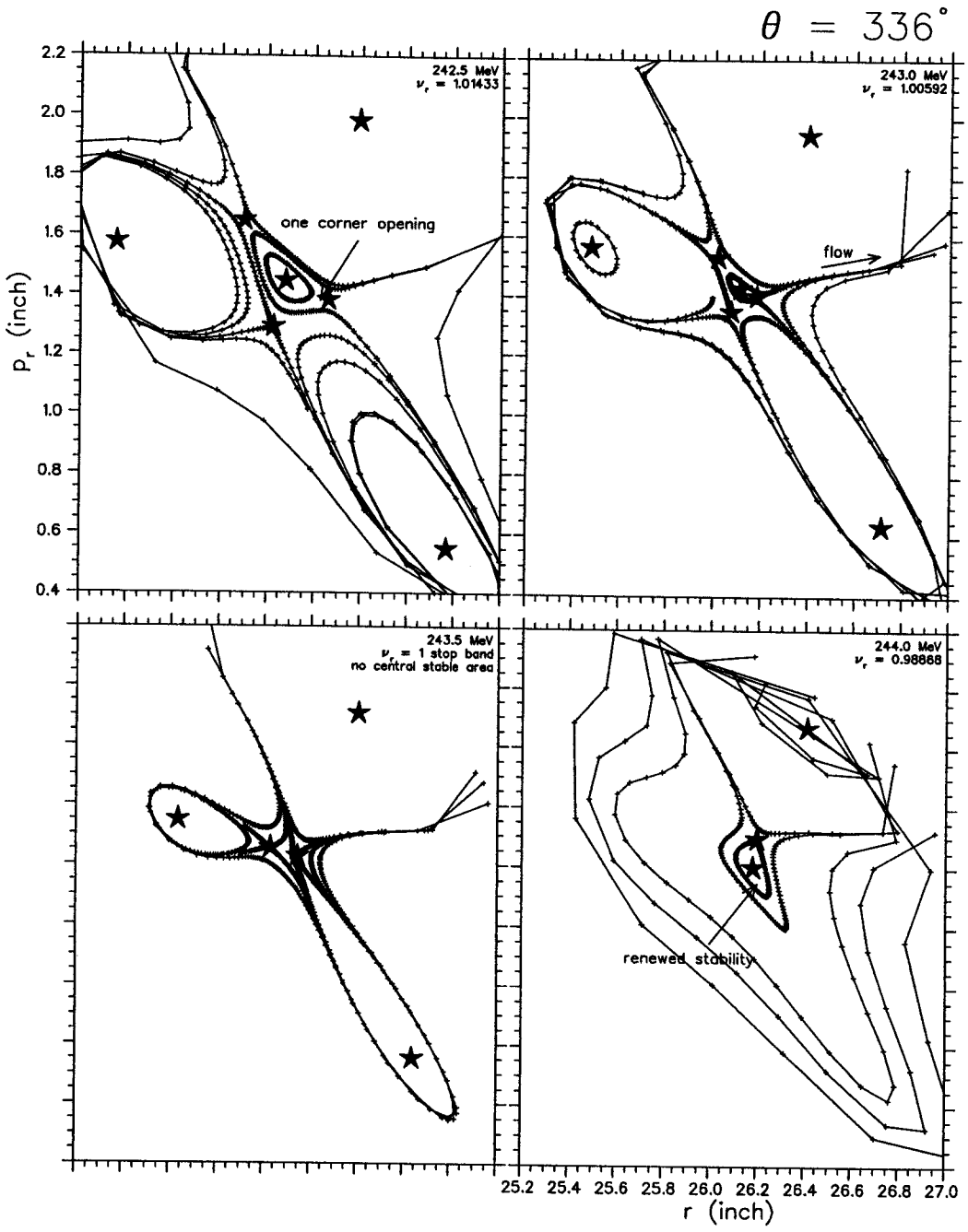

Figure 6.9: Schematic radial phase space plots show the behavior of the phase space regions as the $\nu_r = 1$ resonance is traversed. The stars denote the fixed points and the lines connect positions on successive revolutions of coasting orbits evolving from given starting conditions.

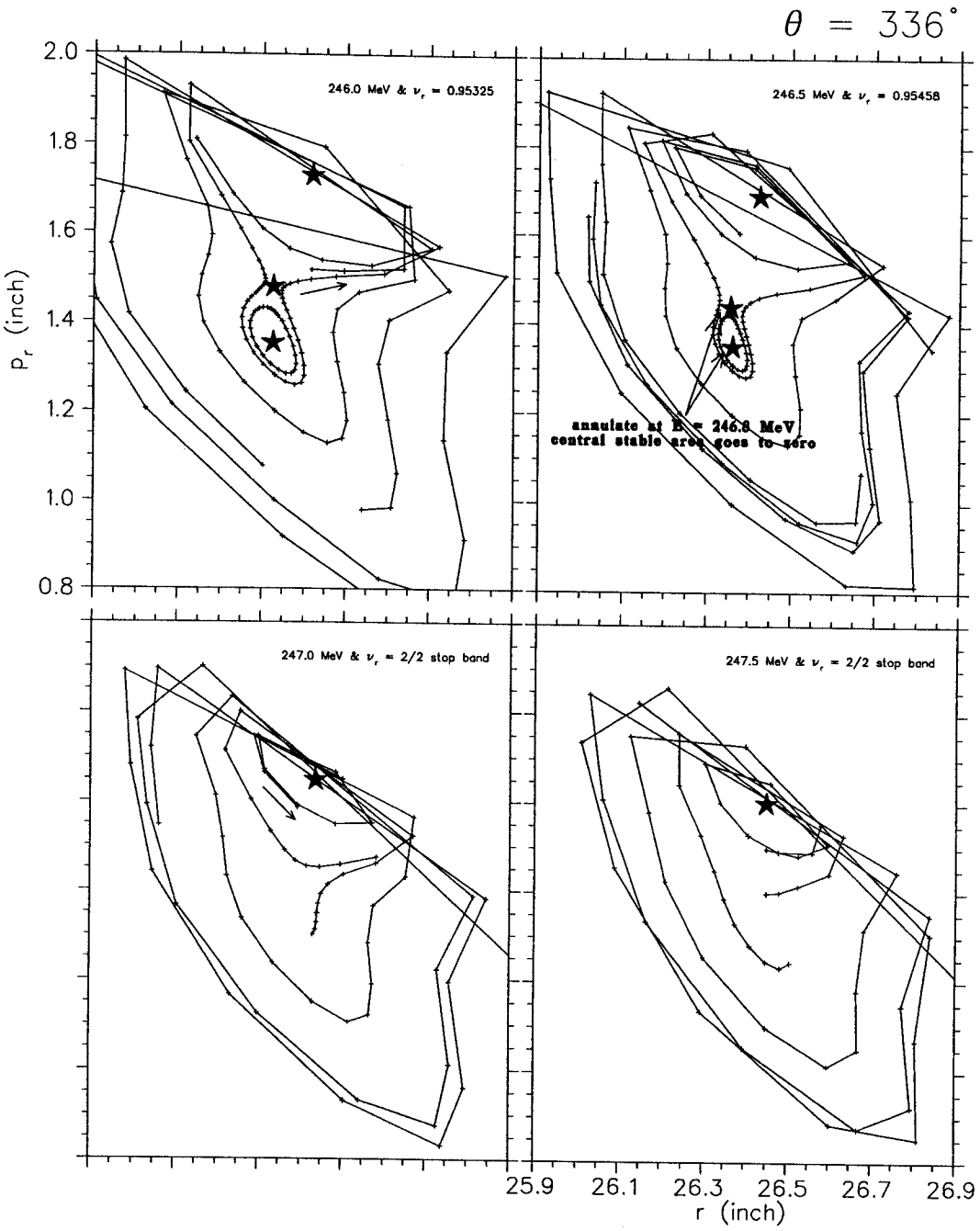

Figure 6.10: Schematic radial phase space plots show the behavior of the phase space regions under the influence of regenerator.

sition into the stop band at the resonance $\nu_r = 2/2$, driven by the steep rising field portion of the regenerator. The central stable region shrinks to zero rapidly as an energy of 246.8 MeV is being approached. This is good in that the energy spread will be smaller as the vanishing rate of stable area increases. The beam will be dribbled off as it accelerates toward the regenerator. The dumped particles then move along the asymptotes which goes around the hill-type stable fixed point during the extraction process. The turn spacing as the beam enters the extraction system is about 0.1″.

An example of the midplane motion of an accelerated beam is depicted in Figure 6.11; 2671 orbits uniformly distributed in a 0.5 mil by 0.5 mil rectangular grid covering the interior of an initial eigenellipse at E = 240 MeV are tracked and show the effect of $\nu_r = 1$ resonance traversal and the regenerative extraction system. The beam goes from an ellipse to a distorted pear with a long thin tail after passing through the $\nu_r = 1$ resonance corresponding to the "one corner opening" orientation shown in Figure 6.9. It then undergoes a drastic deformation under the influence of regenerator at about 246.8 MeV; the portion which flows out of the stable region elongates emphatically due to the fast phase flow on the asymptote. Furthermore, it is clearly seen that there is no real turn separation of the whole beam, but good turn spacing is achieved for individual particles by the action of regenerator. Therefore, we inevitably lose some fraction of the beam by striking the septum head-on. The channel entry rate thereby will be improved by an increase of the ratio between the turn separation of the individual particle and the thickness of the septum (Equation 6.4).

The starting radial and vertical phase positions for the pre-extraction orbit runs are depicted in Figure 6.12. The dotted curves give the radial and vertical eigenellipses with initial betatron amplitude 30 mil and 20 mil respectively. Note that if the nonlinear forces are negligible the normalized phase area will be constant and coasting orbits in the phase plot will fall on an ellipse, the "invariant eigenellipse" characteristic

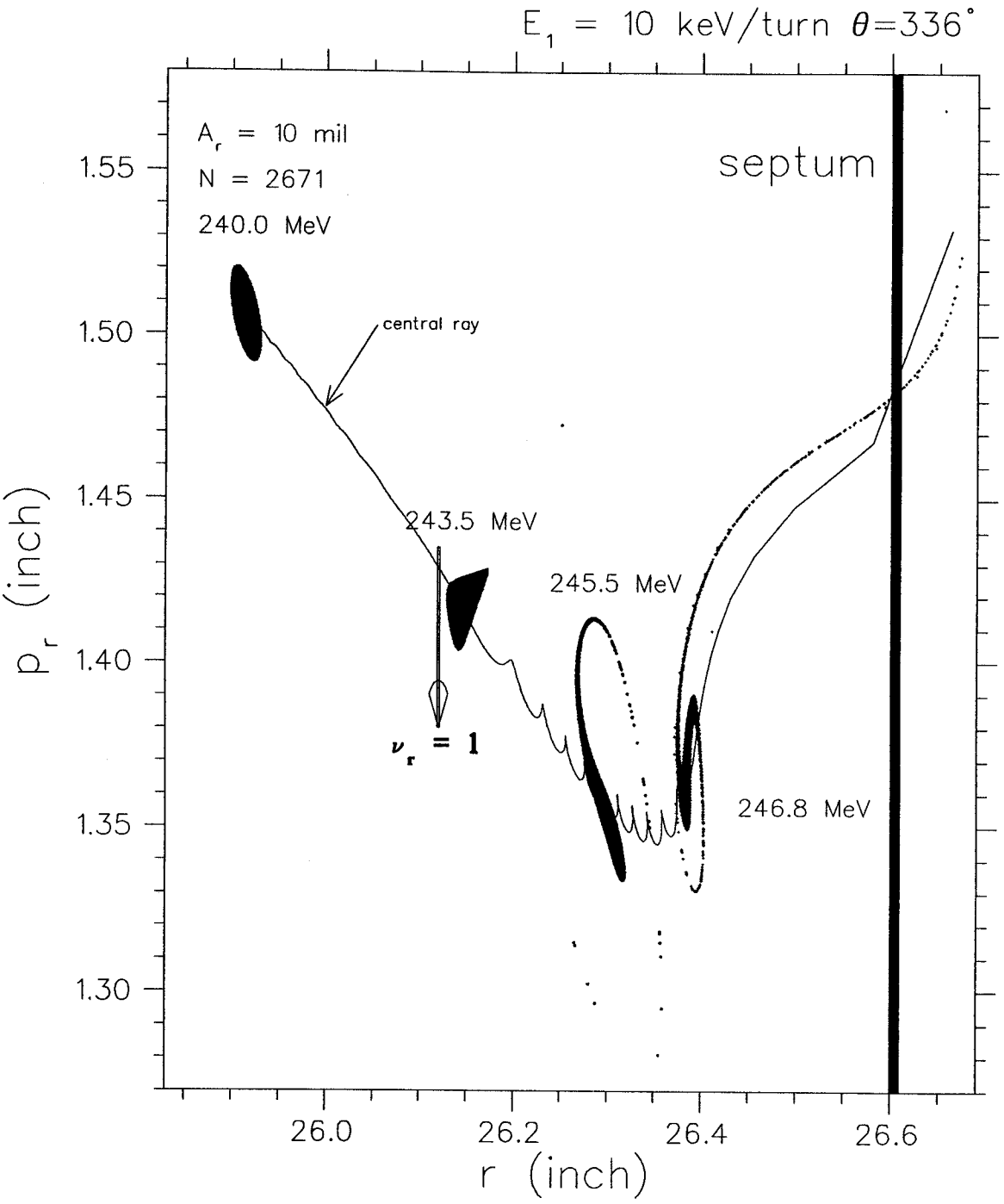

Figure 6.11: Central ray orbit and radial ellipses showing beam behavior at various energies.

of the linear motion. Futhermore, the rectangular grids correspond approximately to a constant current density physical beam. The starting energy is selected at 240 MeV, 70 turns before the $\nu_z = 1/2$ resonance which is the first resonance met in the extraction region.

The orbits are lost radially if they hit the extraction channel elements and lost vertically if they exceed a vertical amplitude limit of 0.5″. The summary of the accelerated orbit calculations are shown in Figures 6.13, 6.14 and 6.15.

The vertical beam envelope is given in Figure 6.13. It shows both the effects of the resonances and the axial instability induced by the "beam off-center". As orbits are pushed off centre rapidly due to either the $\nu_r = 1$ resonance traversal or the regenerative action, the orbits move further and further into the nearby coupling resonances, so that the axial instability may be encountered (beam off-center effect).

The energy spectrum for the particles which enter the aperture of the first electrostatic deflector is given in Figure 6.14. Two groups of particles are identified. The $\nu_r = 1$ stop band traversal accounts for the low energy group, while the high energy group is associated with the action of the regenerator. We see most of the particles pass successfully through the $\nu_r = 1$ resonance, thus we might expect a good extraction efficiency. In addition, the multi-peaks in energy spectrum, though quite surprising at first sight, are principally an effect of the phase space distortion associated with the $\nu_r = 1$ resonance.

The radial and axial phase distributions of the beam at the entrance of the electrostatic deflector are shown in Figure 6.15. It seems that the beam spot is quite confined in both motions. A 10 mil electrostatic septum with its entrance positioned at the radius of 26.605″ gives optimal extraction efficiency.

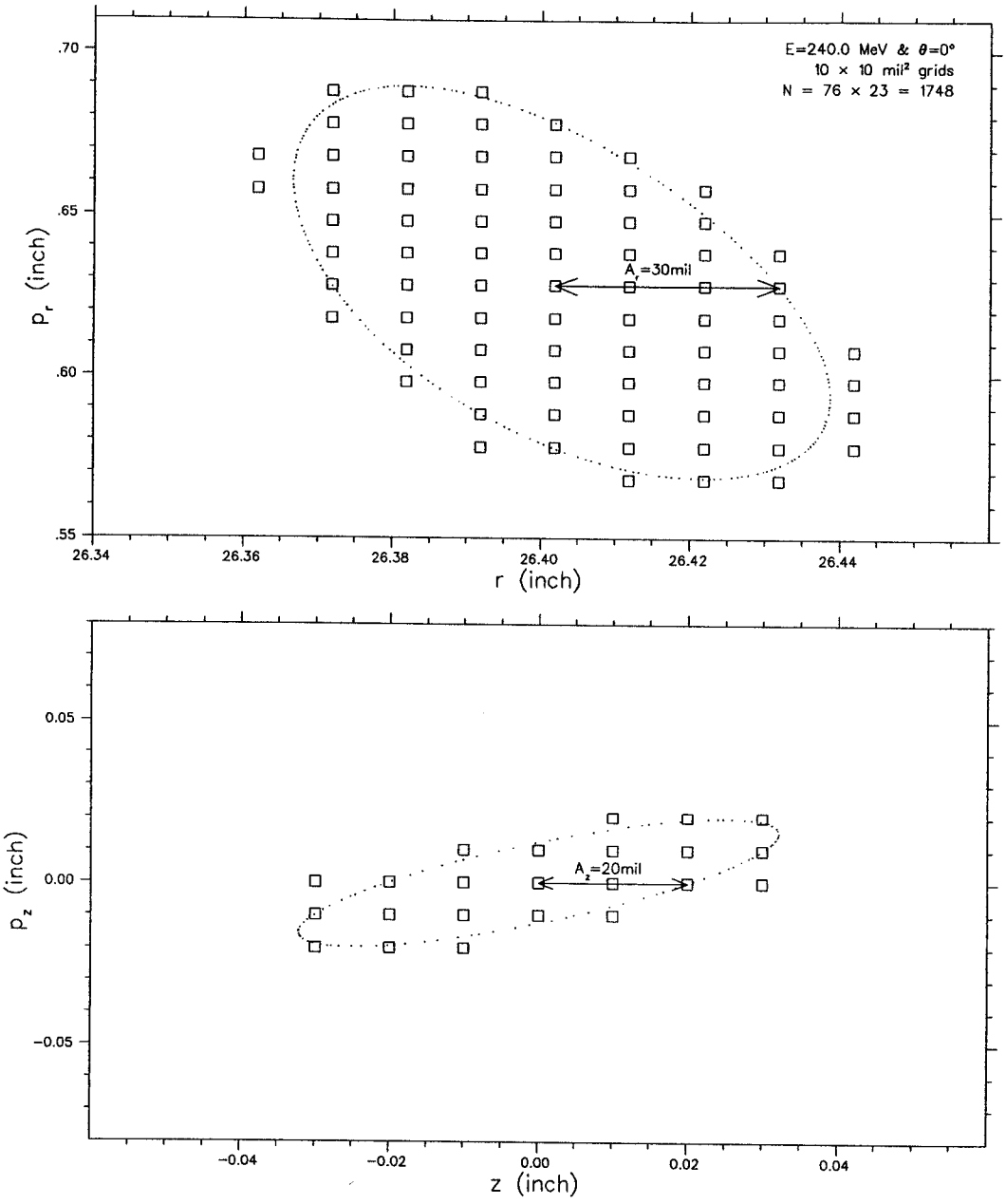

Figure 6.12: Initial $(r,\ p_r)$ and $(z,\ p_z)$, indicated by the squares, at E = 240 MeV and $\theta = 0^o$ used for accelerated orbits runs. Note A_r and A_z used hereafter are defined above.

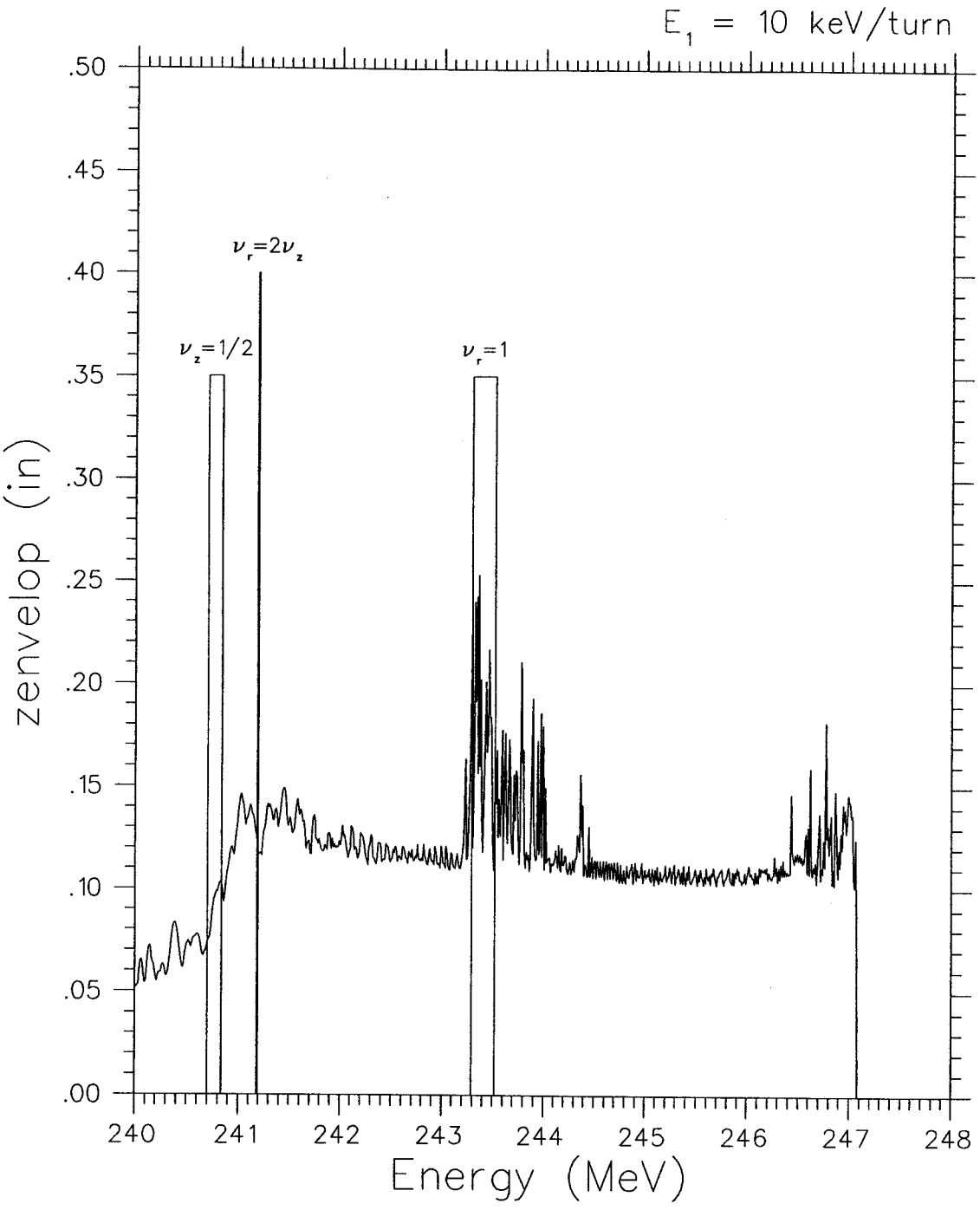

Figure 6.13: Vertical beam envelope as function of energy.

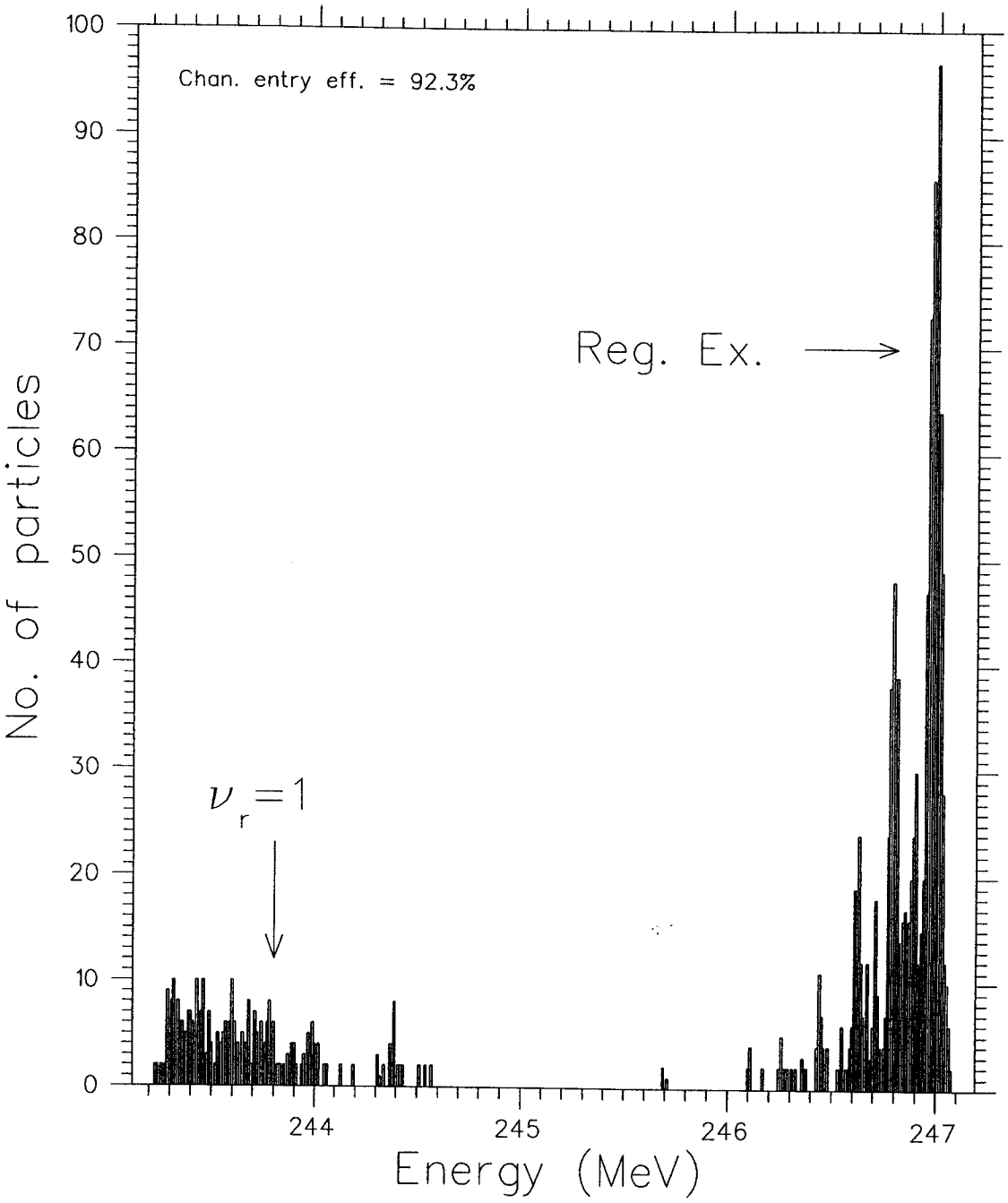

Figure 6.14: Distribution of energies for the particles entering successfully the first extraction channel at $\theta = 336°$.

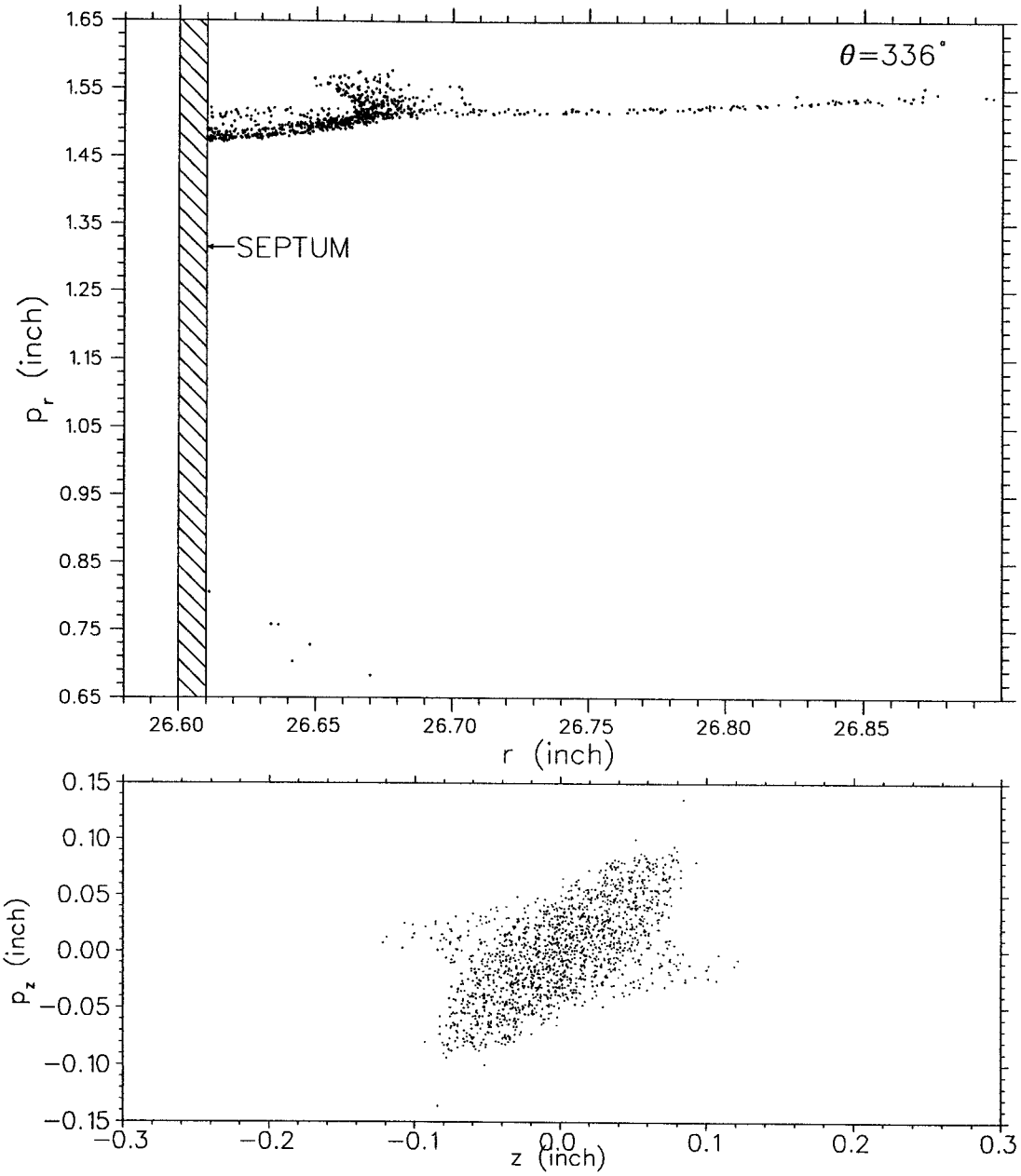

Figure 6.15: Radial and axial phase plots at the entrance of the first extraction channel ($\theta = 336^o$) showing the resultant distribution for those orbits that successfully enter the channel.

6.3.2 Extracted Beam Optics

The particles which successfully enter the aperture of the first electrostatic deflector provide the input data for computing the optical characteristics of the external beam. These calculations are carried out by utilizing the DEFLZ800 code. This program treats only linear vertical motion and also calculates only the coupling of the radial into the vertical motion, but omits the reverse coupling. These are, however, appropriate simplifications due to the fact that the extracted path is shorter than one turn and the axial displacement is much smaller relative to the radial displacement.

The acceptance of the extraction system is found by tracking displaced rays as shown in Figure 6.16, then using these results to determine the maximum tolerance in phase space and energy at the channel entrance. From these results the energy spread in the external beam is expected to be 0.8 MeV or 0.32% of the extraction energy.

Plots of the radial and vertical envelopes for the extracted beam are given in Figure 6.17. The loss histogram, given in 2^o steps at the bottom of the figure, depicts the loss of the extracted orbits due to hitting the walls of channels or failing to enter channels. We see that there is a significant beam loss at the entrance of the second electrostatic deflector. The main reason is that the particles in the low energy group will not enter the second electrostatic deflectors after they exit from the first electrostatic deflector; they just go radially inward.

The final energies, radial and vertical phase distributions of the extracted beam at $\theta = 308^o$ where particles go off the field, are given in Figure 6.18. This figure indicates an energy spread of 800 KeV (upper panel) and a quite limited beam size (middle and bottom).

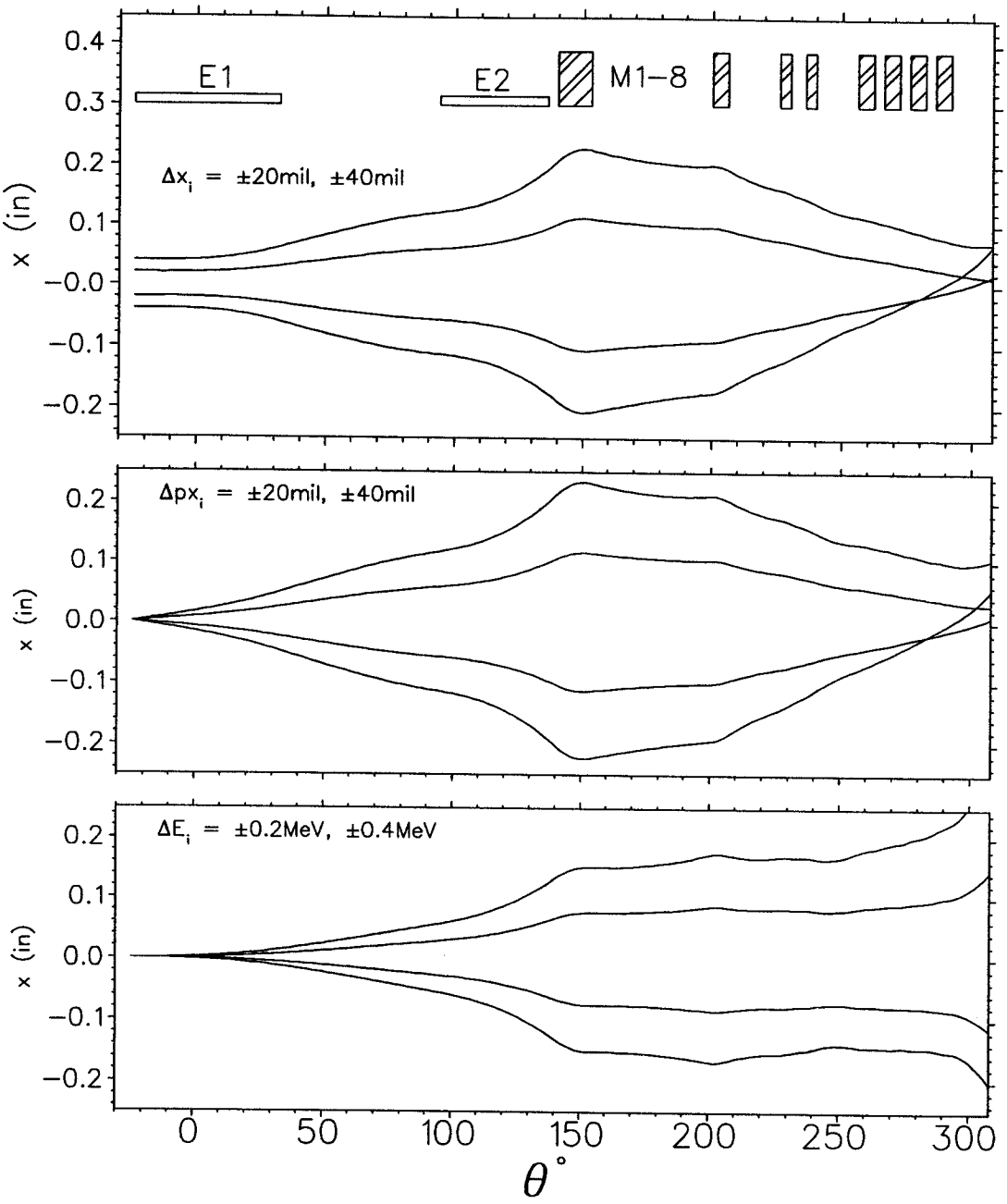

Figure 6.16: The radial phase and energy acceptance of the extraction system.

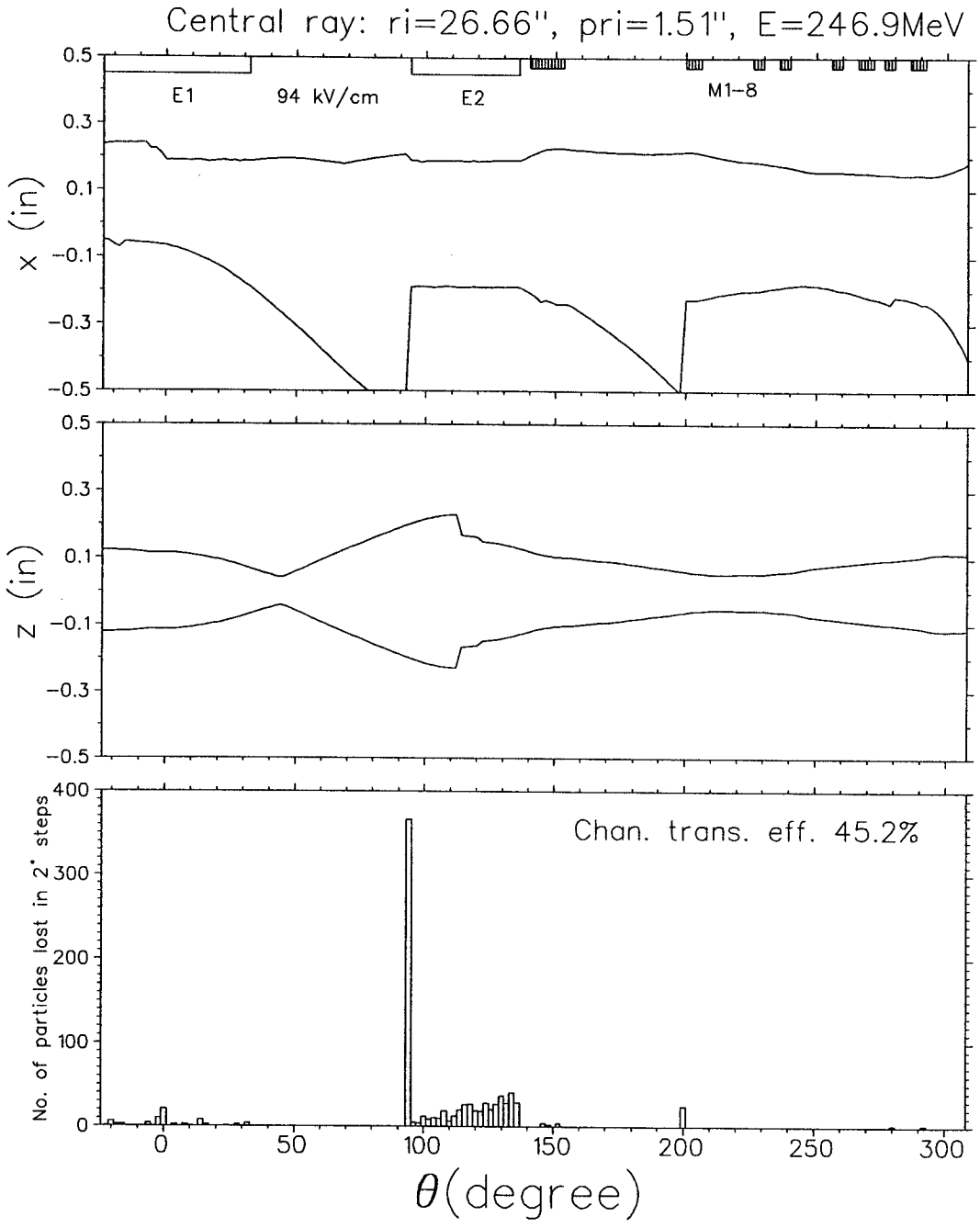

Figure 6.17: Radial and vertical envelopes of the extracted beam. Plots show $(r - r_o)$ and z vs. θ from -24^o to 308^o. The corresponding loss histogram is also depicted in the bottom.

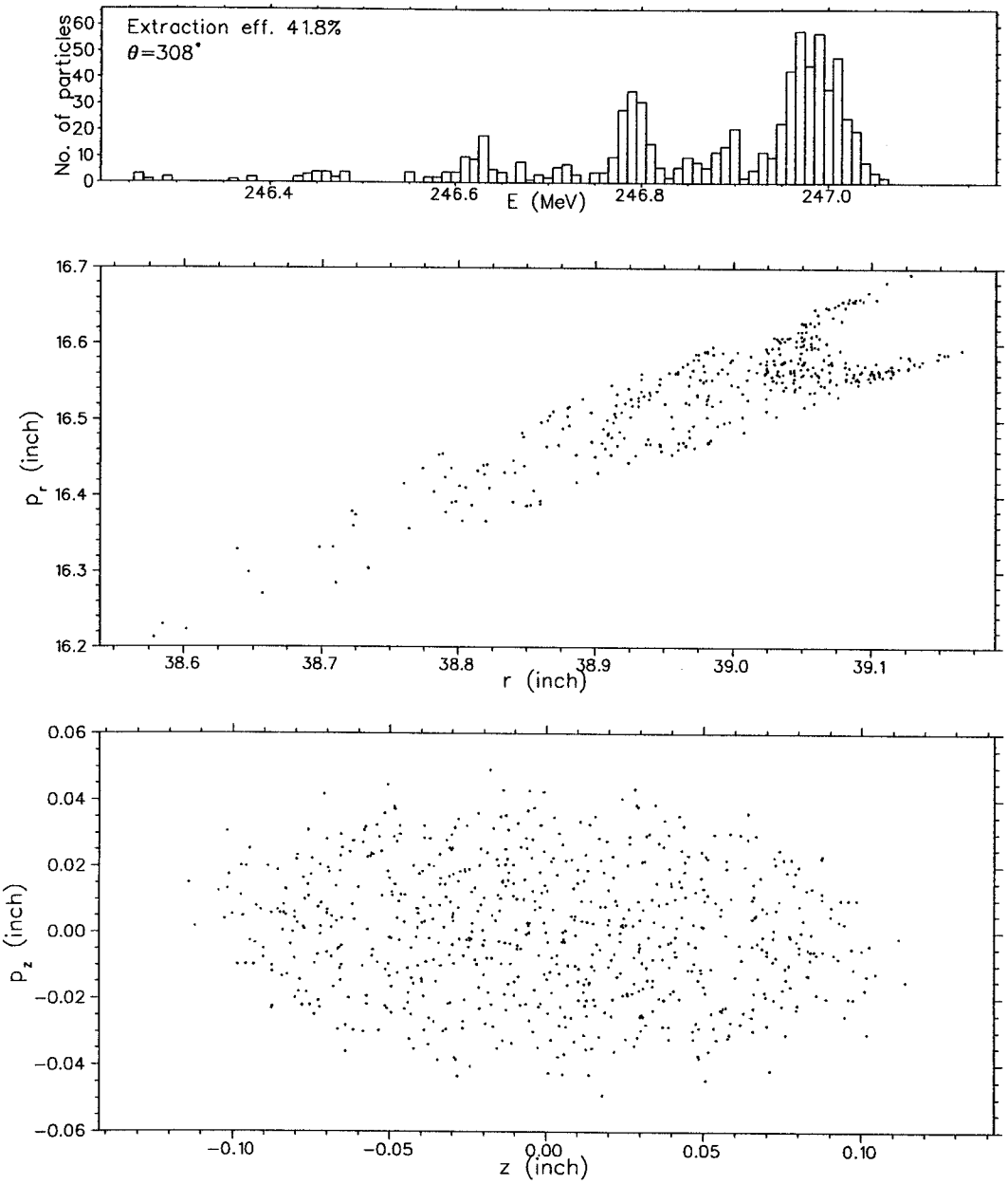

Figure 6.18: Distribution of final energies of the extracted beam (top). The corresponding radial and vertical phase space distributions are shown in the middle and bottom panels, respectively.

6.4 Performance Estimation and Summary

The extraction efficiencies for particles associated with initial betatron amplitudes x_o and z_o have been calculated and shown in Figure 6.19. The efficiency for median plane particles lies in the range of 40% and decreases rapidly with increasing betatron amplitudes due to the limited $\nu_r = 1$ resonance acceptance. Based on these contour curves, the extraction efficiency can be calculated if both the size and current density distribution of internal beam are known.

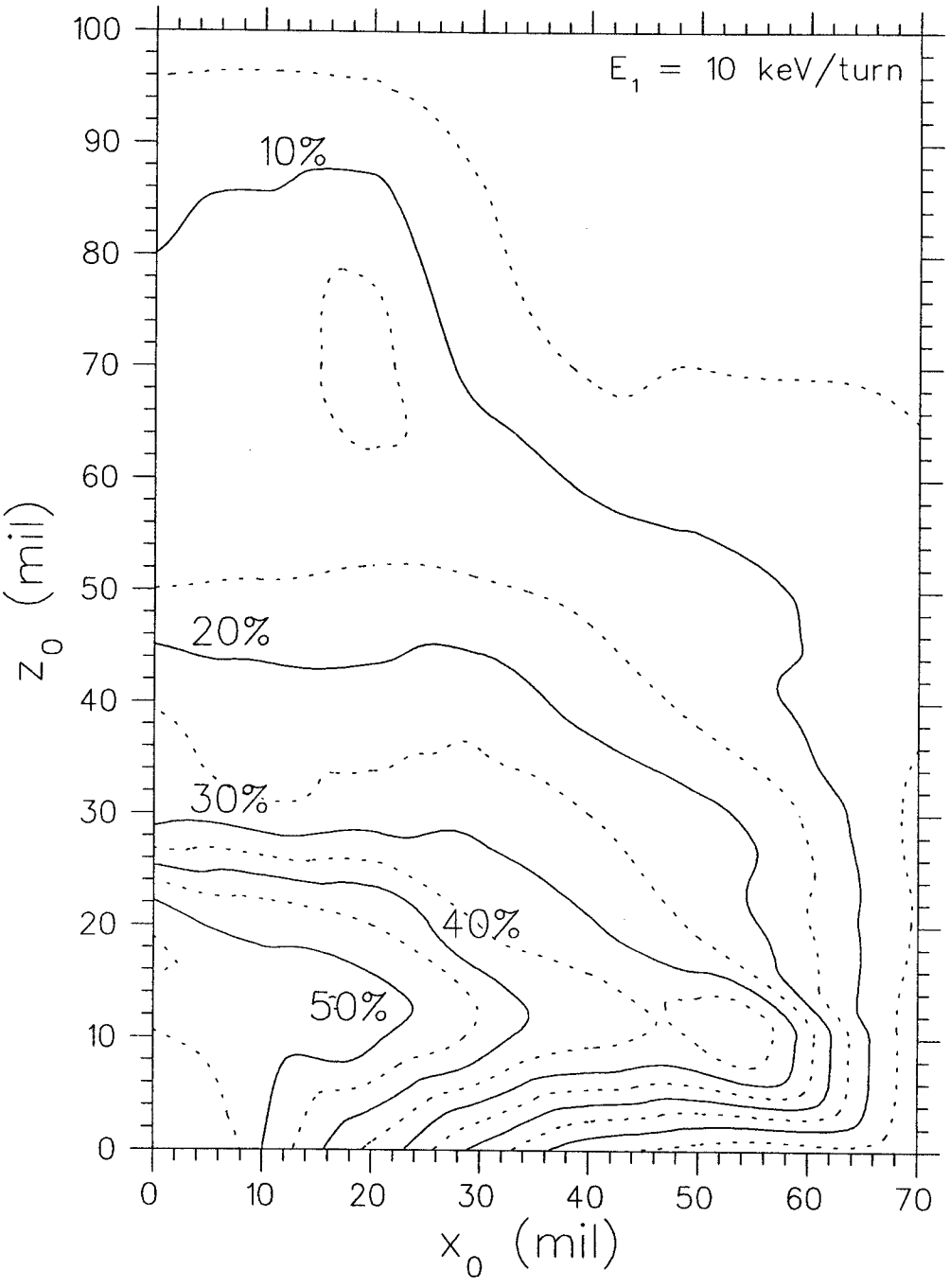

Figure 6.19: Extraction efficiencies vs. betatron oscillation amplitudes of boundary points on eigenellipses at E = 240 MeV. The number labeling beside the solid curves is the extraction efficiency. Unlabeled dash curves give extraction efficiency contour equal spacing between two adjacent labeled solid curves.

Chapter 7

$\nu_r = 1$ Excitation Extraction

7.1 Introduction

The second likely extraction system we consider is the so-called $\nu_r = 1$ excitation system; we extract the beam at the resonance $\nu_r = 1$. In this procedure, the degradation and loss of the beam associated with the resonance $\nu_r = 1$ can be avoided in comparison with the regenerative scheme in Chapter 6. But a major drawback of this method stems from the lower energy at which the beam is extracted which may require electric deflector field strengths which are impossible to achieve.

The voltage holding capability of electrostatic deflectors has long been recognized as one of the limiting factors in extracting a high energy beam from a superconducting cyclotron. In response to the demand for higher electric bending power, certain processes have been made to improve the voltage holding capability recently in our lab; 80 kV at 6 mm gap can be achieved without serious leakage [75]. In addition, a news letter from Chalk River declares that 95 kV is achieved in the presence of both r.f. power and a 3-Tesla magnetic field across a septum/anode gap of 7.5 mm [76]. Consequently, we may anticipate that 160 kV/cm at 5 mm aperture could be achieved routinely and reliably in the near future; the electric deflector field strengths implied by the calculations shown in this chapter thus seem clearly feasible.

The excitation of the $\nu_r = 1$ resonance is used to expand the turn spacing as the beam enters the first electrostatic deflector. The bump coil produces a $\cos\theta$ perturbation on the beam. As a result, it opens up a corner of the triangular stable region of the radial phase space at one of the unstable fixed points; the stability limits shrinks as the energy approaches the resonance and the beam spills out slowly along a asymptote (as exemplified further on in Figure 7.9 [42]).

7.2 Analytic Solution Concerning the $\nu_r = 3/3$ Resonance

A simplified analytical method regarding the $\nu_r = 3/3$ resonance is presented in this section. Also semi-quantitative results are derived to shed insight on beam behavior in a three-sector cyclotron at the $\nu_r = 3/3$ resonance.

For a three-sector cyclotron, the betatron motion about the stable equilibrium orbit in a perfect three-fold symmetric magnetic field can be expressed approximately as [45]

$$\frac{d^2x}{d\theta^2} + \nu_r^2 x = cx^2 cos3\theta \tag{7.1}$$

where x is the displacement from the equilibrium orbit, c is a constant characterizing the strength of the non-linear force, and the $cos3\theta$ factor arises from the three-sector periodicity of the magnetic field.

The solution to the linear Kerst-Serber equation $\frac{d^2x}{d\theta^2} + \nu_r^2 x = 0$ is $x = Asin\nu_r\theta$. Considering c as a perturbation on the linear motions, the solution to the Equation 7.1 may therefore be written as

$$x(\theta) = a(\theta) \cdot sin(\nu_r\theta + \phi(\theta)) \tag{7.2}$$

Assuming slowly varying $a(\theta)$ and $\phi(\theta)$ relative to θ, Conte and Mackay [77] show that

$$\frac{da}{d\theta} = -\frac{ca^2}{8}cos(3\phi) \tag{7.3}$$

$$\frac{d\phi}{d\theta} = \nu_r - 1 + \frac{ca}{8}sin(3\phi) \tag{7.4}$$

One trivial solution to Equations 7.3, 7.4 is $a = a_{eo} = 0$, which characterizes an "elliptical" fixed point (E.O.). For small amplitude a, the nonlinear force $(cx^2cos3\theta)$ is negligible, so that a is a constant and successive phase space orbits at one fixed azimuth will fall on an ellipse with precession frequency $\mid \nu_r - 1 \mid$.

The "unstable" fixed points occur when both $a(\theta)$ and $\phi(\theta)$ are constant. Hence, we have

$$cos(3\phi) = 0, \tag{7.5}$$

giving rise to three fixed points 120° apart ($\phi_{us} = 90°, 210°$, and 330°). In addition, the resulting radial position, a_{us} for unstable fixed points is

$$a_{us} = \frac{8 \mid \nu_r - 1 \mid}{c} \tag{7.6}$$

As summarized in Gordon's paper [45], the three unstable fixed point mark a "triangle" separatrix in radial phase space between stable "elliptical" orbits and unstable orbits, characterized by asymptotes along which orbits move in or out. A good numerical example was given in Chapter 3 (Figure 3.9).

Consider a flat bump of the form

$$\Delta B = B_1 cos\theta \tag{7.7}$$

The radial betatron equation of motion becomes

$$\frac{d^2x}{d\theta^2} + \nu_r^2 x = cx^2 cos3\theta + gcos\theta \tag{7.8}$$

where $g = (B_1/B_o) \cdot R$ measures the strength of the perturbation.

For small g, the solution of the above differential equation can be found in Laslett's paper [78]. He showed that the locations of the two relevant fixed points which lie on the $p_x = 0$ axis for $\nu_r \simeq 1$ are

$$a_{eo}(g) \simeq \frac{9g}{8(\nu_r - 1)} \tag{7.9}$$

$$a_{us}(g) \simeq \frac{8(\nu_r - 1)}{c} - \frac{9g}{8(\nu_r - 1)} \tag{7.10}$$

When these two fixed points coincide, they topologically annihilate and radial stability disappears, causing particles which had previously been in the stable region to spill out along one of the asymptotes. The stop band of the $\nu_r = 3/3$ resonance can be estimated as follows. Requiring $a_{eo}(g) = a_{us}(g)$, yields $\mid \nu_r^* - 1 \mid$; if $\mid \nu_r^* - 1 \mid \geq \mid \nu_r - 1 \mid$, the radial motion is unstable

$$\mid \nu_r^* - 1 \mid = \frac{3}{4}\sqrt{\frac{gc}{2}} \tag{7.11}$$

The $\nu_r = 3/3$ stop band in energy units can then be approximated as

$$\Delta E_{sb} = \frac{3}{2 \cdot (d\nu_r/dE)}\sqrt{\frac{cB_1R}{2B_o}} \tag{7.12}$$

7.3 Optimization of Bump Phase

As was shown by Blosser [42], quite different extraction characteristics, (i.e. "one" or "two corner opening" orientation, flow rate in phase space, deflecting strength required

to bend beam out, distortion and integrity of beam), are obtained depending on the bump angle selected.

Numerical calculations have been done to explore the relation between the bump angle and various orbit behaviors. The end behaviour of initially centered phase space orbits with first harmonic bumps at various different phases are shown in Figure 7.1 (top). The electric deflector field strength required to bend beam out versus bump phase is also given in this graph (bottom). Note the E strength is approximate due to the difficulties involving the accurate determination of which point on the asymptote is selected as the reference orbit for the extraction channels.

It seems that the 160° bump gives the best overall performance in accordance with integrity of beam and electric deflector field strength requirement.

7.4 Optimization of Bump Amplitude

Near extraction special attention has to be paid to the vertical motion. Resonances which can cause growth of the vertical amplitude in this magnetic field occur at $\nu_z = 1/2$, and at $\nu_r = 2\nu_z$.

At a half integer resonance such as $\nu_z = 1/2$, vertical stability is lost if there exists a first radial derivative of the first harmonic of the median plane magnetic field. The amplitude gain will vary as the square of the driving term. The intuitive reason for the quadratic dependence is that both the strength of the resonance and the number of turns spent in the stop band are proportional to this driving term [57].

The vertical amplitude growth associated with $\nu_z = 1/2$ stop band may be estimated by using the EO code. If we write $z = Ze^{i\nu_z\theta}$ and $\nu_z = 1/2 + i\nu^*$ in the stop

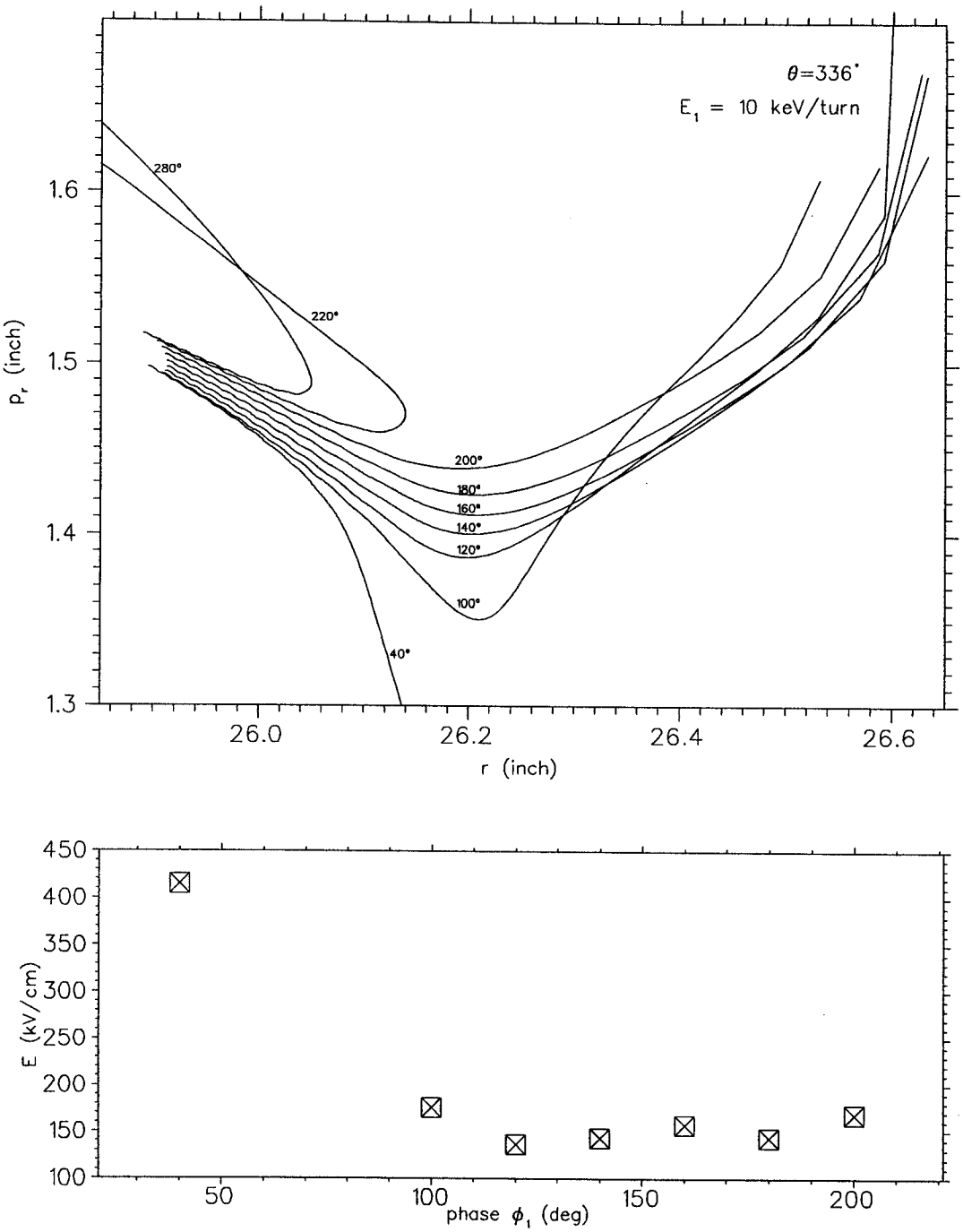

Figure 7.1: Top: radial phase space plot for the accelerating orbits at $\theta = 336^0$, initially centered at E=240 MeV, with 1.2 gauss first harmonic bump at several different azimuths. The number besides the curve is the bump phase ϕ_1 in degree. Bottom: the approximated electric deflector field strength required to bend beam out vs. bump phase.

band, then the amplitude growth $Z_{final}/Z_{initial}$ is given by

$$\frac{Z_f}{Z_i} = e^{\int \nu^* \cdot d\theta}$$

$$\simeq \cdots\cdots \times e^{\nu^*(E-2\Delta E)\cdot 2\pi \cdot \frac{\Delta E}{E_1}} \times e^{\nu^*(E-\Delta E)\cdot 2\pi \cdot \frac{\Delta E}{E_1}} \times e^{\nu^*(E)\cdot 2\pi \cdot \frac{\Delta E}{E_1}}$$

$$\times e^{\nu^*(E+\Delta E)\cdot 2\pi \cdot \frac{\Delta E}{E_1}} \times e^{\nu^*(E+2\Delta E)\cdot 2\pi \cdot \frac{\Delta E}{E_1}} \times \cdots\cdots$$

$$\equiv \prod_{stopband} e^{\nu^*(E)\cdot 2\pi \cdot \frac{\Delta E}{E_1}} \tag{7.13}$$

where ν^* is the imaginary part of the vertical focusing frequency and E_1 is energy gain per turn.

The axial amplitude growth Z_f/Z_i as a function of energy gain per turn for centered orbits with five different first harmonic bump amplitudes, computed using the EO code data and Equation 7.13, is shown in Figure 7.2.

The NSCL linear Z code can also be used to investigate the effects of the resonance $\nu_z = 1/2$ on vertical amplitude growth. Since this code only couples the radial motion into the axial motion, not vice versa, the $\nu_z = 1/2$ resonance effect will be isolated if we start the computations on equilibrium orbits. The evolution of vertical ellipses and corresponding eigenellipses at various energies are shown in Figure 7.3. We find that the accelerating ellipses are tilted and stretched due to the resonance crossing.

The $\nu_r = 2\nu_z$ resonance (the Walkinshaw resonance) occurs just after the $\nu_z = 1/2$ resonance and shortly before the $\nu_r = 1$ resonance in this magnetic field. It is well known that the effect of the Walkinshaw resonance depends strongly on the beam quality and on the energy gain per turn [62].

The Z^4 orbit code was used to study the evolution of both radial and axial ellipses associated with $B_1 = 1.2$ gauss and $E_1 = 10$ keV/turn in the vicinity of the resonances $\nu_z = 1/2$ (240.7 MeV) and $\nu_r = 2\nu_z$ (241.2 MeV); results are plotted in Figure 7.4. Non-linear features of the resonances (amplitude dependence) and some common characteristics (distortion, stretching and amplitude growth) are clearly indicated.

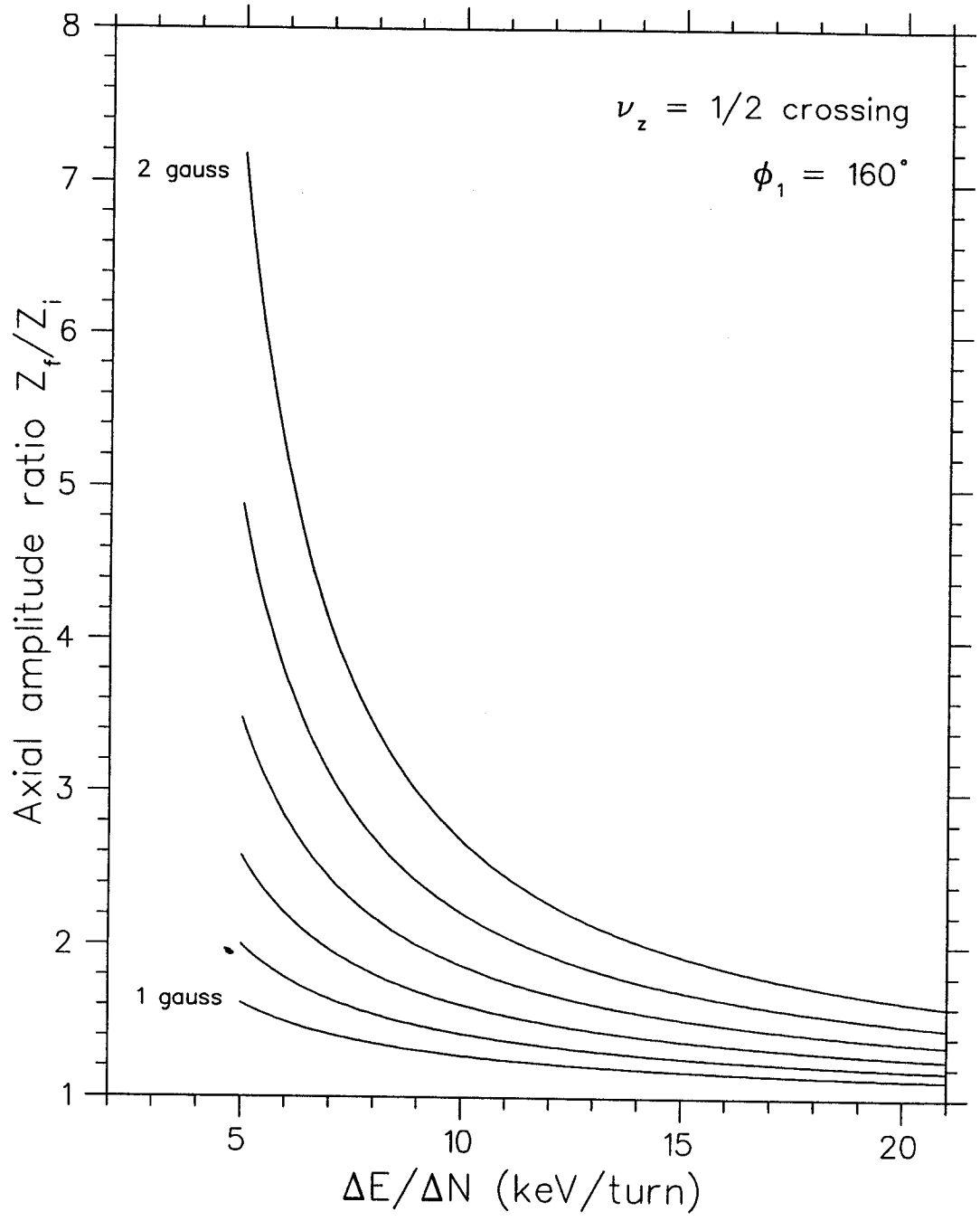

Figure 7.2: Plot of axial amplitude growth induced by the $\nu_z = 1/2$ resonance traversal vs. energy gain per turn, estimated by the EO code for centered orbits. The number besides the curve is the amplitude of the first harmonic bump in gauss unit. Unlabeled curves are equally spaced in 0.2 gauss steps between labeled curves.

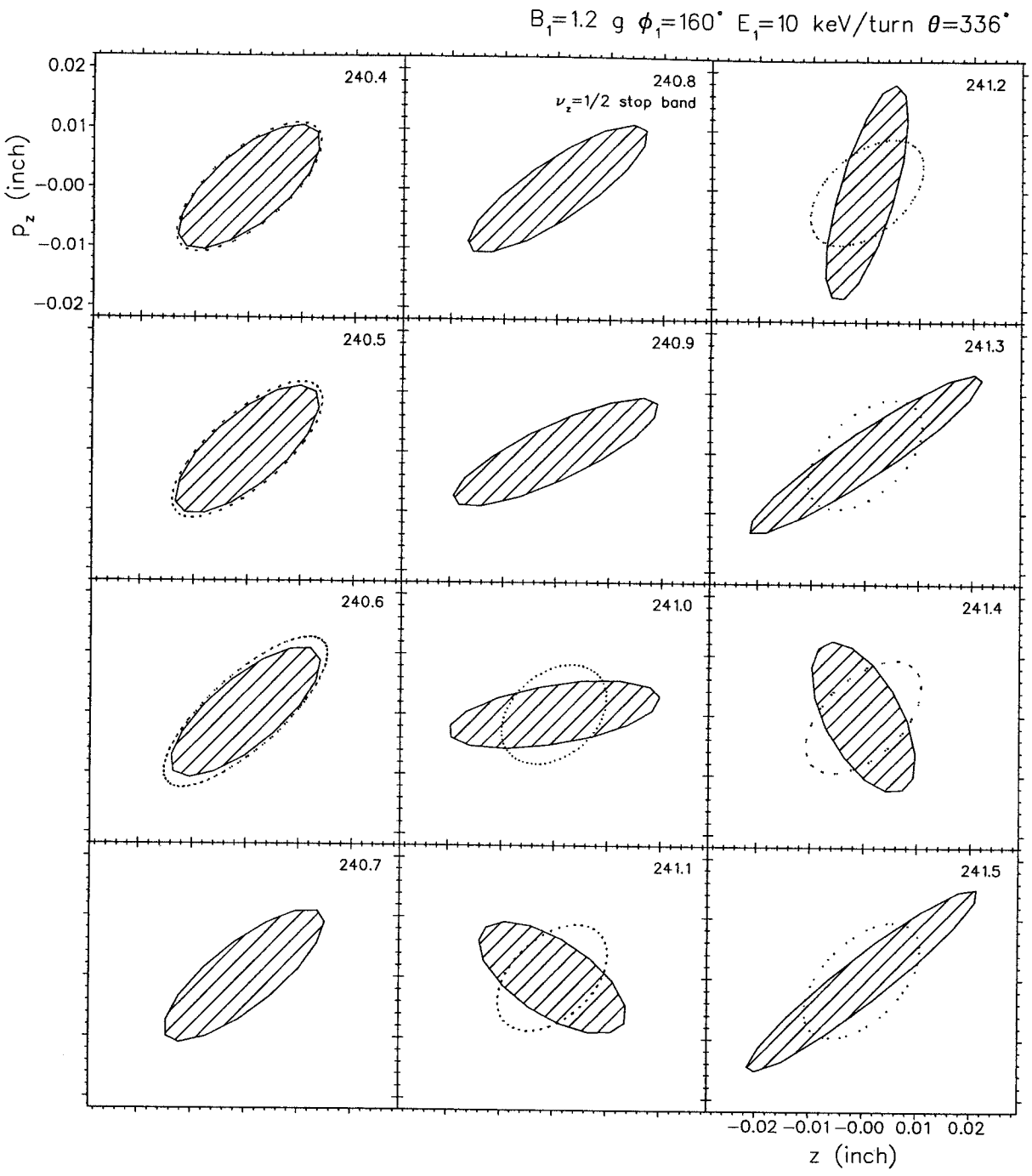

Figure 7.3: Plot of evolution of z ellipses (solid curves) showing the resonance $\nu_z = 1/2$ effect by using linear Z code. The dotted curves are the eigenellipses at each energy.

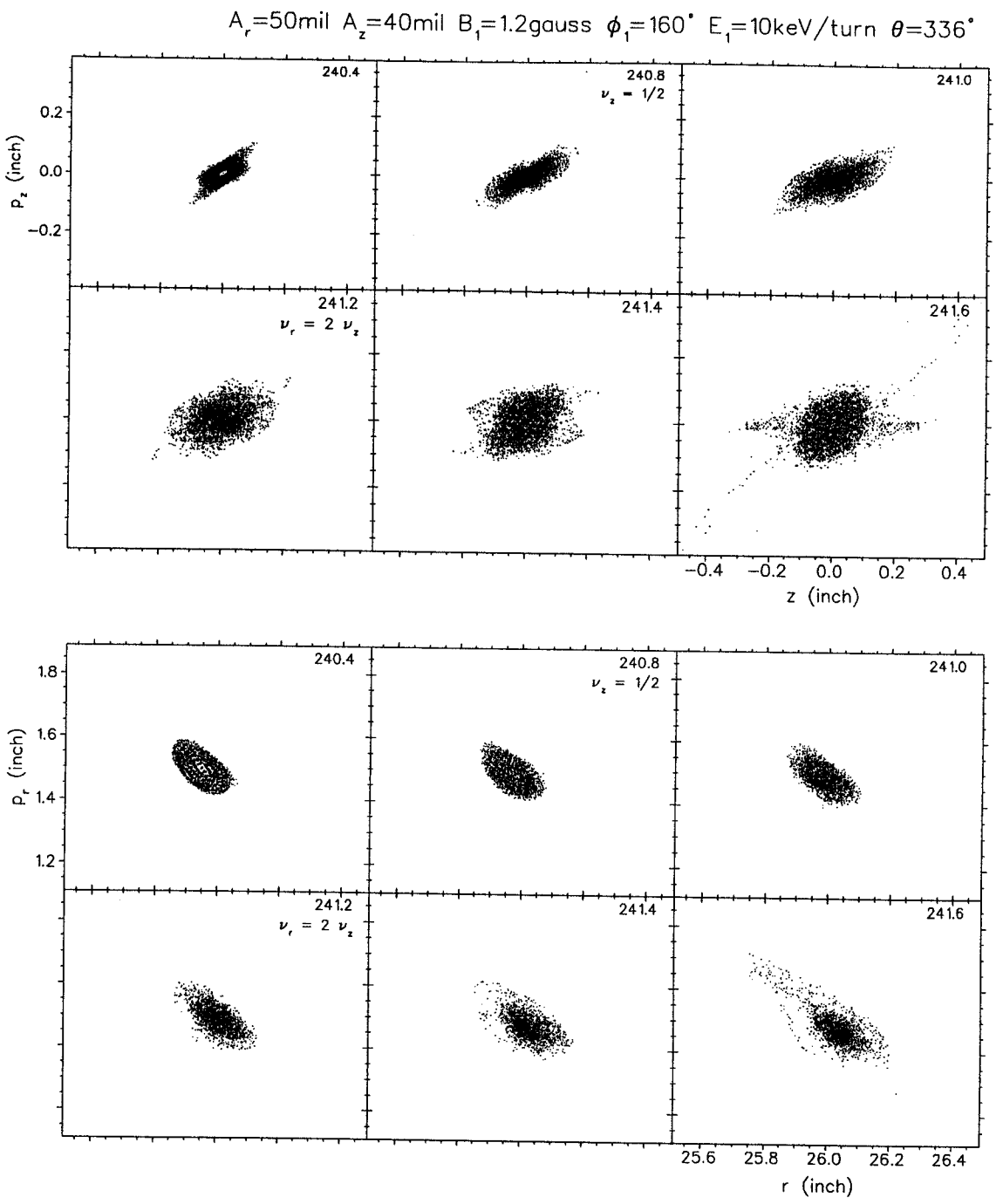

Figure 7.4: Evolution of accelerating ellipses in the vicinity of resonances $\nu_z = 1/2$ and $\nu_r = 2\nu_z$. The numerical labeling is the energy in MeV.

A stronger (1.7 gauss) bump was also studied and Figure 7.5 compares these results with the 1.2 gauss case by showing the final outward flowing asymptote for each bump for two different E_1 values.

The turn spacing at the head of the septum and required electric deflector field strength as function of septum position and bump amplitude are shown in Figure 7.6. The stronger bump gives lower extraction energy, increases phase space flow rate, decreases the electric deflector field strength and moves the asymptote further out in radius. The weaker bump does the opposite. But the stronger bump is not unreservedly a desirable feature in that vertical instability is inevitably induced by a stronger bump. The beam axial envelope vs. different bump amplitudes is shown in Figure 7.7. It shows that for $B_1 > 1.2$ gauss, vertical loss will occur caused by the resonances $\nu_z = 1/2$ and $\nu_r = 2\nu_z$.

The results in Figures 7.6 and 7.7 show clearly that the turn separation, vertical growth, needed electric deflector field strength, and distortions are strongly correlated in the $\nu_r = 1$ extraction process. To quantitatively evaluate the tradeoffs implied by these several considerations, additional acceleration studies have been carried out which are not presented in details here. These more extensive orbit calculations show that the optimal bump corresponding to the conditions of $E_1 = 10$ keV/turn, $A_r = 30$ mil, $A_z = 20$ mil, is $B_1 = 1.2$ gauss, and $\phi_1 = 160^0$.

7.5 Summary of Final Calculations of $\nu_r = 1$ System

Parameters of extraction elements are shown in Table 7.1.

The radial and axial focusing frequencies as a function of energy in the extraction region are given in Figure 7.8. At the $\nu_r = 1$ resonance the 1.2 gauss bump opens a

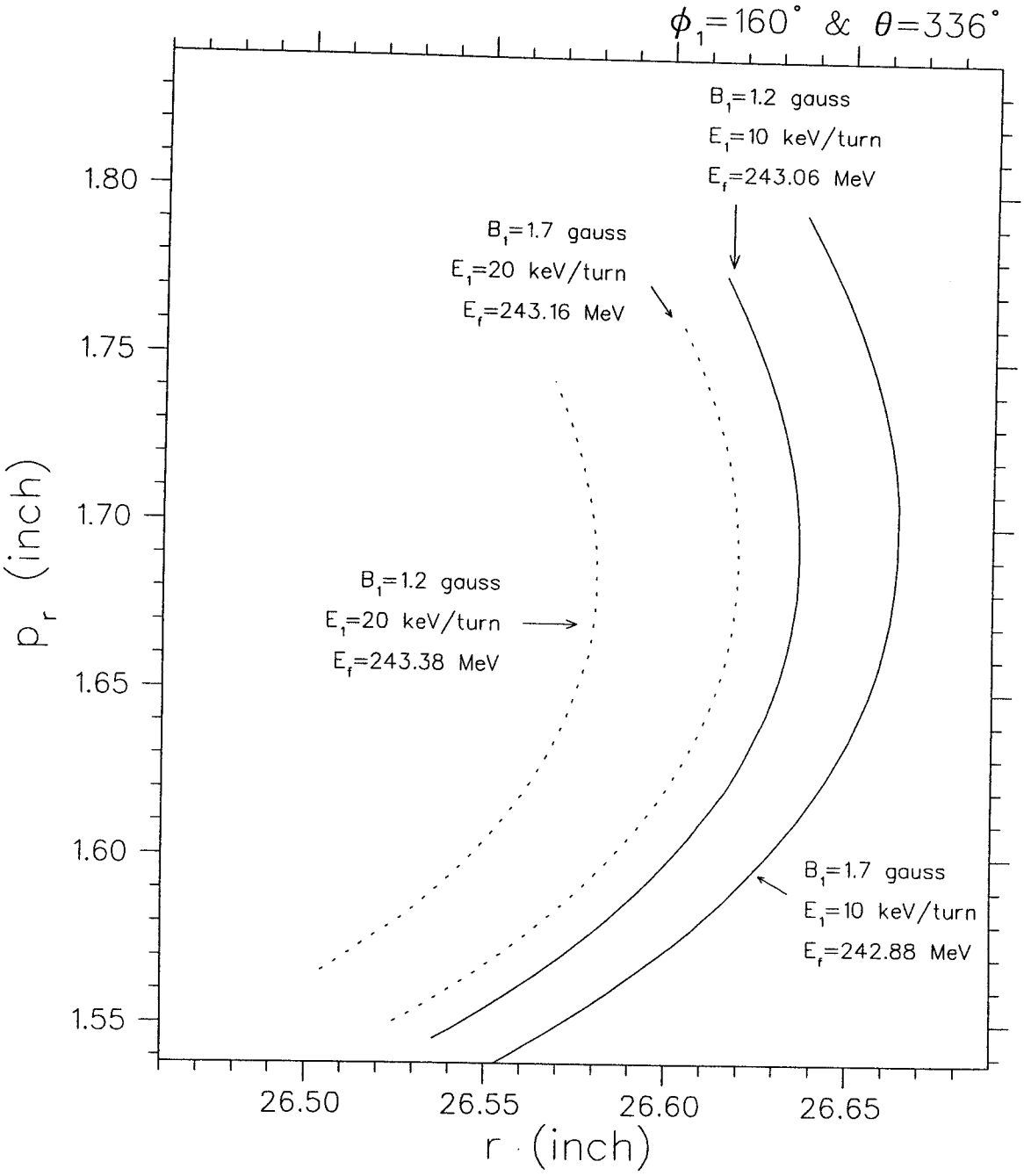

Figure 7.5: Asymptotes in the $\nu_r = 1$ excitation extraction for various conditions.

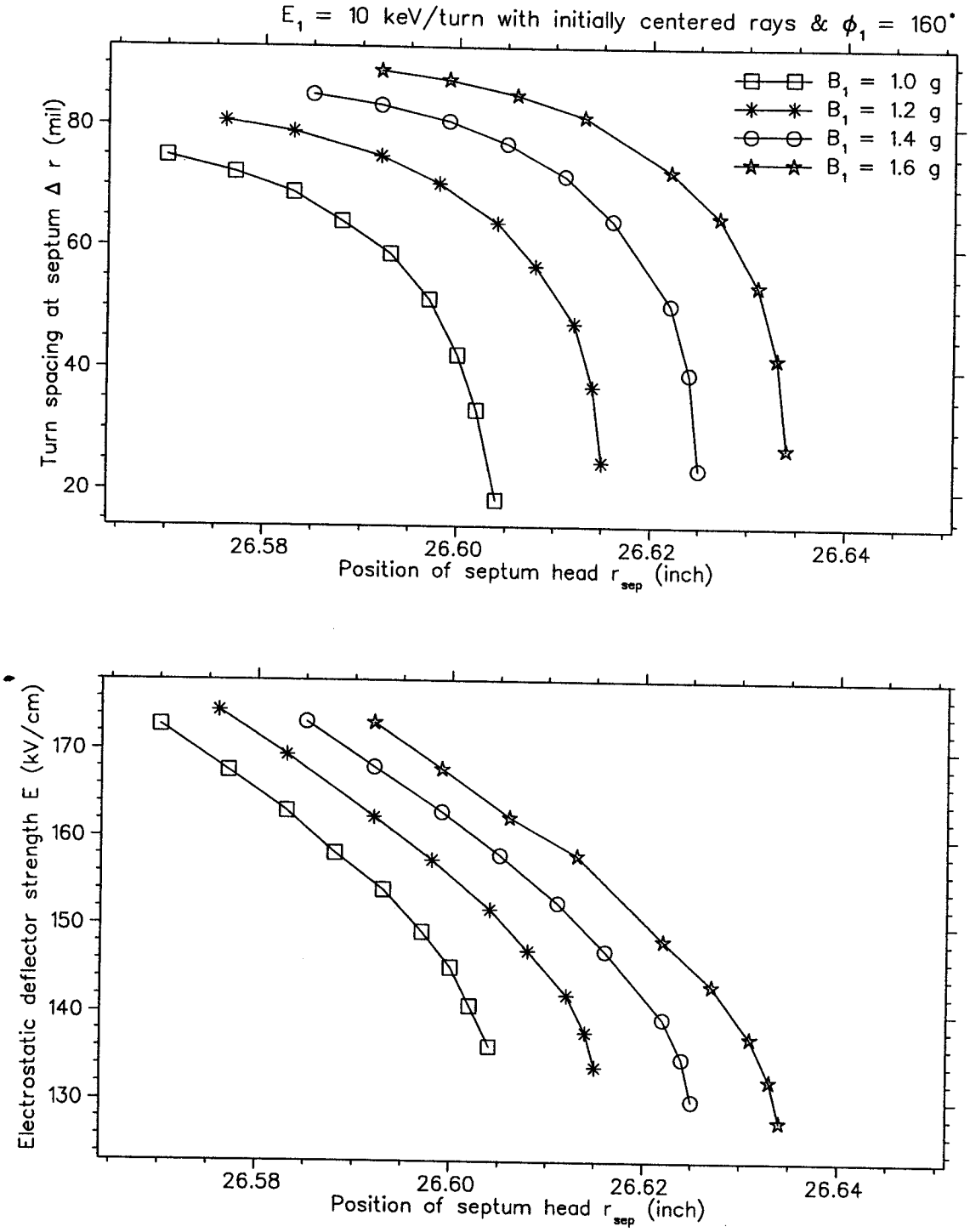

Figure 7.6: Plots showing the turn spacing at the head of the septum (top) and the electric deflector field strength required to extract the beam (bottom) as function of septum position and bump amplitude.

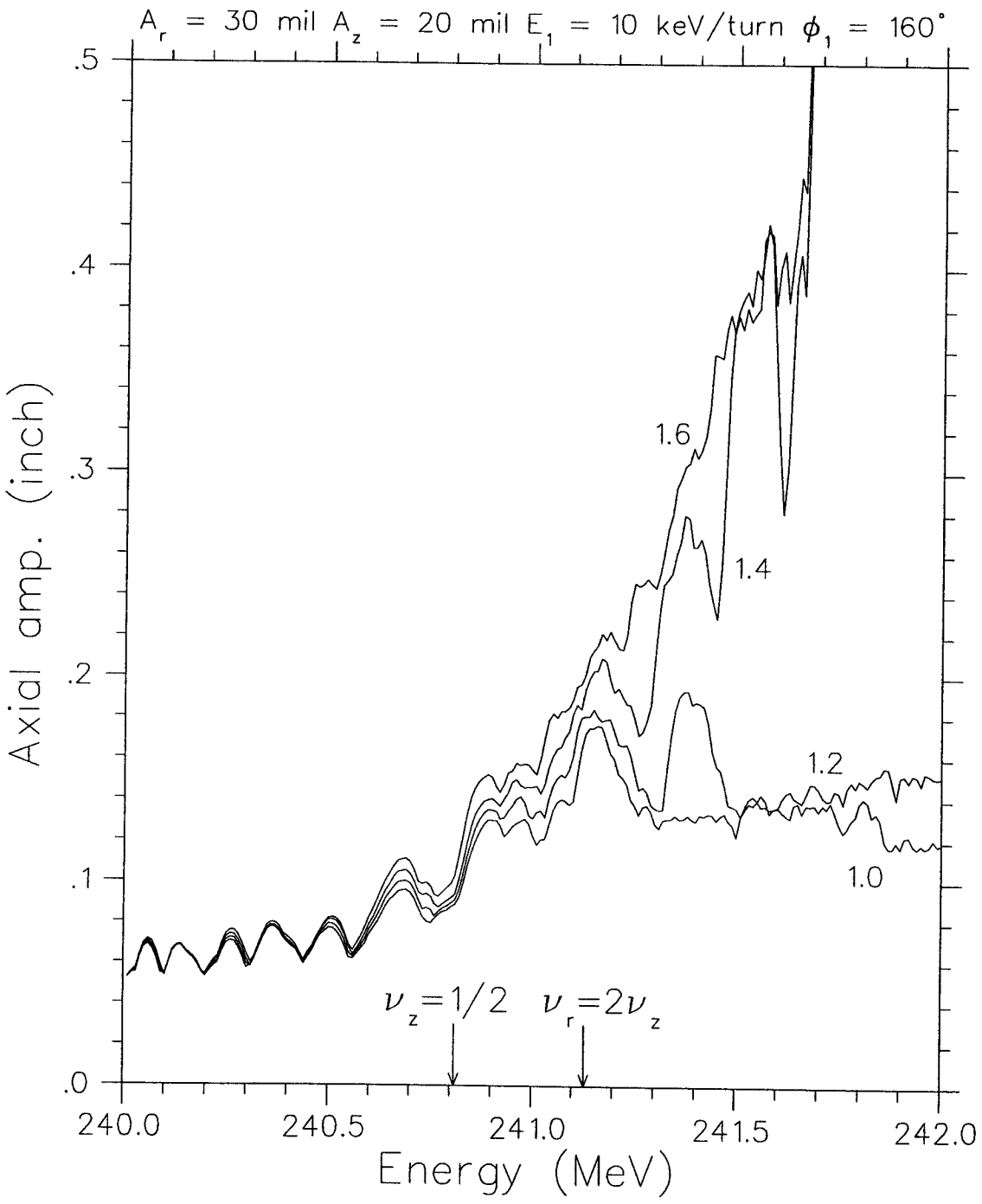

Figure 7.7: Axial envelop vs. energy showing the effect of bump amplitude on beam behavior for the $\nu_z = 1/2$, $\nu_r = 2\nu_z$ resonance crossing.

Table 7.1: Extraction element parameters ($B_1 = 1.2$ gauss)

	Θ_i (deg)	Θ_f (deg)	R_i (inch)	R_f (inch)	M.A. (inch)	E (kv/cm)	ΔB (kg)	$\partial B/\partial x$ (kg/inch)	R_c (inch)
E1	-24	32	26.64	27.44	0.2	161			
E2	94	136	27.75	28.14	0.2	161			
R	49	61							
M1	140	153	28.16	28.23	0.5		1.2	8.8	
M2	200	206	28.70	28.80	0.5		1.2	8.8	
M3	226	232	29.22	29.37	0.5		1.2	8.8	
M4	236	242	29.49	29.69	0.5		1.2	8.8	
M5	256	262	30.27	30.59	0.5		1.2	8.8	
M6	266	272	30.85	31.30	0.5		1.2	8.8	
M7	276	282	31.67	32.33	0.5		1.2	8.8	
M8	286	292	32.88	33.92	0.5		1.2	8.8	
C1	320	334							28.2
C2	46	58							29.6

stop band of 1.14 MeV width where no equilibrium orbit exists.

Figure 7.9 shows an initial 50 mil betatron eigenellipse (the cross hatched area) accelerated into the resonance, with non-accelerated orbits superimposed at each energy to show the characteristics of the static phase space. The mid-plane motion is seen to be excellent - clean turn separation and 100% beam capture into the desired outward flowing asymptote.

The beam axial envelope vs. energy, the energy density distribution for those which successfully enter the channel, and (r, p_r), (z, p_z) spectrums at the entrance of the deflector are given in Figure 7.10 for the conditions $A_r = 30$ mil, $A_z = 20$ mil, $B_1 = 1.2$ gauss, $\phi_1 = 160°$, $E_1 = 10$ keV/turn and $r_{sep} = 26.050''$. The large axial growth at E $\simeq$ 242.4 MeV is due to the beam being off center, but a channel entry efficiency of 83.3% is never-the-less achieved.

Transmission loss thru the the extraction system is primarily due to the limited

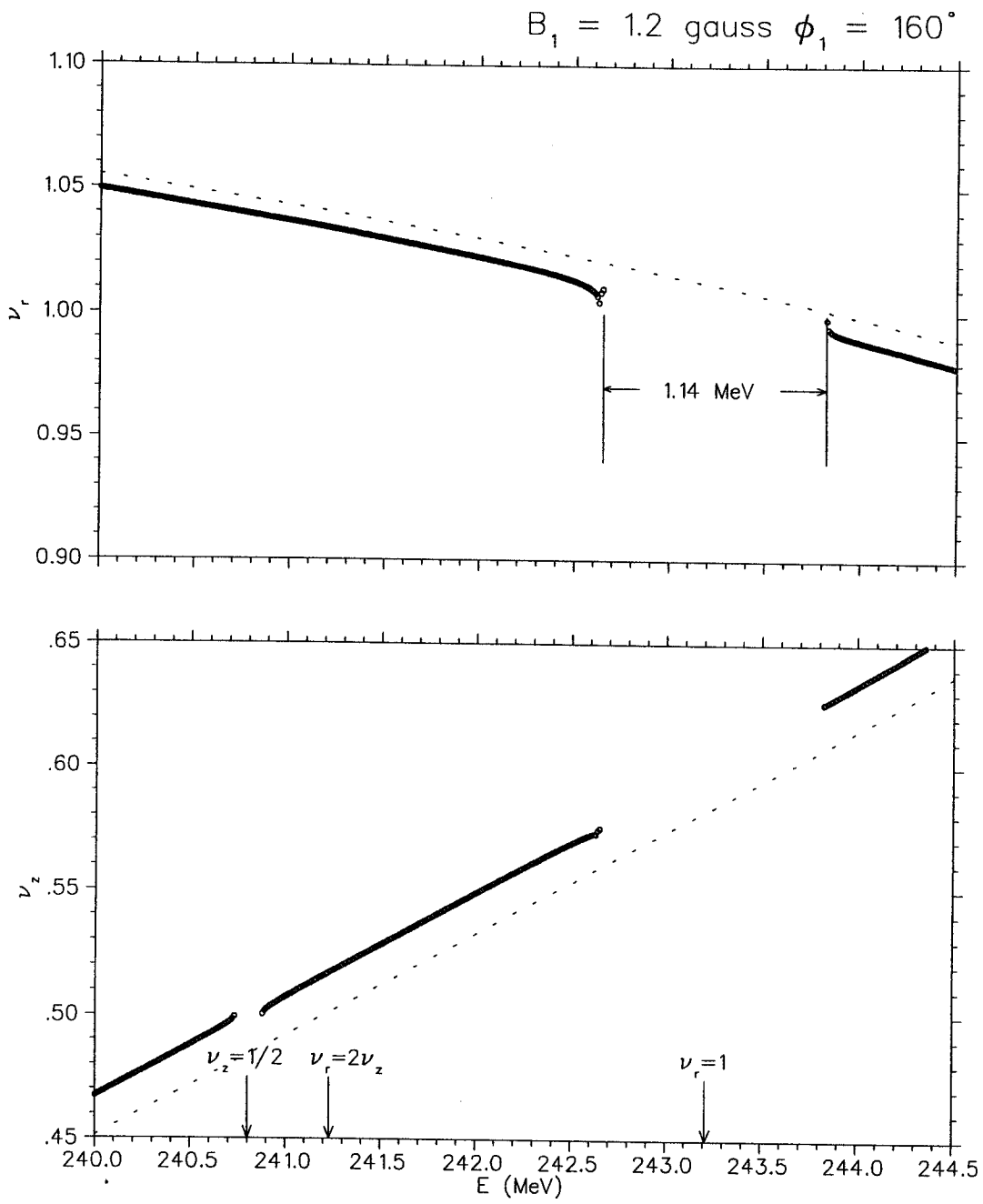

Figure 7.8: The focusing frequencies in the $\nu_r = 1$ excitation extraction field are plotted vs. energy (heavy solid curves). As a reference, the focusing frequencies associated with the perfect 120^0 field map are also depicted (dotted curves).

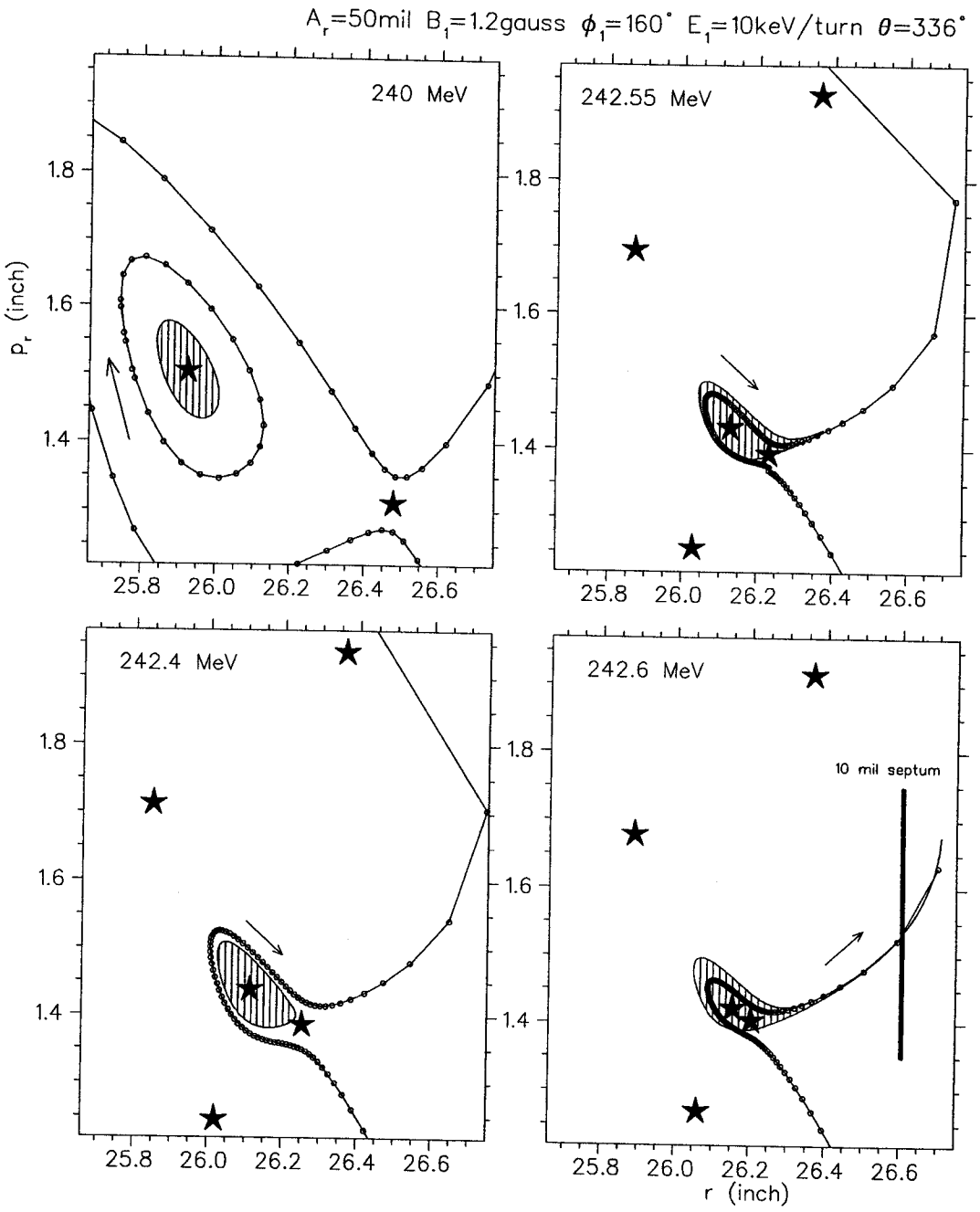

Figure 7.9: Radial phase plots showing the behavior of acceleration runs with a bump $B_1 = 1.2$ gauss, $\phi_1 = 160°$. The fixed points are represented by stars, the static flow direction by arrows, and the beam by hatched areas.

aperture (5mm) of electrostatic deflector and the radially defocusing force associated with rapid edge field fall-off. Figure 7.11 gives the half beam width measured from the center of the beam, the beam loss histogram in 2^o steps along the extraction path, the distribution of final energies and $(r,\ p_r)$, $(z,\ p_z)$ spectrums at $\theta = 308^o$ where particles go off the magnetic field. The resulting channel transmission efficiency and total extraction efficiency are 21.4% and 17.8%, respectively.

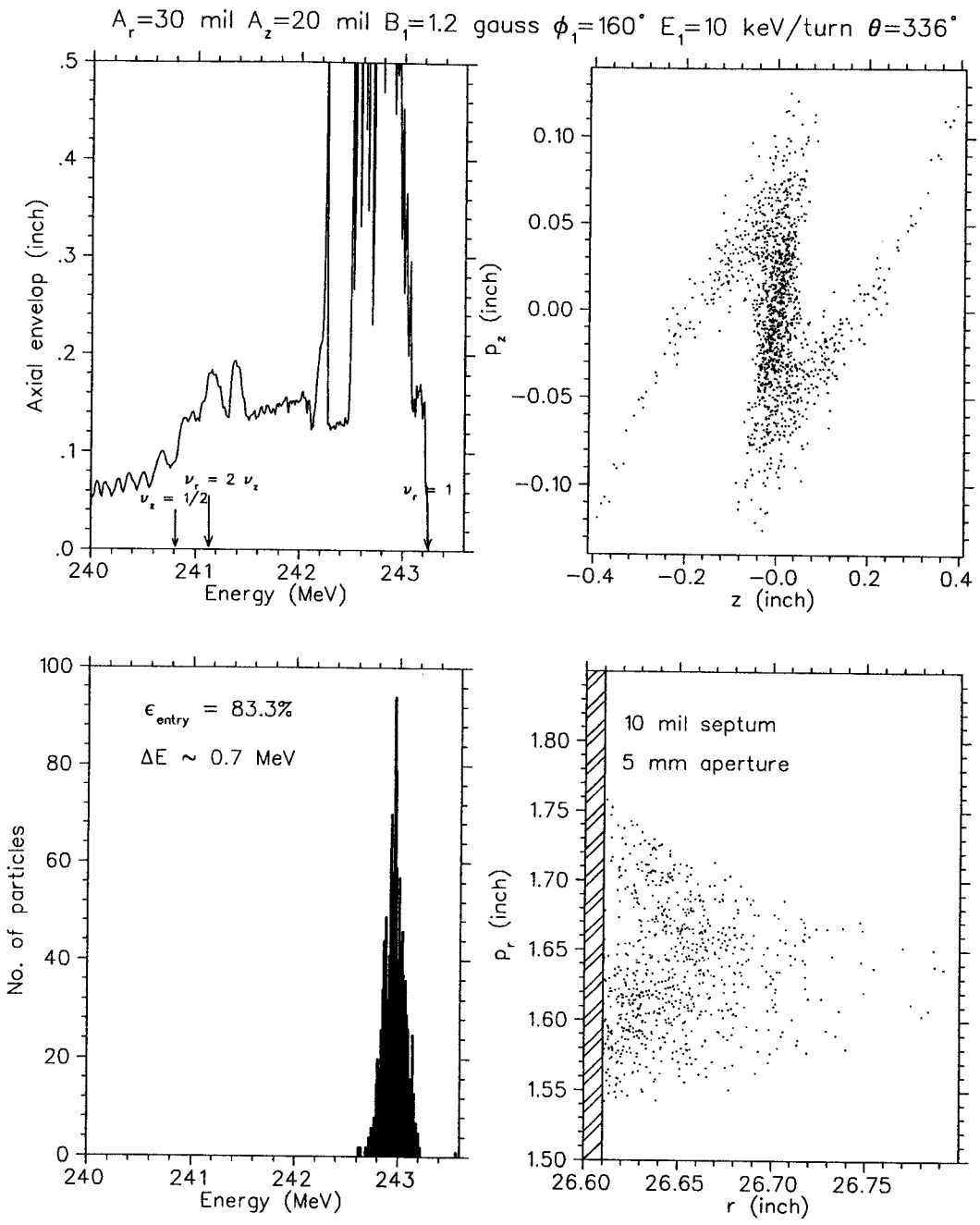

Figure 7.10: Features of the $\nu_r = 1$ extraction system computed with the Z^4 code. Left top: beam axial envelop vs. energy showing a acceptably vertical confinement through the whole extraction process. Left bottom, right top, right bottom: distribution of energies, radial and vertical phase spectrums for those which enter the deflector at the entrance of the extraction channel.

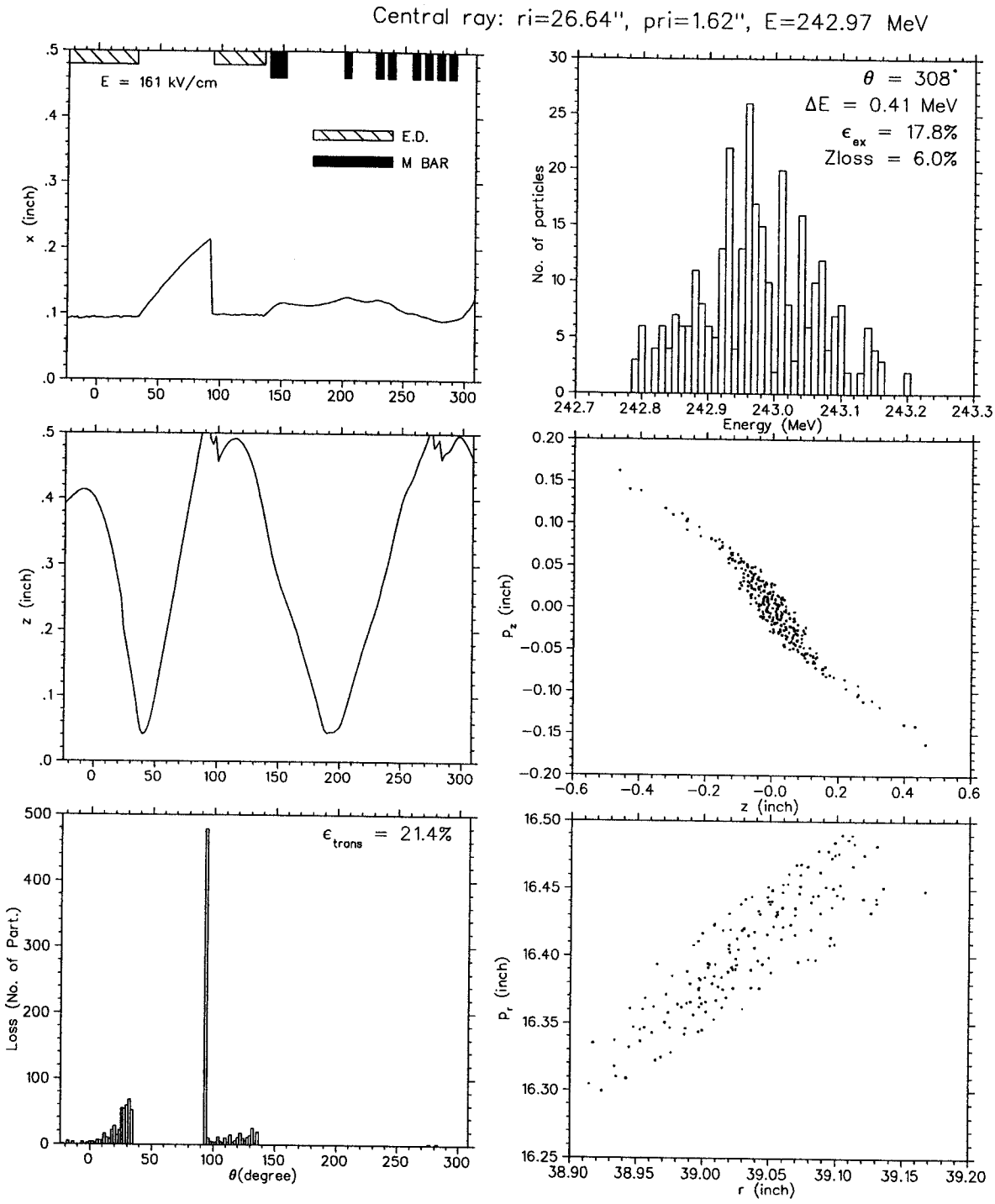

Figure 7.11: Left: the beam half width measured from the beam center and loss histogram in 2^o steps vs. θ along the extraction path. Right top: distribution of final energies. Right middle, bottom : radial and vertical phase spectrums at $\theta = 308^o$.

Chapter 8

Precessional Extraction

Compared to $\nu_r = 1$ excitation extraction considered in Chapter 7, precessional extraction, denoted PE, is the standard method used in most isochronous cyclotrons, and provides larger extraction radii, thus higher energies of the extracted beam, and the deflecting power of extraction system required is probably lower (p_r dependence). However, one difficulty of the PE is the beam loss and degradation, when passing the resonances. In addition, the turn separation from PE may not be sufficient to effectively clear the septum in such a high magnetic field synchrocyclotron.

8.1 Turn Spacing from Acceleration

The relativistic relation gives the total energy E_t in terms of rest mass m_o and particle momentum p as follows

$$E_t^2 = m_o^2 c^4 + p^2 c^2 \tag{8.1}$$

Totally differentiating the both side of Equation 8.1, after some steps, we get

$$\frac{dp}{p} = \frac{E_t^2}{p^2 c^2}\frac{dE_t}{E_t} = \frac{\gamma^2}{\gamma+1}\frac{dE_t}{E_k} \equiv \frac{\gamma^2}{\gamma+1}\frac{dE}{E} \tag{8.2}$$

where E_k, denoted as E for simplicity, is the kinetic energy of particle.

Using $p = qrB$ and assuming an axially symmetric magnetic field, $dB = \frac{B}{r}kdr$, and $\nu_r^2 = 1 + k$, which after some simple calculation, yields

$$\frac{dp}{p} = \nu_r^2 \frac{dr}{r} \tag{8.3}$$

Substituting the above expression for $\frac{dp}{p}$ and $\frac{dE}{E} = \frac{dE}{dn}\frac{dn}{E} = E_1\frac{dn}{E}$ into Equation 8.2, we obtain the formula for radius increase per turn due to acceleration, namely,

$$\frac{dr}{dn}(accel.) = r \times \frac{E_1}{E} \times \frac{\gamma^2}{\gamma + 1} \times \frac{1}{\nu_r^2} \tag{8.4}$$

Equation 8.4 immediately gives a simple idea about how to increase the radial gain per turn by "brute force" acceleration in order to get a high extraction efficiency:

- Build machines with a large average radius, i.e., a small magnetic field.
- Make the energy gain per turn, E_1, as high as possible.
- Accelerate the beam into the fringe field, where ν_r drops, i.e. the field fall-off region.

Unfortunately, brute force acceleration is generally very expensive and in addition can not alone guarantee high extraction efficiency. Several other methods can be used to enhance the turn spacing at the extraction radii, one of which is the precessional extraction mechanism, pioneered in the MSU K50 cyclotron [43]. A small field perturbation having an azimuthal first harmonic component is used in this method to induce a coherent precession of the desired amplitude as the beam accelerates through this resonance, and this radius gain periodically, when the precession is at the right phase, adds to the acceleration radius gain and increases extraction efficiency.

8.2 Turn Spacing from Orbit Precession

Recall Equation 4.11, the $\nu_r = 1$ resonance crossing produces a coherent amplitude ΔR

$$\Delta R = \pi \times R \times \frac{B_1}{B_o} \times \left(E_1 \cdot \frac{d\nu_r}{dE} \right)^{\frac{-1}{2}} \tag{8.5}$$

After the resonance, the beam precesses with the frequency $|\nu_r - 1|$ around its equilibrium position. This "coherent amplitude" is used to enhance the radius gain per turn up to a limit set by the radial difference between two successive precession cycles. (It is sometimes useful to use less precession than the limiting value in order to reduce the beam axial loss associated with the beam off-center.) As a result of this precession, post-resonance acceleration gives the radial separation needed to clear the septum.

Considering this more quantitatively, the maximum turn separation between two successive precession cycles, i.e., the maximum beam to beam separation at the head of septum, is approximated by

$$\frac{dR}{dn}(precession) = \frac{dR}{dn}(accel.) \times \frac{1}{|\nu_r - 1|} \tag{8.6}$$

The top and middle panels, respectively, of Figure 8.1 show dR/dn (accel.) and dR/dn (precession) calculated by EO code vs. energy. The electric deflector field strength required to extract the beam vs. final energy is also shown in this graph (bottom).

The value dR/dn (precession) is too small to guarantee a good extraction for synchrocyclotrons due to the negligible acceleration effect, as can be seen from Figure 8.1. In addition, we have to extract the beam at energies higher than 249 MeV for the reason of reasonable electric deflector field strength ($E \leq 160$ kV/cm) if the PE is used.

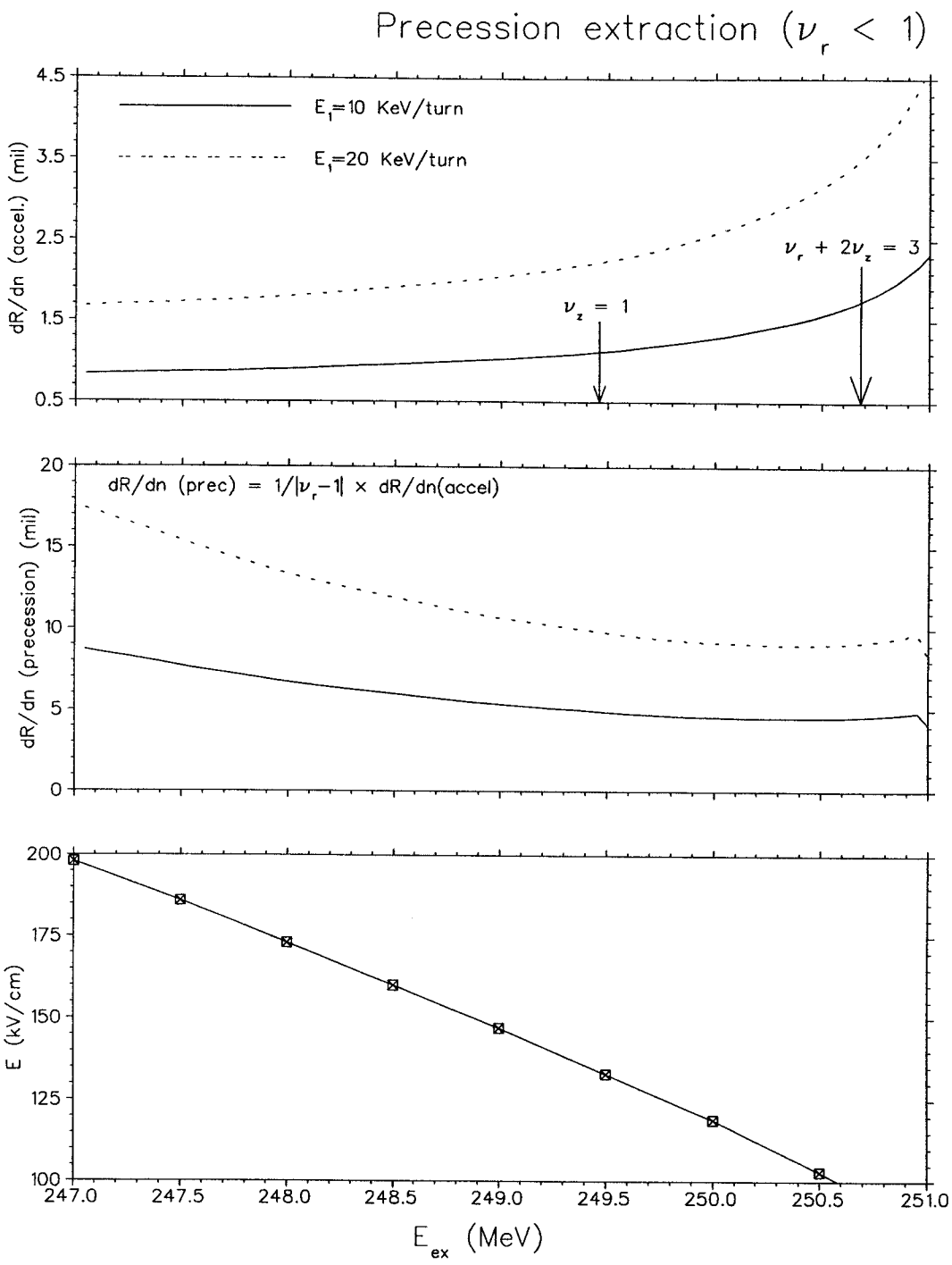

Figure 8.1: Top: dR/dn (accel.) vs. energy. Middle: dR/dn (precession) vs. energy. Bottom: required electric deflector field strength vs. final energy.

Table 8.1: The resonances in the precession extraction field.

Resonance	Driven by	Occurs at (MeV)
$\nu_z = \frac{1}{2}$	$\frac{\partial B_1}{\partial r}$	240.45 - 241.71
$\nu_r = 2\nu_z$	field derivatives & amplitude	241.00
$\nu_r = 1$	B_1	242.90 - 243.49
$\nu_z = 1$	B_1	249.23 - 249.68
$\nu_r + 2\nu_z = 3$	field derivatives & amplitude	250.68

An example of the PE mechanism is given in Figure 8.2, in which the central ray orbits and radial beam spots at various energies are plotted. Assumptions were: the 10 mil betatron eigenellipse consists of 0.5 mil by 0.5 mil grids and starts at E = 240 MeV with E_1 = 20 keV/turn. Particles striking an aperture limit or entering the deflector are removed from the calculations. As indicated in this graph, the beam is characterised by amplitude-dependent distortions after accelerating through the $\nu_r = 1$ resonance due to the residual field imperfections at the $\nu_r = 1$ radius. Second, no clean beam separation is achieved at the septum entrance simply because the radius gain per turn is too small.

8.3 Performance Calculations

The important resonances encountered in the PE system are listed in Table 8.1. The beam is proposed to be extracted at about E = 249 MeV to avoid beam loss corresponding to the resonances at $\nu_z = 1$ and $\nu_r + 2\nu_z = 3$.

Parameters of the extraction elements are shown in Table 8.2. A one mil electrostatic deflector septum is used in this system to increase the channel entry rate, thus increasing the extraction efficiency.

The combined r and z accelerated orbit runs using Z^4 are summarized in Figure 8.3

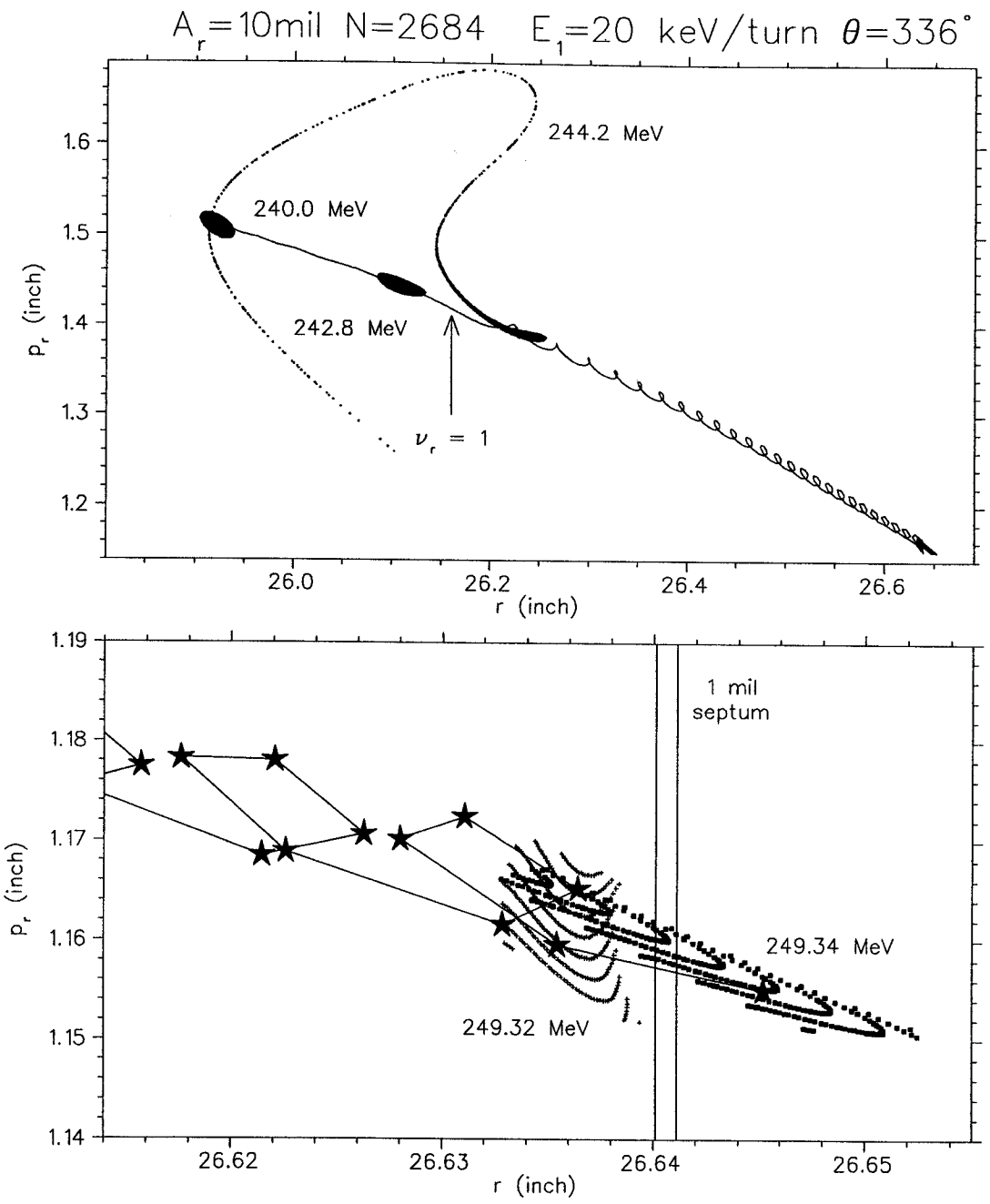

Figure 8.2: Central ray orbits and beam spots at various energies illustrates the effect of $\nu_r = 1$ resonance crossing and the concept of precession extraction (a net $B_1 \sim 0.1$ gauss bump used).

Table 8.2: Extraction element parameters

	Θ_i (deg)	Θ_f (deg)	R_i (inch)	R_f (inch)	M.A. (inch)	E (kv/cm)	ΔB (kg)	$\partial B/\partial x$ (kg/inch)	R_c (inch)
E1	-24	32	26.65	27.06	0.2	144			
E2	94	136	27.25	27.76	0.2	144			
R	49	61							
M1	140	153	27.78	27.85	0.5		1.2	8.8	
M2	200	206	28.38	28.50	0.5		1.2	8.8	
M3	226	230	28.99	29.17	0.5		1.2	8.8	
M4	236	240	29.28	29.50	0.5		1.2	8.8	
M5	256	262	30.14	30.47	0.5		1.2	8.8	
M6	266	272	30.74	31.20	0.5		1.2	8.8	
M7	276	282	31.57	32.24	0.5		1.2	8.8	
M8	286	292	32.80	33.84	0.5		1.2	8.8	
C1	320	334							27.80
C2	46	58							29.20

which shows the beam axial envelope vs. energy, the energy spectrum, and r, p_r, and z, p_z at the entrance of the deflector. These calculations start at $E = 240$ MeV, and the initial beam is represented by a combination of rectangular phase space grids associated with a 30 mil radial and 20 mil vertical betatron eigenellipses. The resulting channel entry efficiency is 81.9%. The large energy spread (lower-left in Figure 8.3), which causes low channel transmission rate, comes from two factors. The first is that the initial beam size is much larger than the turn spacing at the head of the septum. The second corresponds to the long thin tail structure, as shown in Figure 8.2, which in turn increases the radial width of the beam, induced by the $\nu_r = 1$ traversal.

As in preceeding chapters, the particles which successfully enter the mouth of the extraction system provide the input data for the extraction optics computations. Figure 8.4 then gives the beam half width and loss histogram in 2^o steps along the extraction channel, the distribution of final energies and the r, p_r, and z, p_z spectrums as the beam exits the cyclotron. The energy spread of the output beam is found to be

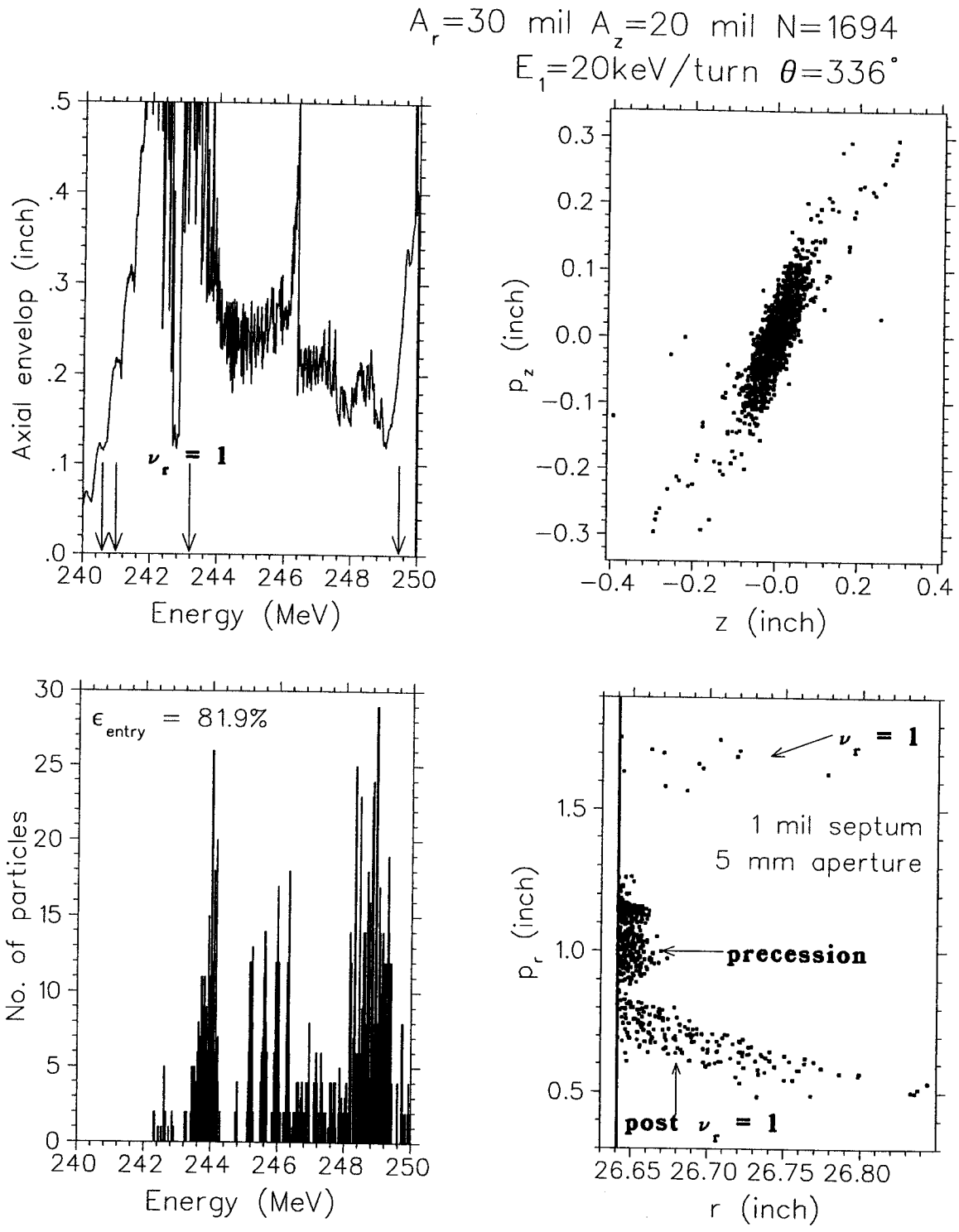

Figure 8.3: Upper left: beam axial envelop vs. energy showing the beam lost vertically due to the resonance transversal and off-centre of beam. The rest: distribution of energies, radial and vertical phase spectrums at the entrance of the extraction channel for those particles successfully enter the deflector.

strongly correlated to the aperture of the electrostatic deflector and to the initial radial spread at the entrance. The resulting channel transmission efficiency and extraction efficiency are 28.1% and 23.0%, respectively.

In conclusion, it is possible but very difficult to get beam out of synchrocyclotrons based on the precession extraction scheme. To accomplish this, we must reduce the septum thickness as much as possible to increase the channel entry rate. Moreover, the location of the electrostatic deflector has to be positioned extremely accurately to match the particle trajectories because of the extremely limited space to insert the septum between the last internal turn and the extracted orbit.

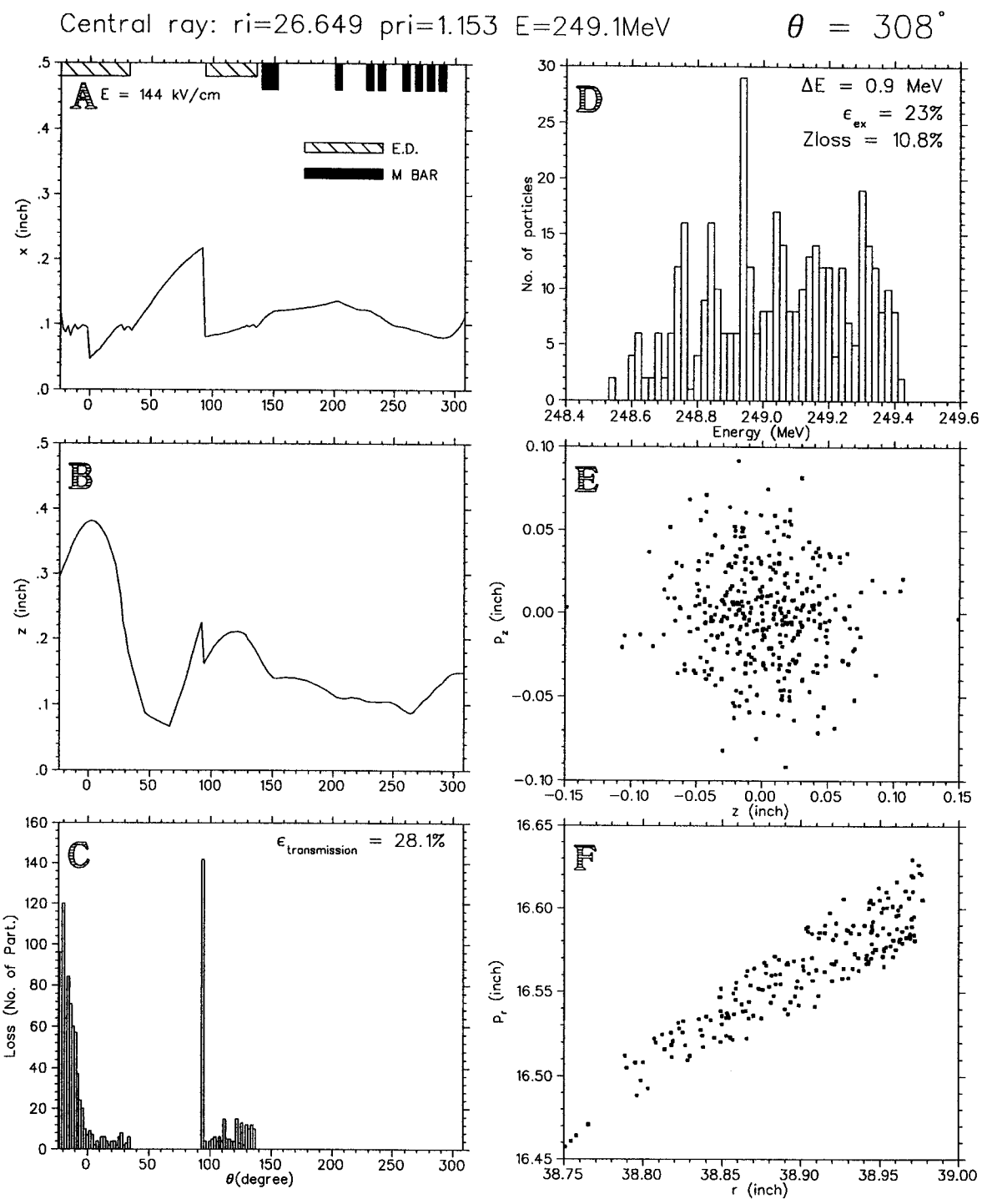

Figure 8.4: Panels A, B, C: the beam half width and loss histogram in 2^o steps vs. θ along the extraction channel. Panel D: distribution of final energies. Panels E, F: radial and vertical phase spectrums at $\theta = 308°$.

Chapter 9

Summary and Conclusions

We noted in Chapter 3 that the orbit problems in the intermediate radius are minor in the proposed K500 adapted synchrocyclotron and the extraction system is then the most critical aspect of the possible conversion and therefore the focus of this thesis, as explained in Chapter 1. Three possible extraction solutions have then been explored: (1) The traditional regenerative method of synchrocyclotron extraction which uses two magnetic disturbances, a regenerator (a positive gradient bump) and a peeler (falling fringe field), to produce a $\cos 2\theta$ field perturbation, and induces radial oscillations with exponential increasing amplitude. (2) The $\nu_r = 1$ excitation extraction system which employs a first harmonic bump to make the orbits drift to a selected radially unstable asymptote as the $\nu_r = 1$ stop band approaches. (3) Precessional extraction, in which a smaller first harmonic bump, is used to produce a small coherent precession of optimum amplitude as the beam accelerates through the $\nu_r = 1$ resonance and, as a result of this precession, post-resonance acceleration gives the radial separation needed to clear the septum.

For all three proposed extraction systems, the existing extraction components of the K500 cyclotron are assumed to be used for economic reasons: Two existing electrostatic deflectors are selected as the first two extraction channels because of their thin septum and well confined field. Following the electrostatic deflectors, eight

passive magnetic elements (focusing bars) are employed to provide assistance to both deflect and focus the beam, due to their negative field in their aperture centre and their strong radially focusing field gradient across the aperture.

The resonances encountered in the extraction and their characteristics are summarized in Table 9.1. One conclusion from the extraction calculations is that the extraction performance in the K250 synchrocyclotron is mainly limited by the resonance transitions. Chapter 4 showed that the amplitude gain for slow resonance traversal is roughly proportional to the square of the driving force and inversely proportional to the energy gain per turn because the width and strength of the stop band are approximately proportional to the driving term, respectively, and the energy gain per turn measures how fast the resonance is traversed. In addition, the resonance crossing will introduce beam distortions which depend strongly on initial beam amplitude, on magnetic field derivatives, and on field imperfections. Consequently, for synchroncyclotrons with their intrinsically low energy gain per turn, the extracted beam's character owing to the resonance traversal will be very sensitive to both the magnetic field imperfections and to the initial beam quality.

The Z^4 and DEFLZ800 codes (see Chapter 2) were used to perform the orbit tracking and extraction efficiency calculations for different conditions. Standard assumptions were:

- A monoenergetic beam starts at E = 240 MeV.
- Initially uniform rectangular phase space grids inside the projected "beam eigenellipses".
- Constant energy gain is assumed in the Z^4 calculations.

The justification for these assumptions (a good approximation and a fast calcula-

Table 9.1: Summary of resonances encountered in the extraction.

Resonance energy and corresponding stop band width							
resonance in ext. region	$\nu_r = 1$ excitation ex. ($B_1 = 1.2$ g)		regenerative extraction		precession extraction		driving force b
	E (MeV)	ΔE (MeV)	E (MeV)	ΔE (MeV)	E (MeV)	ΔE (MeV)	
$\nu_z = 1/2$	240.81	0.14	240.77	0.14	240.58	0.26	dB_1/dr
$\nu_r = 2\nu_z$	241.13		241.19		241.0		field deri. & ampli.
$\nu_r = 1$	243.25	1.14	243.11	0.22	243.19	0.62	B_1
$\nu_r = 2/2$			246.8				$\cos 2\theta$ gradient bump
$\nu_z = 1$	249.86	0.14			249.46	0.46	B_1
$\nu_r + 2\nu_z = 3$	251.13				250.68		field deri. & ampli.
Characteristics	$\Delta A \propto f\left(\frac{b^2}{E_1}\right)$ & amplitude dependence & distortions						
$\nu_z = 1/2$	causes growth of the axial amplitude						
$\nu_r = 2\nu_z$	both radial and vertical amplitude growth depend on initial beam quality, on how fast the stop band is passed, and on the field shape						
$\nu_r = 1$	(1)off-centre drift of beam (2)introduces beam distortions						
$\nu_r = 2/2$	(1)achieved by a positive gradient bump (regenerator) and a neg. grad. bump (falling fringe field, peeler) (2)characterized by exponential growth of radial gain						
$\nu_z = 1$	produces vertical loss						
$\nu_r + 2\nu_z = 3$	final energy limit						

tion) was presented in Chapter 5.

In order to see the influence of several crucial parameters (initial beam quality, energy gain per turn, septum thickness and aperture of electrostatic deflectors) on extraction efficiency and for comparison among these three mechanisms, calculations have been done with one parameter changed in turn while keeping the others fixed. The results are summarized in Table 9.2. The parameters $A_i(i = r, z)$ are betatron oscillation amplitudes, B_1 the net first harmonic bump amplitude, E_1 the energy gain per turn, t the septum thickness, A the aperture of the electrostatic deflectors, Δr the turn spacing at the septum entrance for initially centered particles, ϵ_{entry} the channel entry efficiency, ϵ_{ext} the total extraction efficiency, and zloss the total vertical loss in %.

The results in Table 9.2 are well explained by the following arguments and comments: (1) In general, the field imperfections produced by extraction devices could not be completely canceled by a first harmonic bump with two adjustable parameters (strength and azimuth) probably due to the scalloping of the orbits; canceling the field imperfections over a limited range at resonance radius is not enough to maintain the orbits in an undisturbed stable state. (2) It seems that the radial position of M1 (and its 180^o compensator C1), owing to its proximity to the internal beam and its large azimuthal width, has significant influence on how successfully the field imperfections in the vicinity of $\nu_r = 1$ can be compensated. (3) As the septum thickness is reduced, the channel entry efficiency rises, and the extraction efficiency typically also increases. (4) The larger the aperture of the electrostatic deflectors, the larger the acceptance of the extraction system, and the bigger the external current. (5) We expect that poor initial beam quality will give rise to low extraction efficiency due to the resonance traversal. (6) Increasing the dee voltage (usually implying larger energy gain per turn) will raise the current extracted from the ion source, enhance

the space charge limit, and decrease the amplitude growth due to resonance crossing or increase the acceptance of the resonance; therefore in general, we will end up with higher extraction efficiency and larger output current by increasing the dee voltage.

In Chapter 6, a weak regenerator (50 gauss/cm) system, giving turn to turn spacing at the septum entrance of about 0.1″, was described. With 0.1″ separation, the axial instability induced by the off-center beam was substantially allayed as was seen in Figure 6.13, and a high channel entry efficiency owing to the very thin 0.01″ electrostatic septum was achieved. In addition, it is rather easy to compensate the fringe field of the weak regenerator to reduce the beam loss when the beam passes through the resonances compared to the situation in a traditional synchrocyclotron where a magnetic element is normally used as the first extraction channel. Satisfactory results are therefore expected using the regenerative extraction scheme.

There are two primary difficulties in the $\nu_r = 1$ excitation extraction (Chapter 7), summarized as follows. The electric field strength, which puts a limit on the maximum aperture of electrostatic deflectors, is one of the limiting factors to achieve high extraction efficiency in the $\nu_r = 1$ resonant extraction scheme. Another factor is that the three resonances ($\nu_z = 1/2, \nu_r = 2\nu_z, \nu_r = 1$) are only about 3 mm apart – so close that it is not possible to excite the $\nu_r = 1$ resonance alone without also exciting the resonances $\nu_z = 1/2$ and $\nu_r = 2\nu_z$. For example, the $\nu_r = 1$ excitation extraction performance can not be improved by increasing dee voltage because: The field bump becomes significantly less effective as energy gain per turn increases. The larger energy gain per turn will thus call for a stronger bump to restore the extraction effectiveness. However, this also increases the vertical driving force for resonance crossing ($\nu_z = 1/2, \nu_r = 2\nu_z$) and thus induces vertical instability.

Chapter 8 concluded that for high magnetic field synchroncyclotrons with their intrinsically low energy gain, i.e., small turn to turn separation, the precession ex-

Table 9.2: Summary of extraction calculations. The betatron oscillation amplitudes are denoted as $A_i(i = r, z)$, the net first harmonic bump amplitude B_1, the energy gain per turn E_1, the septum thickness t, the aperture of the electrostatic deflectors A, the turn spacing at the septum entrance for initially centered particles Δr, the channel entry efficiency ϵ_{entry}, the total extraction efficiency ϵ_{ext}, and the total vertical loss zloss.

Regenerative extraction $E_f \sim 247$ MeV $E \sim 96$ kV/cm									
initial conditions									
A_r (mil)	A_z (mil)	total orbits	E_1 (keV/turn)	t (mil)	A (mm)	Δr (mil)	ϵ_{entry} (%)	ϵ_{ext} (%)	zloss (%)
30	20	1748	10	10	10	105	92.30	41.77	0.00
30	20	1748	20	10	10	101	90.78	52.00	0.00
30	20	1748	10	1	10	105	99.65	42.06	0.00
30	20	1748	10	10	5	105	90.72	21.15	0.00
50	40	3255	10	10	10	105	75.42	22.09	18.04
50	40	3255	20	10	10	101	91.64	37.36	1.14
$\nu_r = 1$ **excitation extraction** $E_f \sim 243$ MeV $E \sim 159$ kV/cm										
initial conditions										
A_r (mil)	A_z (mil)	total orbits	B_1 (g)	E_1 (keV /turn)	t (mil)	A (mm)	Δr (mil)	ϵ_{entry} (%)	ϵ_{ext} (%)	zloss (%)
30	20	1725	1.2	10	10	5	60	83.30	17.80	6.03
30	20	1725	1.7	20	10	5	58	81.68	19.36	5.45
30	20	1725	1.2	10	1	5	60	92.00	19.54	6.38
30	20	1725	1.2	10	10	10	60	88.88	32.70	8.81
50	40	3404	1.2	10	10	5	60	39.75	7.76	58.84
50	40	3404	1.7	20	10	5	58	43.95	9.75	51.59
Precession extraction $E_f \sim 249$ MeV $E \sim 144$ kV/cm									
initial conditions									
A_r (mil)	A_z (mil)	total orbits	E_1 (keV/turn)	t (mil)	A (mm)	Δr (mil)	ϵ_{entry} (%)	ϵ_{ext} (%)	zloss (%)
30	20	1694	20	1	5	10	81.88	23.02	10.80
30	20	1694	10	1	5	5	41.44	6.26	51.12
30	20	1694	20	10	5	10	34.83	4.25	10.33
30	20	1694	20	1	10	10	82.23	31.70	10.80
50	40	3441	20	1	5	10	50.77	11.48	41.96

traction is not an attractive way to extract the beam.

In conclusion, three important results have been established by this study. (1) The magnetic fields in the extraction region has to be manipulated carefully to avoid the beam loss induced by the resonance transitions due to the beam's low energy gain. (2) The regenerative extraction system is a promising candidate for the proposed conversion of the K500 to a 250 MeV synchrocyclotron for proton therapy because it is reasonably easy to construct and gives better results than the other two methods. (3) This K500 adapted synchrocyclotron will have an output proton energy of about 250 MeV and should have an external beam current in the range of 5 to 30 nA which meets the requirements for its purpose. Important parameters of the proposed machine are given in Table 9.3.

Table 9.3: Parameters of the K250 proton synchrocyclotron

		unit	Comment
Beam			
type of ions	H^+		
output energy	~ 250	MeV	
internal current	30	nA	$V_{dee} = 15kV$
internal current	60	nA	$V_{dee} = 30kV$
external current	5 - 30	nA	
Magnetic structure			
number of sectors	3		
spiral angle constant	4.407	deg/inch	
average field at extraction	3.591	tesla	
average field at center	3.314	tesla	
hill gap	2.5	inch	
valley gap	~ 22	inch	
RF system			
dee voltage	15 (30)	kV	
resonating system	2 dees coupled		
harmonic number	h=1		
synchronous phase angle ϕ_s	48.2	degree	$E_1 = q \cdot V_{dee} \cdot cos\phi$
acceleration time	0.53	ms	$V_{dee} = 15kV$
acceleration time	0.26	ms	$V_{dee} = 30kV$
modulation frequency	1.0	kHz	
Central region			
type of source	P.I.G.		
slit size	0.33×0.95	mm^2	
phase acceptance	20	degree	assumption
capture efficiency	0.2	%	assumption

Bibliography

[1] E.O. Lawrence and N.E. Edlefsen, On the production of high speed protons, Science 72, 376, (1930).

[2] E.O. Lawrence and M.S. Livingston, The production of high speed protons without the use of high voltages, Phys. Rev. 40, 19, (1932).

[3] J.R. Richardson, A short anecdotal history of the cyclotron, 10th Int. Conf. on Cyclotrons and their applications, 617, (1984).

[4] V.I. Veksler, A new method of acceleration of relativistic particles, J. of Physics USSR 9, 153, (1945).

[5] E.M. Mcmillan, The synchrotron - a proposed high energy particle accelerator, Phys. Rev. 68, 143, (1945); The origin of the synchrotron, 69, 534, (1946).

[6] H.G. Blosser, Synchrocyclotron improvement programs, Proc. 5th Int. Cyclotron Conf., 405, (1969).

[7] L.H. Thomas, The paths of ions in the cyclotron, Phy. Rev. 54, 580, (1938).

[8] E.L. Kelly, et al., Two electron models of a constant frequency relativistic cyclotron, Rev. Sci. Instr. 27, 493, (1956).

[9] K.R. Symon, et al., Fixed-field alternating-gradient particle accelerators, Phys. Rev. 103, 1837, (1956).

[10] H.G. Blosser and A. I. Galonsky, The MSU 53 MeV cyclotron, IEEE Trans. on Nucl. Sci., NS-13, 4, 466, (1966).

[11] J.R. Richardson, The status of TRIUMF, 7th Int. Conf. on Cyclotrons and their applications, 41, (1975).

[12] H.A. Willax, Status report on SIN, 7th Int. Conf. on Cyclotrons and their applications, 33, (1975).

[13] R.E. Pollock, Status report on the Indiana University cyclotron facility, 7th Int. Conf. on Cyclotrons and their applications, 27, (1975).

[14] P. Miller, The MSU superconducting cyclotron program, 10th Int. Conf. on Cyclotrons and their applications, 11, (1984).

[15] J.A. Nolen, et al., Commissioning experience with the NSCL K1200 superconducting cyclotron, 12th Int. Conf. on Cyclotrons and their applications, 5, (1989).

[16] H. Schmeing, et al., Current status of the superconducting cyclotron at Chalk River, 12th Int. Conf. on Cyclotrons and their applications, 88, (1989).

[17] H.G. Blosser, Application of superconductivity in cyclotron construction, 9th Int. Conf. on Cyclotrons and their applications, 147, (1981).

[18] R.R. Wilson, Radiological use of fast protons, Radiology 47, 487, (1946).

[19] C.A. Tobias, et al., Radiological use of high energy deuterons and alpha particles, Rad. Ther. Nucl. Med. 67, 1, (1952).

[20] Max L. M. Boone, et al., Introduction to the use of protons and heavy ions in radiation therapy: historical perspective, Int. J. Radiation Oncology Biol. Phys. 3, 65, (1977).

[21] H.G. Blosser, et al., Proposal for a manufacturing prototype superconducting cyclotron for advanced cancer therapy, MSUCL-874, (1993).

[22] Gary Stix, Beam of hope, Scientific American 263, 24, (1990).

[23] XiaoYu Wu, Conceptual design and orbit dynamics in a 250 MeV superconducting synchrocyclotron, Ph. D. Thesis, Michigan St. Univ., (1990).

[24] D. Böhne, Synchrotrons for cancer therapy, EPAC, 217, (1992).

[25] Y. Jongen, et al., Progress report on the IBA-SHI proton therapy system, 13th Int. Conf. on Cyclotrons and their applications, 244, (1992).

[26] A.F. Thornton and H.D. Suit, Current and Potential Clinical Indications of Proton Irradiation, 13th Int. Conf. on Cyclotrons and their applications, 234, (1992).

[27] M.J. Berger, Penetration of proton beams through water I. Depth-dose distribution, spectra and LET distribution, NISTIR 5226, (1993).

[28] A.M. Koehler, et al., Protons in radiation therapy (comparative dose distributions for protons, photons, and electrons), Radiology 104, 191, (1974).

[29] E. Pedroni, Accelerators for charged particle therapy: performance criteria from the user point of view, 13th Int. Conf. on Cyclotrons and their applications, 226, (1992).

[30] R.L. Maughan, H.G. Blosser (the builder of the Harper medical cyclotron) and W.E. Powers, A superconducting cyclotron for neutron radiation therapy, Medical physics 21, 779, (1994).

[31] P. Mandrillon, et al., Status of the feasibility studies of the European light ion medical accelerator, 12th Int. Conf. on Cyclotrons and their applications, 152, (1989).

[32] S Holm and P-U Renberg, Magnetic field design for a combined fixed frequency and frequency modulated cyclotron, IEEE Trans. on Nucl. Sci., NS-26, 2012, (1979).

[33] H.G. Blosser and D.A. Johnson, Focusing properties of superconducting cyclotron magnets, Nucl. Inst. Meth. 121, 301, (1974).

[34] E. Fabrici and F.G. Resmini, A survey of beam dynamics prior to extraction in the K-500 cyclotron at M.S.U., Nucl. Inst. Meth. 180, 319, (1981).

[35] G. Bellomo and F.G. Resmini, Trimming of the magnetic field for the K-500 cyclotron at M.S.U., Nucl. Inst. Meth. 180, 305, (1981)

[36] H.G. Blosser and M.M. Gordon, Performance estimates for injector cyclotrons, Nucl. Inst. Meth. 13, 101, (1961).

[37] H.G. Blosser, Optimization of the cyclotron central region for the nuclear physics user, 123, NSCL annual report 1969-70.

[38] S. Holm, Factors affecting beam intensity and quality in synchrocyclotrons, Proc. 5th Int. Cyclotron Conf., 736, (1969).

[39] Steve Snyder, NSCL internal report, unpublished.

[40] E. Fabrici, et al., The extraction system for the K500 cyclotron at MSU, Nucl. Inst. Meth. 184, 301, (1981).

[41] Hogil Kim, Regenerative beam extraction, IEEE Trans. on Nucl. Sci., NS-13, 4, 58, (1966).

[42] H.G. Blosser, et al., Resonant extraction from three-sector low-spiral cyclotrons, Nucl. Inst. Meth. 18/19, 488, (1962).

[43] M.M. Gordon, Single turn extraction, IEEE Trans. on Nucl. Sci., NS-13, 4, 48, (1966).

[44] D.W. Kerst and R. Serber, Electronic orbits in the induction accelerator, Phys. Rev. 60, 53, (1941).

[45] M.M. Gordon, The Oak Ridge relativistic isochronous cyclotron, Nucl. Inst. Meth. 6, 221, (1960).

[46] H.G. Blosser, Class note, Phy 961, MSU, (1971).

[47] M.M. Gordon, Computation of closed orbits and basic focusing properties for sector-focused cyclotrons and the design of CYCLOPS, Particle accelerators 16, 39, (1984).

[48] D.J. Clark, et al., The criteria and techniques of magnetic field measurement used on the UCLA 50 MeV spiral ridge cyclotron, Nucl. Inst. Meth. 14, 321, (1961).

[49] M.M. Gordon and D.A. Johnson, Calculation of fields in a superconducting cyclotron assuming uniform magnetization of the pole tips, Particle Accelerators 10, 217, (1980).

[50] M.M. Gordon and E.M. Fabrici, Beam extraction system for the K=500 superconducting cyclotron, IEEE Trans. Nucl. Sci., NS-26, 2101, (1979).

[51] M.M. Gordon and V. Taivassalo, The Z^4 orbit code and the focusing bar fields used in the beam extraction calculations for superconducting cyclotrons, Nucl. Inst. Meth. A247, 423, (1986).

[52] D.A. Johnson, NSCL internal report, unpublished.

[53] Felix Marti and Dong-O Jeon, NSCL, private communication.

[54] P. Miller, et al., The magnetic field of the K500 cyclotron, MSUCP-37, (1982).

[55] M. Reiser, et al., Conversion studies for the SREL 600-MeV synchrocyclotron, Proc. 5th Int. Cyclotron Conf., 749, (1969).

[56] Dong-O Jeon, Finite difference method for calculating magnetic field components off median plane using median field data, submitted to Journal of Computational Physics.

[57] R. Baartman, et al., Amplitude growth from the rapid traversal of a half-integer resonance, Proc. 10th Int. Conf. on Cyclotrons and their Applications, IEEE, NS-40, (1984).

[58] M.M. Gordon and Dong-O Jeon, Improved formulas for calculating cyclotron orbit properties, Nucl. Inst. Meth. A301, 182, (1991).

[59] R. Baartman, et. al., Beam optics for a 12-GeV isochronous cyclotron ring, IEEE Trans. Nucl. Sci., NS-30, 2010, (1983).

[60] M.M. Gordon, Orbit properties of the isochronous ring cyclotron with radial sectors, Annals of Physics 50, 571, (1968).

[61] S. Suwa, et al., Efficient Beam extraction from a synchro-cyclotron at n=1, Nucl. Inst. Meth. 5, 189, (1959).

[62] A.A. Garren, et al., Electrostatic deflector calculations for the Berkeley 88″ cyclotron, Nucl. Inst. Math. 18/19, 525, (1962).

[63] J.J. Livingood, Principles of cyclic particle acceleration, Van Nostrand, New York, Chap. 6, (1961).

[64] D. Bohm and L.L. Foldy, Theory of the synchro-cyclotron, Physical review 72, 649, (1947).

[65] M.L. Mallory, Phase space density studies on cyclotron ion sources, Ph. D. Thesis, Michigan St. Univ., (1966).

[66] K.J. Lecouteur, The regenerative deflector for synchrocyclotrons, Proc. Phys. Soc., London B64, 1073, (1951).

[67] K.J. Lecouteur, Perturbations in the magnetic deflector for synchrocyclotrons, Proc. Phys. Soc. B66, 25, (1953).

[68] K.J. Lecouteur, Non-linear regenerative extraction of synchrocyclotron beams, Phil. Mag. 46, 1265, (1955).

[69] S. Lindbäck, A study of the regenerative extraction system in the CERN synchrocyclotron, Proc. 5th Int. Cyclotron Conf., 235, (1969).

[70] F.T. Howard, Cyclotron-1972, AVF and FM, Proc. 6th Int. Conf. on Cyclotrons and their Applications, 689, (1972).

[71] L.O. Andersson, The Gustaf Werner Cyclotron, 9, TSL progress report, 1992-93.

[72] B. Allardyce, et. al., The extraction system of the improved CERN synchrocyclotron, Proc. 7th Int. Conf. on Cyclotrons and their Applications, 287, (1975).

[73] W.F. Stubbins, Design of regenerative extractors for synchrocyclotrons, Rev. Sci. Instr. 29, 722, (1958).

[74] S. Holm, Status report on the Gustaf Werner cyclotron in Uppsala, Proc. 13th Int. Cyclotron Conf., 106, (1992).

[75] Thomas Kuo and Jerry Nolen, Deflector Development for the K1200 cyclotron, 13th Int. Conf. on Cyclotrons and their Applications, 596, (1992).

[76] Chalk River Nuclear Laboratories, TASCC Newsletter 8#1, (Jan, 1994).

[77] M. Conte and W.W. Mackay, An introduction to the physics of particle accelerators, Chap. 10, (1991).

[78] L.J. Laslett and S.J. Wolfson, Concerning the $\nu/N \rightarrow 1/3$ resonance, 5. Analysis of the equation $\frac{d^2v}{ds^2} + (\frac{2\nu}{N})^2 v - \frac{b}{2}(cos2s)v^2 - \lambda(cos\frac{2s}{3}) = 0$, MURA-497.